NOTICE

THIS DOCUMENT HAS BEEN REPRODUCED FROM MICROFICHE. ALTHOUGH IT IS RECOGNIZED THAT CERTAIN PORTIONS ARE ILLEGIBLE, IT IS BEING RELEASED IN THE INTEREST OF MAKING AVAILABLE AS MUCH INFORMATION AS POSSIBLE

UNIVERSITY OF ILLINOIS
URBANA

AERONOMY REPORT NO. 91

A ROCKET-BORNE ENERGY SPECTROMETER USING MULTIPLE SOLID-STATE DETECTORS FOR PARTICLE IDENTIFICATION

by
K. L. Fries
L. G. Smith
H. D. Voss

December 1, 1979

A E R O N O M Y   R E P O R T

N O.   91

A ROCKET-BORNE ENERGY SPECTROMETER USING MULTIPLE

SOLID-STATE DETECTORS FOR PARTICLE IDENTIFICATION

by

K. L. Fries
L. G. Smith
H. D. Voss

December 1, 1979

Aeronomy Laboratory
Department of Electrical Engineering
University of Illinois
Urbana, Illinois

ABSTRACT

A rocket-borne experiment using energy spectrometers that allows particle identification by the use of multiple solid-state detectors is described. The instrumentation provides information regarding the energy spectrum, pitch-angle distribution, and the type of energetic particles present in the ionosphere.

Particle identification is accomplished by considering the different loss mechanisms, and the effects on various types of particles, for solid-state detectors with gold and aluminum surfaces of several thicknesses. The ratios of measured energies for the various detectors are compared against known relationships during ground-based analysis in order to obtain particle identification.

Pitch-angle information is obtained by using detectors with small geometrical factors mounted with several look angles. Particle flux is recorded as a function of rocket azimuth angle. By considering the rocket azimuth, the rocket precession, and the location of the detectors on the rocket, the pitch angle of the incident particles is derived.

The detectors, charge preamplifiers, and pulse shaping (filtering) electronics are described in detail. Specifically, the detector loss mechanisms used in particle identification, the requirements of the low-noise preamplifier and the conflicting requirements of optimal noise filtering and signal pulse shaping for the pulse-shaping electronics are discussed.

TABLE OF CONTENTS

LIST OF FIGURES

1. INTRODUCTION

This report describes the development and first results of a rocket-borne experiment to identify and obtain the flux and energy spectrum of energetic particles in the upper atmosphere. A group of energetic particle spectrometers (EPS's) is used; each has a solid-state detector. The identification of the type of particle is based on the comparison of flux measured with detectors having surface metal layers of different thicknesses of aluminum and gold. The pitch-angle distribution is obtained by mounting the detectors with different orientations and by processing this data with respect to the azimuth of the spinning rocket. The system was built for use on payloads launched in the Joint American-Soviet Particle Intercalibration (JASPIC) Program.

The JASPIC Program involved four American rockets (three Nike Apaches and one Nike Tomahawk) and five Soviet MR12 rockets. Experiments provided by several groups including the University of Illinois, Cornell University, the University of Texas, Aerospace Corporation, and the Soviets were used in near-simultaneous launches to provide data that will help in the interpretation of the large variability in particle measurements made, in the past, at different times and different places.

The instruments flown by the University of Illinois on the JASPIC Program on Nike Apache 14.543 in June 1978 and on Nike Apache 14.542 in September 1978 were designed to provide detailed energy spectrum and pitch-angle information. These data are to be compared with the model of the nighttime ionosphere presented in *Voss and Smith* [1977] and with other measurements.

A general description of the array of energetic particle spectrometers is given in Chapter 2. The subsequent sections of this report concern the details of design and construction of the instrument.

Chapter 3 describes the solid-state detectors used in the instrument. The theory of operation and the physical and electrical properties are discussed. The method used for particle identification is described.

The problem of noise and the signal processing to minimize the effects of noise are discussed in Chapter 4. A theoretical approach is used, producing general results. The actual electronics and the reasons for the specific design are discussed in Chapter 5.

The calibration of the instrument is outlined in Chapter 6. Some preliminary flight data are presented in Chapter 7.

A summary of the work performed and suggestions for future work are contained in Chapter 8.

2. GENERAL DESCRIPTION OF THE SYSTEM

2.1 *Energetic Particle Spectrometers*

An Energetic Particle Spectrometer (EPS) is required to provide information regarding the energy of a particle that enters the detector. This information can be obtained in analog or digital form. With the addition of counting electronics one obtains information regarding the particle flux in terms of the number of occurrences of a particle (counts) that fall within a given energy range (channel). The greater the number of channels, the better the energy resolution. There must, however, be a statistically significant counting rate in, at least, some of the channels.

The type of output used depends upon the application of the EPS. For the rocket-borne application we are interested in measuring relatively low energy particles (10 keV to 100 keV) which produce ionization in the E region of the ionosphere. In this application we are primarily interested in energetic electrons and ions such as hydrogen, helium, or oxygen. In addition to particle energy, particle identification and pitch angle the angle between the velocity vector of the particle and the local magnetic field) are of interest.

In the present application the number of particles that fall within a given range of energy is more important than the actual energy of an individual particle. For this realization the configuration shown in Figure 2.1 is used. The detector is followed by a preamplifier and a pulse shaper. The pulse shaper refers to the filter that modifies the signal pulse and reduces the noise inherent in the system. The output of the shaper is a pulse whose amplitude is proportional to the energy of the incident particle. The detector, preamplifier, and pulse shaper will be referred to as the linear section of the system. The term linear is used because linear systems analysis techniques are applicable. For the evaluation of different detectors or different electronics the signal is observed at this point.

The remainder of the EPS is the counting electronics. This will be referred to as the non-linear section because the techniques used to analyze linear systems cannot be used on this portion of the EPS. This portion of the circuit includes a pulse-height analyzer. The level of the analog pulse is checked and the counter that corresponds to the band of energies that includes the measured energy is incremented.
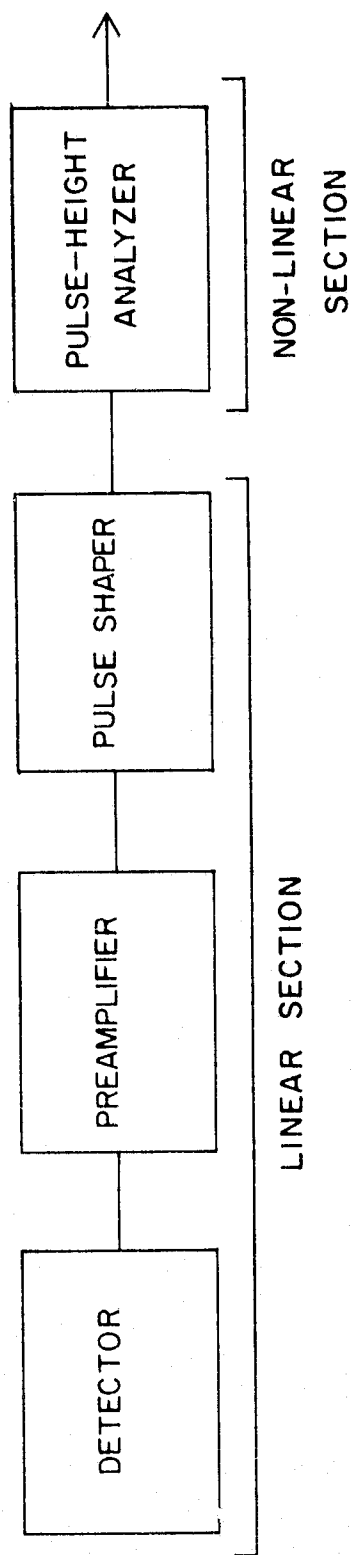
Figure 2.1 The principal elements of an energetic particle spectrometer.

2.2 *The Detector*

The detector's function is to produce an electrical signal that is related to the energy of an incident energetic particle. The surface-barrier solid-state detector produces a charge that is proportional to the incident particle energy. In addition, the detector is rugged, easily mounted, small, requires relatively low bias voltages, and has good resolution. For the above reasons this type of detector has been chosen for rocket-borne EPS applications [*Voss and Smith*, 1974].

The operation of the solid-state detector is analogous to the operation of an ionization chamber. An energetic particle will ionize the gas in an ionization chamber; the number of ions will be proportional to the energy of the particle. An electric field will collect the charge (ions) and this charge pulse can be amplified and filtered.

When an energetic particle enters a solid-state detector, it produces free carriers. The number of carriers is proportional to the energy of the particle. The electric field, caused by the reverse bias applied to the surface barrier detector, will rapidly collect the free charges generated in the depletion layer. This results in a charge pulse of short duration (typically 1 ns).

The surface of the solid-state detector is coated with metal (aluminum or gold) to reduce the sensitivity to light and to provide electrical contact. Particles that enter the detector must pass through the metal layer; interaction results in the loss of some of the particle's energy. Since this energy loss occurs outside the depletion region of the detector, the charge that is collected may be less than would be produced in the absence of the layer. (Only carriers that are produced in the depletion region of the detector are collected.) Because the atomic interactions depend upon the mass of the incident particle and the type and thickness of the metal, the same type of particles incur different losses in different detectors. By comparing the ratios of measured energies for the same type of particles from detectors with different surface metal layers, the incident particle type can be identified.

2.3 *The Preamplifier*

The preamplifier is a high-gain low-noise amplifier. High gain is required so that the noise injected to the system is confined to the detector and the first stage. Once the signal has been amplified to a

reasonable level, the noise introduced in later stages will be too small to affect the system performance. Similarly, low noise is required to minimize the noise that does affect the system performance.

In addition to gain and noise, the input impedance and the stability (variations with temperature, supply voltage, etc.) must be considered. The solid-state detector produces a current pulse whose duration is independent of the energy of the incident particle. It will be shown in Chapter 3 that the detector is primarily capacitive, and that the value of the capacitance will vary with the temperature of the detector and the applied bias. The current pulse corresponds to a charge which is proportional to the energy of the incident particle and produces a voltage across the input capacitance of the preamplifier/detector combination. Since the detector capacitance is variable, it is desirable that the preamplifier be insensitive to the variations due to the detector. This could be accomplished by adding a large capacitor in parallel with the detector. However, as will be shown in Chapter 5, a charge-amplifier configuration will produce the desired result, without the reduction in signal voltage level that would occur if a large capacitor was placed across the detector. A high input impedance is desired so that the charge from the detector appears across the input capacitance, and is not dissipated in the shunt resistance across the detector.

To satisfy the requirements of high input impedance and low noise, a junction field effect transistor (JFET) is used for the preamplifier. The circuit is discussed in detail in Chapter 5.

2.4 *Signal Processing in the Presence of Noise*

Signal processing, which here involves pulse shaping (filtering), is required for two reasons: (1) the peak of the signal pulse is to be detected by a pulse-height analyzer; and (2) filtering can be performed to improve the signal-to-noise ratio of the system.

Without any pulse shaping the charge preamplifier output will resemble a staircase waveform: each charge pulse will increase the voltage across the effective input capacitance by an amount proportional to the incident particle energy. Since we are interested in the charge produced by an individual pulse, which corresponds to the energy of that particle, rather than the total charge accumulated, this output pulse shape is not very desirable.

By passing the preamplifier output through a high-pass filter we can eliminate the dc component of the signal and observe pulses centered about zero volts. By adding a low-pass filter, making the total filter a band-pass configuration, the length of the output pulse can be chosen so that two pulses occurring at almost the same time will not overlap.

Restrictions must also be placed on the pulse shape because of the limitations of the pulse-height analyzer. To insure proper operation the rise time of the pulse and the sharpness of the peak are limited.

The spectral density of the noise in the system is not flat. By varying the pulse-shaping (filter) characteristics the noise performance of the system can be changed. By using techniques developed for communication systems the best possible noise performance can be determined.

The points listed above along with restrictions due to the electronic circuitry are considered in Chapter 5. The design of the electronics (preamplifier and shaping amplifier) for the instrument flown is also discussed there.

2.5 *Data Collection*

The data collection system of an EPS usually consists of a pulse-height analyzer. The actual configuration will vary depending upon the specific application; variable elements include the method of data collection, how the data is sorted, and the method of storage.

Because of the many possible realizations of the data collection system, a general description will not be presented here. The next section contains a description of the system used in the JASPIC payloads.

2.6 *Instrumentation for Nike Apaches 14.542 and 14.543*

The arrangement of the energetic particle experiments in the payloads for the JASPIC Program are shown graphically in Figure 2.2. The Electrostatic Analyzer (ESA) is another instrument used to measure energetic particles. It is included to measure particle energies in the range of 1 to 10 keV, too small to be measured by a solid-state detector. The ESA uses a programmed (stepped) electric field to select the particle energies to be detected (as compared to the EPS which looks at all particle energies simultaneously). This instrument is described in detail in *Pozzi et al.* [1979].

The EPS consists of six solid-state detectors with their associated preamplifiers, three analog switches, four pulse-shaping amplifiers, four

DOOR RELEASE
MECHANISM

ENERGETIC PARTICLE
SPECTROMETERS
(EPS)

26.687

11.75 DOOR
LENGTH
(2.37 WIDTH)

DOOR

DOOR

ELECTROSTATIC
ANALYZER DECK

ESA PREAMPLIFIER

17.625

COUNTING ELECTRONICS

14.250

MICROPROCESSOR
AND PHA DECK

10.875

QUAD DELAY TIMER
(DOOR RELEASE,
SWEEP INHIBIT,
HI VOLT TURN ON,
APOGEE SWITCH)

9.375

+28V BATTERY
+10V BATTERY

6.312

CONTROL DECK
BAROSWITCHES

4.625

−28V CONVERTER

UMBILICAL CONNECTOR

2.000

MAGNETOMETER

0 REF

Figure 2.2 The part of the payload containing the energetic particle
experiments. The payload also contains probe and propagation
experiments for electron density.

pulse-height analyzers, a multiplexer, A/D converter, and a microprocessor data-manipulation system. A block diagram of the EPS experiment is shown in Figure 2.3. To allow comparison of results and to provide redundancy in case of a failure of the microprocessor two additional systems were included: the analog signal from a multiplexer and the pulse-counting circuits.

The pulse-counting circuits, used in previous flights, are shown in Figure 2.3. This unit contains six threshold detectors (comparators), each followed by a counter. For the present flights only one threshold was assigned to shapers 1 through 3; shaper 4 had three thresholds assigned to it. The microprocessor while using one telemetry channel provides much more information than the six channels required by the counting electronics.

Six detectors were included to provide detailed pitch-angle information and to allow particle identification. Because of limitation in the data-manipulation system and space considerations, only four channels could be handled. Three channels are switched to different detectors at apogee in order to obtain information from the other detectors. Statistics for the detectors are listed in Table 2.1.

The detectors are mounted at specific look angles: 45°, 90° and 135°, referred to the rocket spin axis. The microprocessor tabulates particle counts based on energy level (pulse height) and rocket azimuth. Using information from the spin magnetometer the look angle of each detector relative to the magnetic field can be determined at each instant. This allows the flux to be determined as a function of the pitch angle of the particles.

The different surface materials of the solid-state detectors result in different responses from the various detectors for a given particle type. When the ratios of energy levels measured on the different detectors are compared for a given particle, the particle type can be identified. A magnet is mounted on one detector to prevent electrons from being detected; this provides an additional check for particle identification.

The block diagram of the pulse-height analyzer is shown in Figure 2.4. A sequential programmer (counter) selects the detector channel that is to be measured. This is accomplished by an analog multiplexer; the desired pulse-height detector is routed to the A/D. The other analog multiplexer resets the pulse-height detector after a measurement is taken. Consider
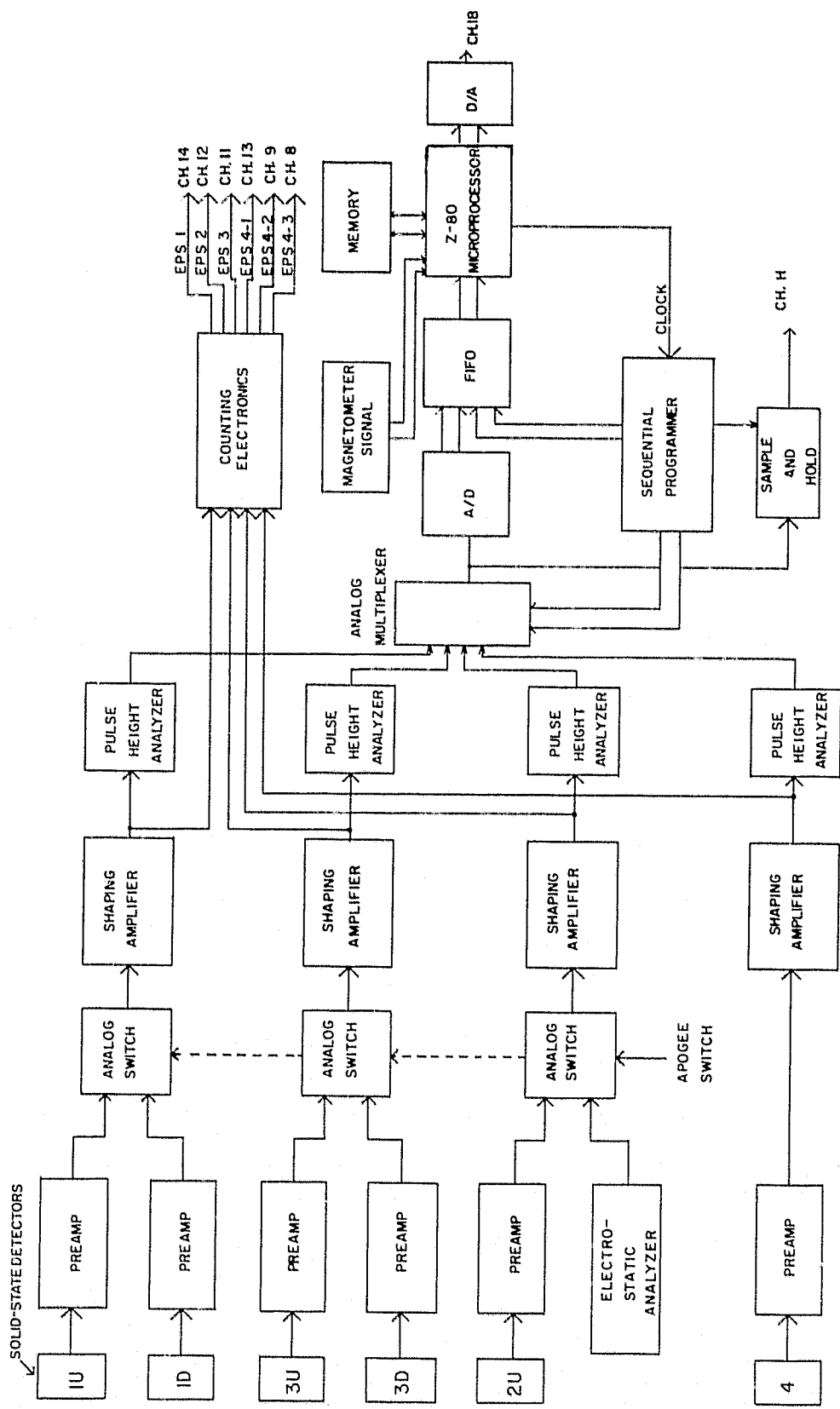
Figure 2.3 Block diagram of energetic particle spectrometer. The data are transmitted on the indicated channels of the telemetry system.

Table 2.1

University of Illinois solid-state detector experiments.

Designation†	Geometrical Factor (cm² ster)	Front Surface Material (μg cm⁻²)**	Look Angle from Spin Axis (deg)	Energy Range (keV**) Electrons	Protons	Energy Channels	Pitch Angle Sectors	Comments
EPS 1 U	0.05	40-Au	90	>10	>15	12	15	High Resolution Detectors Energetic Particle Identification
EPS 1 D	0.05	40-Au	90	>150	>15	12	15	Electron Broom Magnet CWEF*
EPS 2 U	0.05	100-Al	90	>12	>55	11	15	For Energetic Particle Identification, CWEF
EPS 3 U	0.05	40-Al(Au)	45	>10	>25 (15)	12	15	Precipitated Flux
EPS 3 D	0.05	40-Al(Au)	135	>10	>25 (15)	12	15	Backscattered Flux
EPS 4 UD	0.05	40-Al	90	>10	>25	12	15	CWEF and Ion Mass Determination

* Comparison with earlier flights
** Parentheses for Nike Apache 14.543 only
† U indicates ascent and D indicates descent
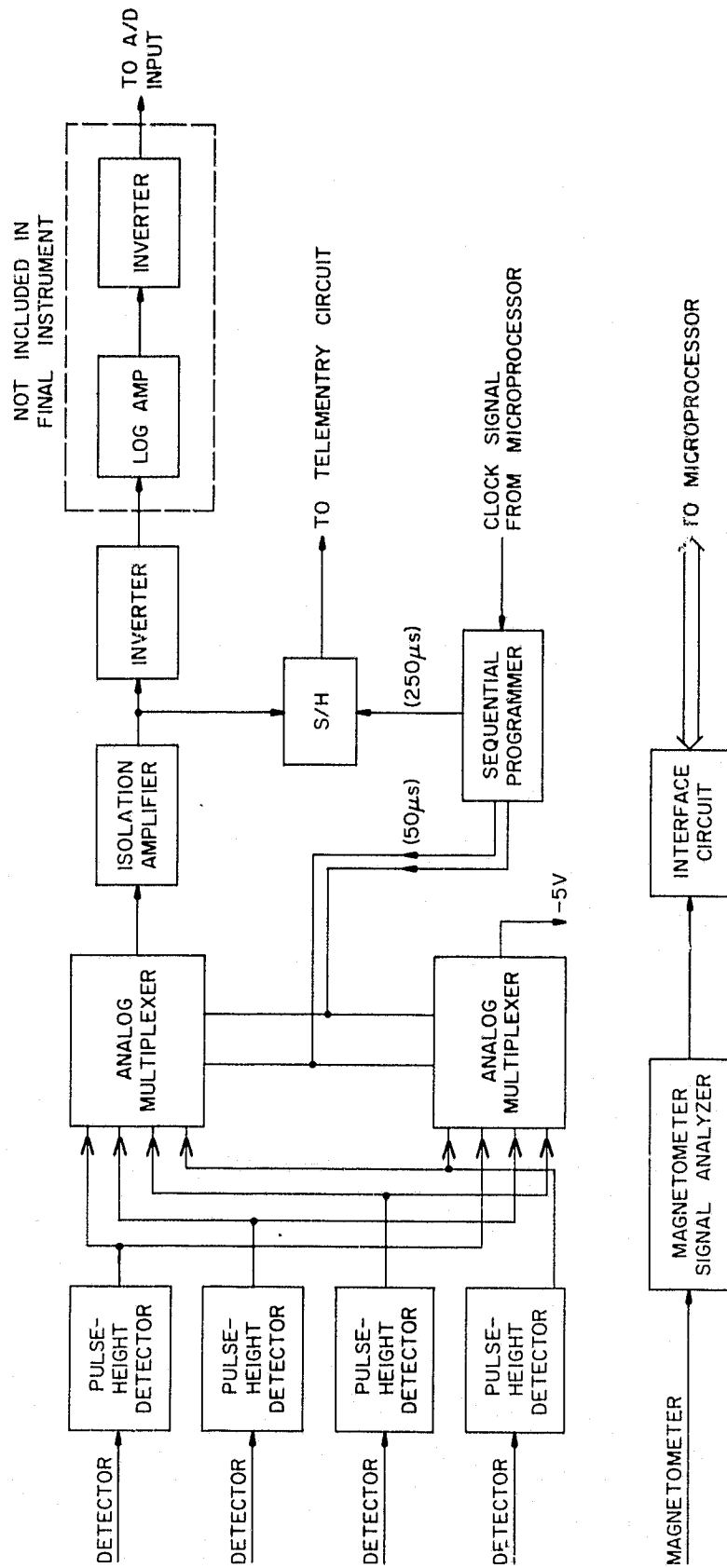
Figure 2.4 The block diagram of the pulse-height analyzer
[*Leung et al.*, 1979].

the time required to cycle through all four channels to be T, then each pulse-height detector holds the peak level of the largest pulse that occurred during an interval of length $3T/4$. In this case $T \approx 200$ μs. For the next $T/4$ interval the pulse-height detector is reset in preparation for the next sampling interval. The measurement times are staggered for each of the detectors.

The data sample is routed through two data collection paths. The analog level goes through a sample and hold, and then to a telemetry circuit; this provides an analog output with very good resolution. The other branch includes the A/D converter and microprocessor, Figure 2.5. The sample and hold provides higher amplitude resolution than the microprocessor, but provides data at 1/5 the rate.

The microprocessor stores the digitized data sample (5 bits), a code from the sequential programmer that identifies the detector (2 bits), and the magnetometer signal (4 bits), which provides azimuth information. The microprocessor then sorts the data according to azimuth, detector number, and increments the counter (5 bits) corresponding to the appropriate energy level.

The azimuth of the rocket is measured by the magnetometer and digitized to provide sixteen sectors. When the microprocessor outputs data, it transmits data in sixteen blocks corresponding to the sixteen azimuth sectors. Each of these blocks of data is preceded by a pulse identifying the sector. Then energy spectrum for each of the four channels is transmitted. Figure 2.6 shows the output corresponding to sector 15. The first few channels of the detectors show a large number of counts, this is due to the noise of the preamplifier and detector. The energy spectrum will display up to 32 counts for sixteen energy bins, each bin corresponding to a certain range of energy. The time scale in the plot corresponds to energy level since the count rates for each energy level are output sequentially.

The first-in first-out (FIFO) memory is included to act as a data buffer; this prevents data from being lost while the microprocessor performs sorting operations and transmits data back to the ground.

The deck containing the linear electronics (detectors, preamps, and shaping amplifiers) is shown in Figure 2.7. The deck containing the non-linear electronics (pulse-height detectors, analog multiplexer, sample and hold, and microprocessor system) is shown in Figure 2.8.
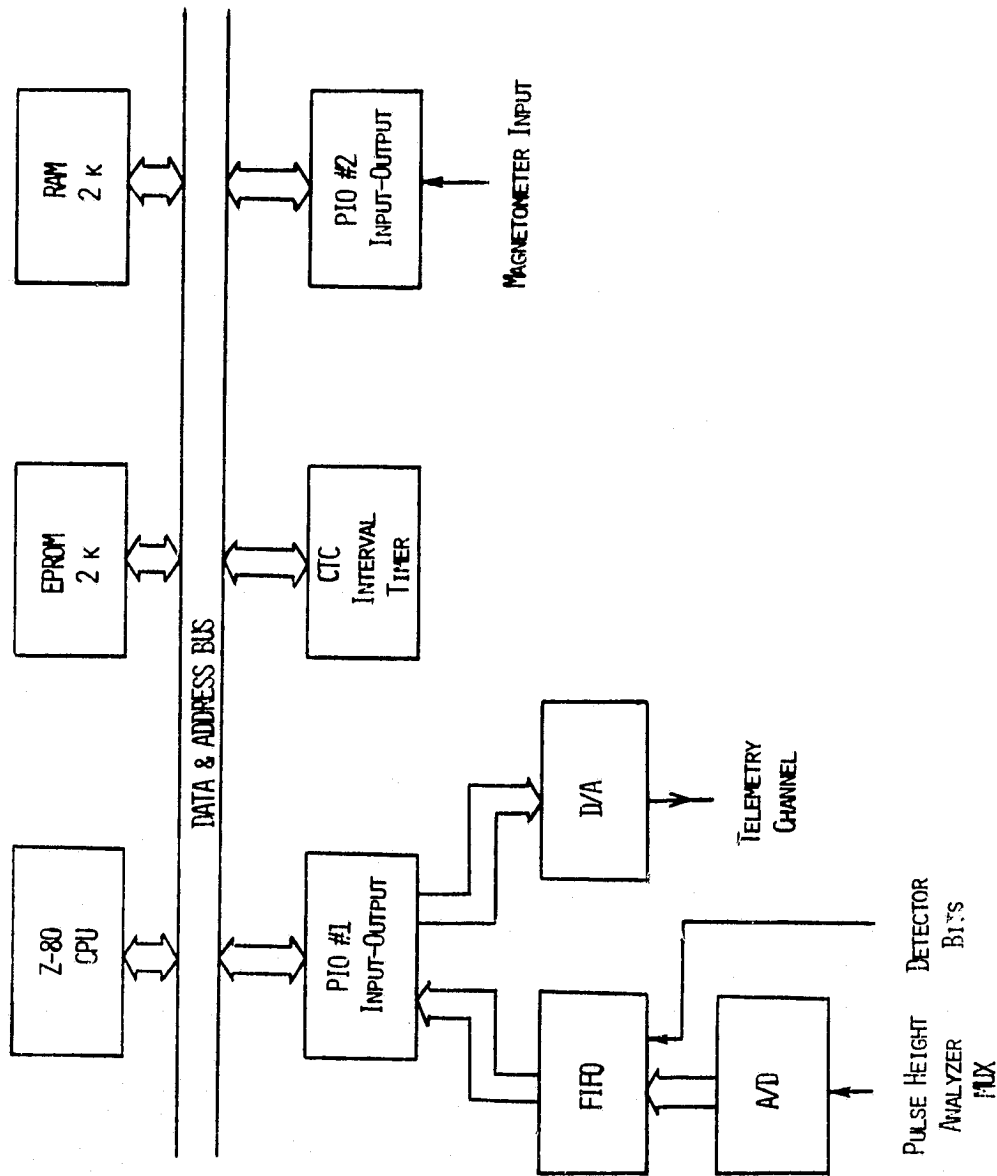
Figure 2.5   Microprocessor data manipulation experiment.
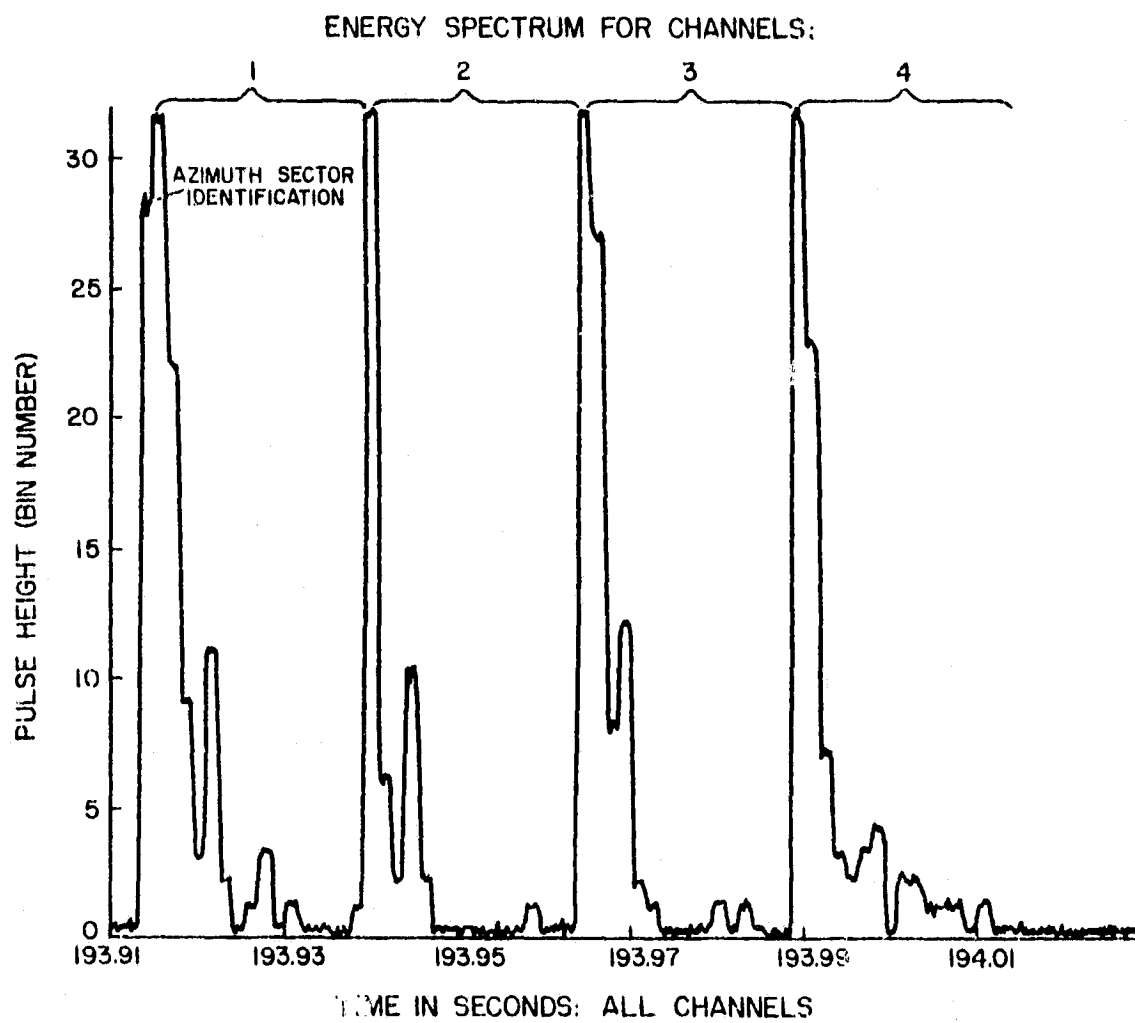
Figure 2.6 A typical block of data obtained from the micro-
processor for one azimuth sector (sector 15).
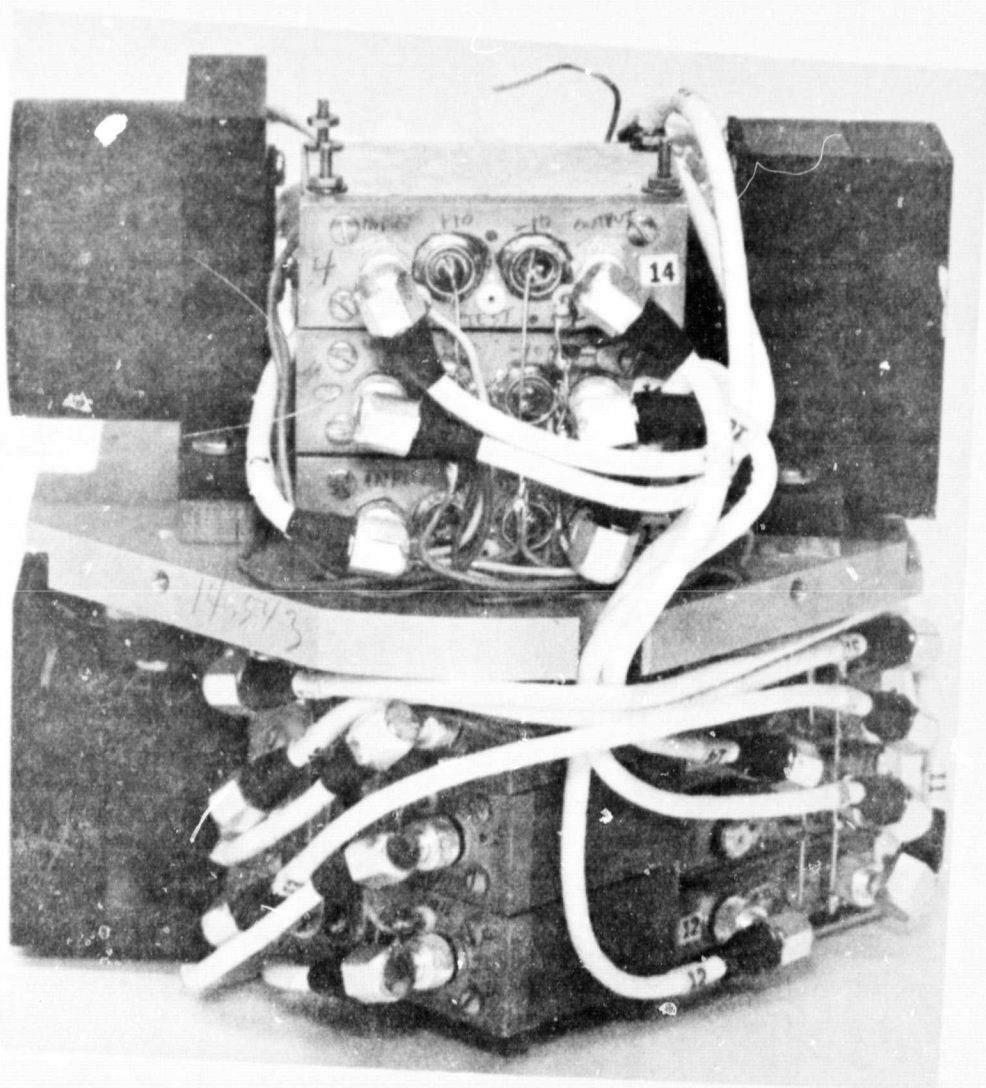
Figure 2.7 The linear electronics deck. The detectors are mounted in the black structures on the right and left sides of the deck. The six preamplifiers are mounted in two groups of three. The four shaping amplifiers can be seen in the lower right-hand corner. The deck is six inches in width.
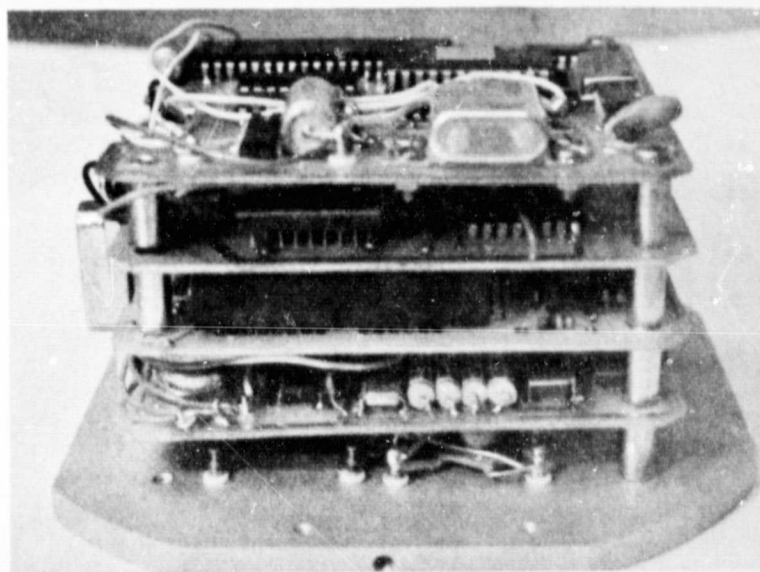
Figure 2.8   The non-linear electronics deck.   The lower card contains
the pulse-height analyzer.   The remaining cards are
associated with the microprocessor.

The pulse-height analyzer is discussed in *Leung et al.* [1979]; the data-manipulation system is described in detail in *Davis et al.* [1979].

3. SURFACE-BARRIER DETECTORS

3.1 *Introduction*

Many devices are used in rocket-borne applications to detect energetic particles: solid-state detectors, scintillators, and gaseous ionization detectors are some of the simpler types available. More complex instruments are needed for energies below about 10 keV. These include a group using magnetic or electrical deflection for energy discrimination (the analyzer). This is followed by a detector which uses electron multiplication, whether with discrete dynodes or without (e.g., the channeltron). A description of these detectors is found in *O'Kelley* [1962].

The solid-state detector is well suited for rocket experiments because it is small, rugged, has high resolving power and operates with relatively low voltages. An incident particle travels through the semiconductor crystal releasing its energy by interactions forming electron-hole pairs. The voltage applied across the detector produces an electric field which sweeps out the carriers produced by the energetic particle, resulting in a short current pulse. The energy lost during electron-hole pair formation is about 3.5 eV for silicon; this is an order of magnitude smaller than for a gas, providing better sensitivity.

From this description of the operation of a solid-state detector it would seem that a homogeneous silicon crystal could be used as a detector; however, there are practical difficulties with this approach. The direct current through the detector must be limited because the fluctuations in the current, due to its formation from discrete electrons, appear as noise superimposed on the desired signal. At room temperature the resistivity of intrinsic silicon is too low for it to be useful as a detector. A crystal which has been prepared using lithium drift techniques (to compensate for the impurities that remain, even after careful processing) will have resistivity high enough to be useful if cooled to low temperatures (70-80°K). Because of the costs involved these are not used unless a large sensitive volume is required [*Deme*, 1971].

The use of a reverse-biased diode allows a high bias voltage, resulting in a high electric field, while keeping a low reverse leakage current for improved noise performance. The surface-barrier diode, using a metal-semiconductor junction, is easier to construct than a diffused diode because of the elimination of the diffusion process.

The properties of surface-barrier detectors are discussed below and results that will be used later will be developed in detail. Consult *Bertolini and Coche* [1968] for an advanced analysis of solid-state detectors. It should be noted that diffused diodes have much in common with the surface-barrier diodes and many of the results below are applicable to diffused detectors.

A typical solid-state detector is shown in Figure 3.1. This is the type used in the energetic particle spectrometers used in Nike Apaches 14.542 and 14.543.

3.2 *Electrical Characteristics*

The surface-barrier diode, sometimes called a Schottky barrier diode, uses a metal layer deposited onto an n-type, or p-type silicon crystal. The doping of the silicon depends upon the metal used; one type of doping will result in ohmic contacts and the other will result in diode properties [*Hunter*, 1962]. A diode is formed by using gold with n-type silicon; or aluminum with p-type silicon. A depletion layer forms in the silicon at the barrier, as shown in Figure 3.2. Schottky's theory for metal-semiconductor junctions neglects the surface effects of the semiconductor, which must be considered in order to match observed results. However, a model developed with Schottky's theory can provide information on expected variations and various results are summarized below. The detector is used with a reverse bias on the junction. This ensures rapid removal of the electron-hole pairs from the depletion layer. The bias (typically 100 V) is not, however, large enough to cause avalanche multiplication (breakdown). A detailed development of metal-semiconductor interfaces can be found in *Carroll* [1974] and *Milnes and Feucht* [1972].

3.2.1 *Leakage current*. The properties of the junction for a metal-semiconductor diode are described in terms of the work function of the metal and the electron affinity of the semiconductor. The current through the diode follows the p-n junction I-V characteristic

$$I = I_s[\exp(qV/kT)-1] \tag{3.1}$$

where

V is the applied voltage

T is the temperature

I_s is the reverse saturation current
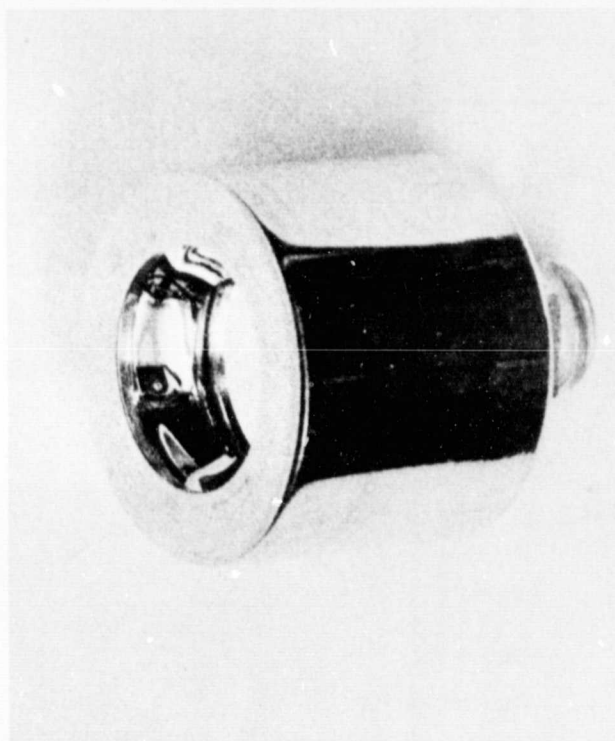
Figure 3.1   The Ortec ruggedized surface-barrier detector.   The sensitive
            area is 50 mm^2, the depletion depth is 100 μm.   The detector
            operates with a reverse bias of 120 V and has a noise width
            of 6 keV at 25 °C.
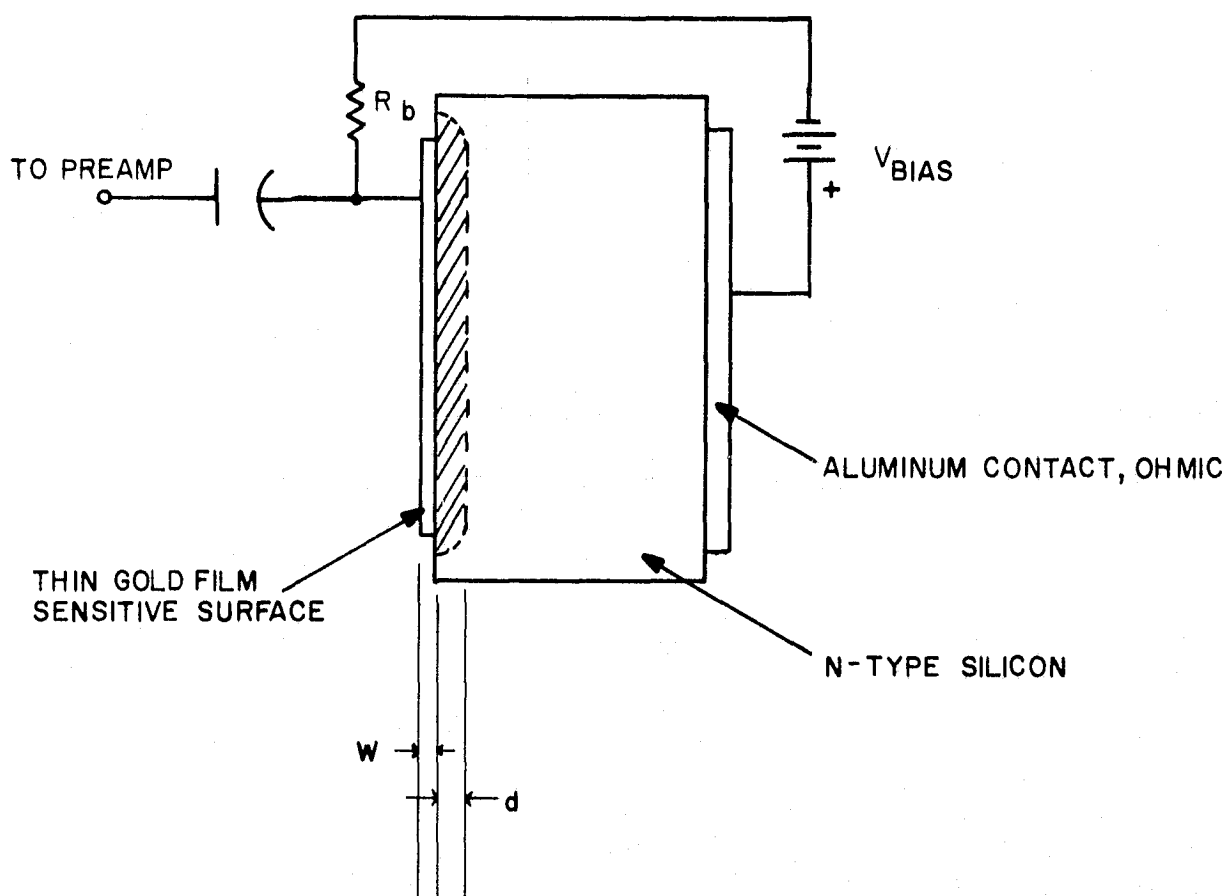
Figure 3.2   Illustration of surface barrier diode. The width of the
surface metal is indicated by W. The depletion layer width
(sensitive depth) is indicated by d and is on the order of 100 μm.

The value of kT is 0.026 eV at room temperature. With the large reverse bias encountered with solid-state detectors the reverse current is approximated as I_s.

The leakage current provides some insight into the temperature dependence. The leakage current density is given by

$$J_o = \frac{4\pi}{h^3} qm^* \, k^2 T^2 \, \exp(-\phi_B/kT) \tag{3.2}$$

where

ϕ_B is the barrier height

m^* is the effective electron mass

Because of the exponential term the leakage current is very sensitive to temperature.

3.2.2 *Depletion region.* The width of the depletion region with the reverse bias applied is important for several reasons. The incident particle must lose all its energy within the depletion region in order to yield valid energy information. The range of energetic particles in silicon and germanium for given energies has been investigated and is available from many sources [for example, *Deme,* 1971]. With this knowledge we can determine the minimum bias required to measure a certain energy, or determine the maximum measurable energy for a detector with a specified maximum bias. The width of the depletion layer is also important in determining the junction capacitance, which is approximated by a parallel-plate capacitor. The maximum field strength allowed in silicon (to avoid avalanche breakdown) is related to the depletion layer width and the applied bias. The depletion layer thickness for a reverse bias voltage V is given by

$$d = [2\varepsilon\varepsilon_o \mu\rho\,(V+V_o)]^{1/2} \tag{3.3}$$

where

ρ is the resistivity of the doped semiconductor

μ is the electron mobility of the doped semiconductor

V_o is the contact potential

ε is the relative dielectric constant of the material

ε_o is the permittivity of free space

Using the formula for a parallel plate capacitor the junction capacitance for a detector with surface area A is

$$C_J = A\varepsilon\varepsilon_o [2\varepsilon\varepsilon_o \mu\rho (V+V_o)]^{-1/2} \tag{3.4}$$

3.2.3 *Dead zone*. There is a layer on the surface of a semiconductor detector where energy lost by the incident particle will not contribute to the measured energy. This is the dead zone. For surface-barrier diodes the dead-zone thickness is roughly equal to that of the metal layer.

The amount of energy lost in the dead zone depends upon the distance a particle must travel before it reaches the depletion region. Particles with a large angle of incidence (measured relative to the normal) travel a greater distance through the dead zone and lose more energy than particles entering normal to the detector. The thickness of the dead zone can be determined by measuring the energy losses for different angles of incidence. The dead zone introduces a limit on the energy resolution and some uncertainty in measured energy because of variation in angle of incidence.

The presence of the dead zone can be used to aid in determining the type of charged particle present if more than one detector is used. This is a feature of the experiment prepared for the payloads of Nike Apaches 14.542 and 14.543. The energy lost per unit distance traveled varies with the particle mass, charge and energy according to the following formula:

$$\frac{dE}{dx} \propto \frac{Z^2 M}{E} \left(\ln \frac{E}{M} + \text{constant} \right) \tag{3.5}$$

where E is the kinetic energy of the charged particle, x is the distance measured along the particle track, Z is the charge of the particle, M is the mass of the particle. Rates of energy loss are plotted for electrons, protons and alpha particles in Figure 3.3; this plot is for silicon, not a metal surface layer, but it illustrates the dependence upon particle mass and energy. If a detector is used with a very thin dead zone, then very little energy is lost in the dead zone for any particle. If a detector with a thick dead zone is used, then the resulting output would be similar to that of the detector with the thin dead zone if electrons are present, but much smaller if heavy particles such as protons or oxygen ions are involved. By including two detectors, one with a thick metal layer and one with a thin metal layer, in the same experimental package, it is possible to determine whether electrons or heavier particles are being measured.

As an example of how two different detectors aid in particle type determination, we will consider Figures 3.4 and 3.5. These are plots of
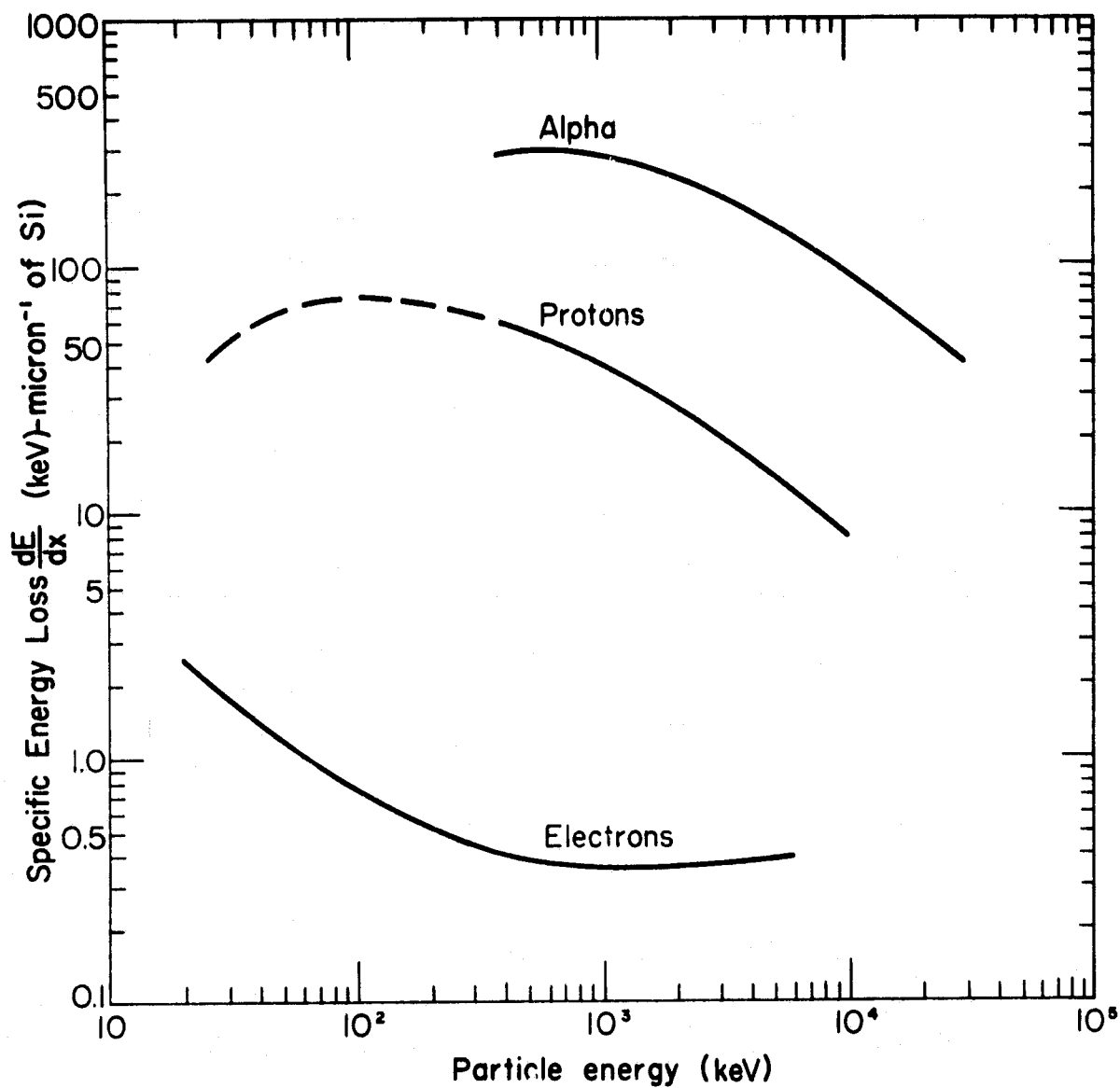
Figure 3.3 Specific energy loss for electrons, protons, and alpha
          particles in silicon. (Data replotted from *Sternheimer*
          [1959] and *Williamson and Boujot* [1962]).

I : 60 keV Am²⁴¹ RADIOACTIVE SOURCE
2:100 keV H⁻ IONS

PULSE HEIGHT ANALYZER CHANNEL

NUMBER OF COUNTS
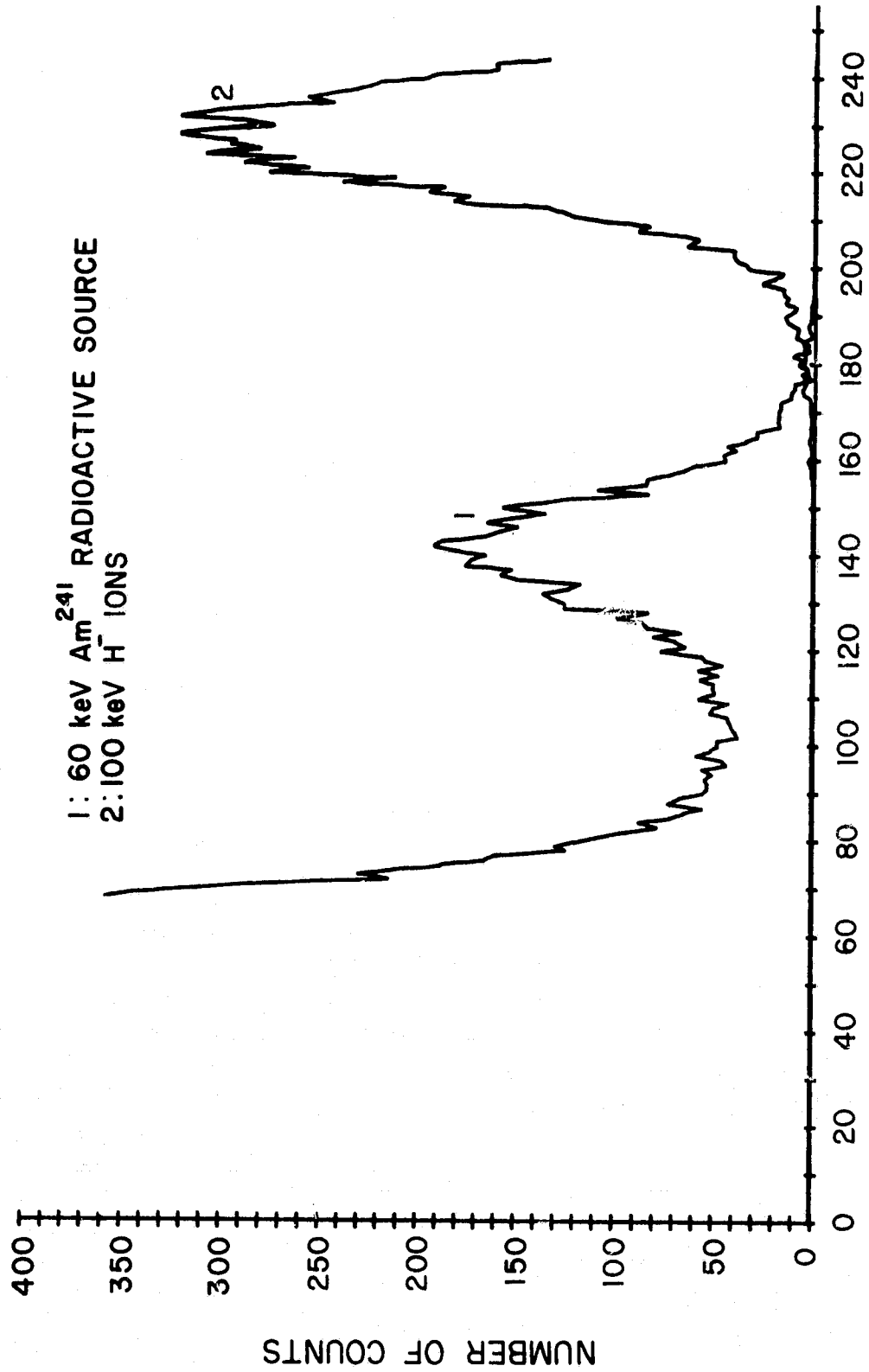
Figure 3.4 EPS intercalibration data for rocket 14.542 detector
1 down (40 μg cm⁻² Au).

1: 60 keV Am²⁴¹ RADIOACTIVE SOURCE
2: 100 keV H⁻ IONS

PULSE HEIGHT ANALYZER CHANNEL

NUMBER OF COUNTS
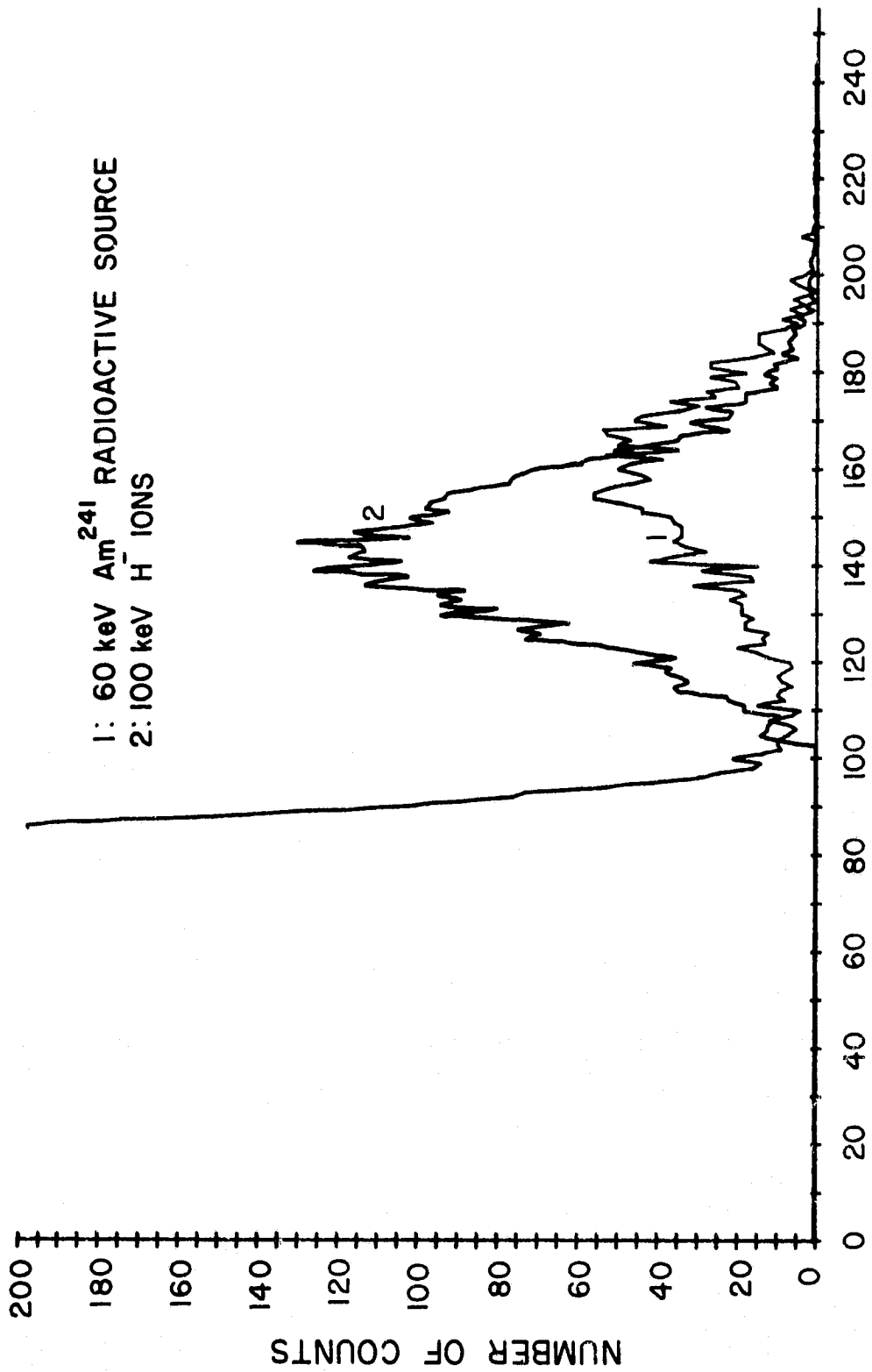
Figure 3.5 EPS intercalibration data for rocket 14.542 detector
2 up (100 μg cm⁻² Al).

pulse-height data obtained from a 256 channel pulse-height analyzer. The instrument is placed in a vacuum chamber and exposed to hydrogen ions (H⁻ in this case, due to practical considerations) from an accelerator, or gamma rays from an Am^{241} radioactive source. The radioactive source produces a 60 keV line that is used for intercalibration of the different detectors. The differences in the thickness of the dead layers will not affect the level of the signal pulse caused by the radioactive source. The pulse-height analyzer (PHA) channel corresponds to output voltage or particle energy; there is a linear relation between all these quantities. The number of counts is the number of times a particle of energy corresponding to a specific PHA channel was detected. The plot can be viewed as a relative probability density, with relative probability on the y-axis, and energy on the x-axis.

The data from the 40 μg cm^{-2} Au detector are shown in Figure 3.4. The pulses due to the 100 keV H⁻ particles are much greater in magnitude than the 60 keV pulses due to the Am^{241}; little attenuation is expected in the dead layer for a 40 μg cm^{-2} Au detector. Figure 3.5 shows the response of a 100 μg cm^{-2} Al detector for the same inputs. Here the dead layer produces a significant attenuation of the heavy H⁻ ions. If the particles had been electrons rather than H⁻ ions, the response of the 100 μg cm^{-2} Al would have been very similar to the response of the 40 μg cm^{-2} Au detector; the dead layer produces very little attenuation for electrons.

It will be shown in more detail in Section 3.4 that, by considering the magnitude of the difference in response of the two detectors, particle identification can be made.

3.2.4 *Channeling*. Silicon detectors are formed from single crystals of silicon and have a regular lattice structure. If an incident particle travels along the crystal parallel to planes of high symmetry (e.g., [111] and [110]), less energy is lost per unit distance (dE/dx) than for particles along paths not parallel to planes of symmetry. This is very important for detectors used in dE/dx applications where the dE/dx information is used to identify particle type, but of no concern if the total particle energy is absorbed, as in the present application.

3.2.5 *Pulse shape*. The output pulse of a detector is determined by the charge collection time and series resistance and capacitance of the detector circuit during the pulse rise, and the time constant of the input

circuit of the associated electronics during the pulse fall. The charge collection time is theoretically limited by the deceleration time of the incident particle; however, the depletion layer thickness, electric field strength, and carrier mobility are also important. High bias voltage and low resistivity material (to obtain the highest field strength) are necessary for a fast rise time. The plasma effect causes an increase in the pulse rise time: for a short time the electron-hole pairs tend to balance the effect of the applied electric field, the duration of this effect is called the plasma time. The net result is a lengthening of the rise time.

3.2.6 *Recombination*. As they are being swept out of the depletion region some of the electron-hole pairs may recombine, reducing the amplitude of the charge pulse. The probability of recombination can be reduced by increasing the bias voltage, thus reducing the collection time. A potentially more serious effect is trapping of charge carriers due to lattice defects or impurities. These tend to be non-uniform effects and the resulting charge pulse may be dependent on the path taken by the particle. The result of trapping can be a multiple-peaked signal resulting from a monoenergetic stream of particles.

Lattice defects caused by high energy particles are referred to as radiation damage. As a detector is used the lattice defects caused by radiation damage become more pronounced. The resolution decreases and becomes voltage dependent. With the short exposure and relatively low energy particles in rocket-borne applications the radiation damage is small. Surface-barrier detectors generally have lower levels of impurities than diffused detectors because the higher temperatures required during diffusion increase the mobility of impurities present during fabrication. This results in a higher resolution for barrier detectors due to fewer trapping centers.

3.2.7 *Model*. The electrical model for a reverse-biased detector is shown in Figure 3.6. The various elements will be described here and those important to the system noise performance will be discussed in greater detail in a later section.

The depletion region is modeled as a capacitance, C_p, with a shunt resistance, R_p. As with most diodes the resistance R_p is large. The leakage current is included as I_L; its value is primarily dependent on temperature and remains relatively constant once steady-state conditions are achieved. The current pulse introduced by a charged particle is indicated by $i_p(t)$.
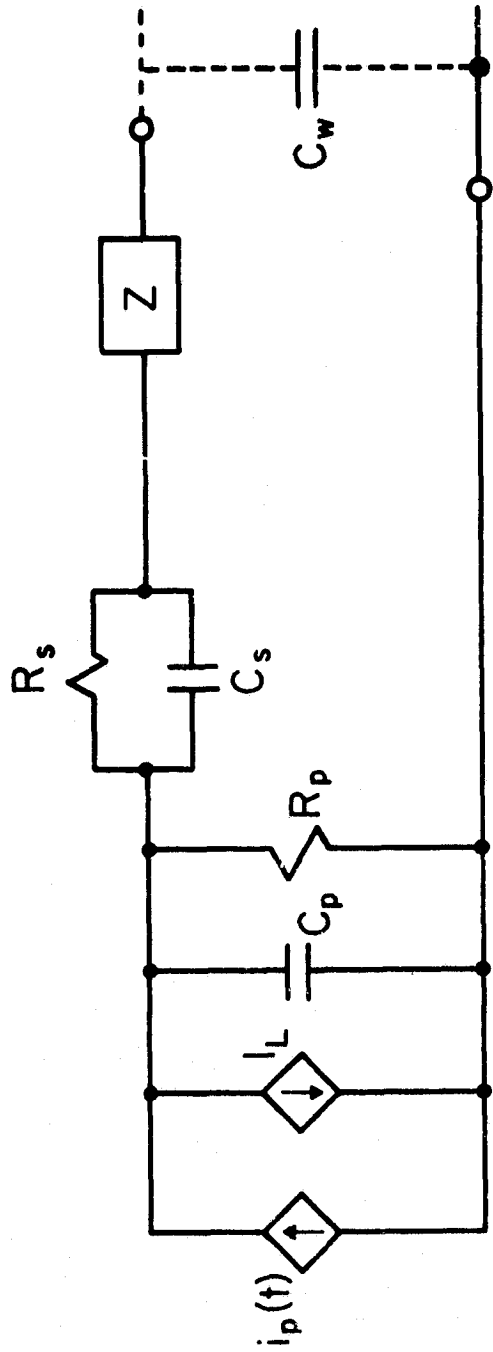
Figure 3.6   Detector equivalent circuit, $i_p(t)$ is the current introduced by an energetic particle, I_L is the leakage current, C_p and R_p are the parallel capacitance and resistance of the depletion region, C_s and R_s are the series capacitance and resistance of the semiconductor material, Z is the contact point impedance and C_w is the wire and connector capacitance [Voss and Smith, 1974].

Outside the depletion region the silicon presents a series resistance, R_s, shunted by a capacitance C_s. It would be more appropriate to treat this region as a distributed network rather than a lumped impedance; however, this representation is sufficient for a first-order model. The contact point is represented by complex impedance Z. This can influence the shape of the pulse and is very important at low temperatures. The coax connectors and connecting cable introduce some shunt capacitance, indicated by C_w.

The leakage current and depletion layer capacitance were discussed earlier. The parameters for the zone outside the depletion layer can be calculated with the equations shown below.

$$R_s = \rho\left(\frac{D-L}{A}\right) \qquad C_s = \frac{\rho\epsilon\epsilon_o}{R_s} = \epsilon\epsilon_o\left(\frac{A}{D-L}\right) \tag{3.6}$$

where ρ is the semiconductor resistivity, D is the total thickness of the silicon, L is the depletion layer thickness, and A is the cross-sectional area.

3.3 *Detector Mounting*

3.3.1 *Collimator.*
The detector mount and the collimator are an integral assembly. The collimator is used to limit and define the angular response of the detector. By reducing the detector's view angle one is able to measure the direction of arrival of the incident particles and problems relating to different distances traveled in the dead layer for various angles of incidence are reduced.

Since particle flux is the quantity of interest, we define the geometrical factor of the detector (including the collimator) to relate the observed count rate to the incident particle flux. That is

$$G \equiv N/\Phi \tag{3.7}$$

where G is the geometrical factor, N is the detector count rate per second, and Φ is the number of particles per square centimeter per second per steradian. In the derivation of geometrical factor we will assume that the incident flux is isotropic over the solid angle for which the detector is sensitive.

The collimator consists of a face plate with a circular hole parallel with the plane of the (circular) sensitive area of the detector. A cut-away view of a collimator is shown in Figure 3.7. The geometrical factor is a function of t, r, and R and is related to the effective area, A, by
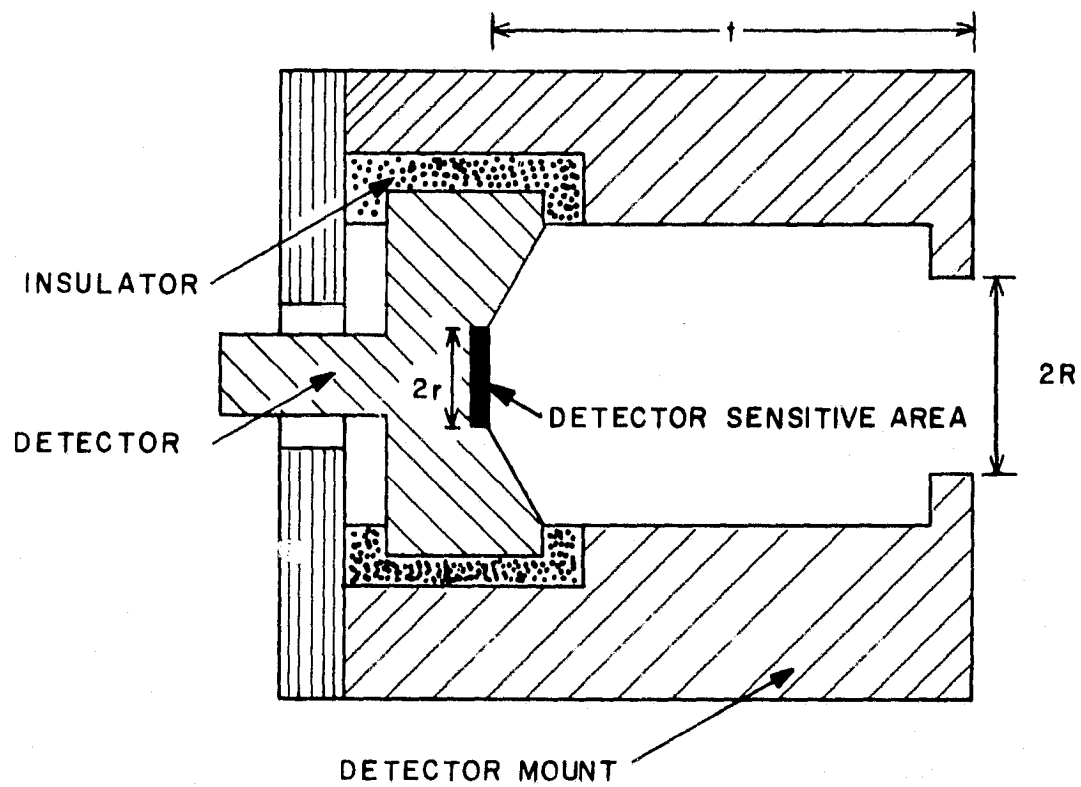
Figure 3.7 Cutaway view of collimator/detector mount.

$$G = \int d\vec{A} \cdot d\vec{\Omega} = \int dA \, \cos\theta d\Omega = A \int_{\theta=0}^{\theta_{crit}} \cos\theta d\Omega + \int_{\theta_{crit}}^{\theta_{max}} A(\theta) \, \cos\theta d\theta$$

(3.8)

where we have split the integral into two regions: when $\theta \leq \theta_{crit}$, because $r \leq R$, the entire surface area of the detector will be illuminated, as shown in Figure 3.8. In this case the illuminated area of the detector, the effective area, is constant $(A = \pi r^2)$ and can be removed from the integral. When $\theta_{crit} < \theta < \theta_{max}$, only a portion of the detector is illuminated, as illustrated in Figure 3.9. In this case the effective area is a function of θ and must be included in the integral. The calculation of the area $A(\theta)$ is rather involved when considered in general and may require the use of numerical techniques for evaluation. For a specific problem simplifications may be made that would allow direct evaluation.

The geometrical factors for the detectors flown on the JASPIC instrument and for detectors flown on previous flights were found numerically. The JASPIC detectors have a geometrical factor of 0.05 cm^2 ster; some of the detectors flown on previous flights had geometrical factors of 0.68 cm^2 ster. The quantity $A \cos\theta$ is plotted for both of the detectors mentioned above in Figure 3.10. It should be noted that the angular response of the JASPIC detectors can be modeled as being triangular.

The angular response of the detector and collimator assembly can also be found experimentally by plotting the count rate as a function of the angle of incidence for a monoenergetic beam of constant particle flux. One definition of angular response is the angle at which the count rate is half of the maximum rate (full width at half maximum).

3.3.2 *Environmental considerations.* Solid-state detectors are well suited for rocket-borne use; however, there are several items that must be considered to insure satisfactory operation.

Radiation damage (Section 3.2.6) can cause trapping centers to form which decreases the energy resolution and can lead to multiple peaking for a monoenergetic input. It is unlikely that any significant radiation damage would occur during a rocket flight since year-long satellite programs through radiation belts show only minor performance degradation. The effects of radiation damage should be kept in mind during laboratory measurements since the detector could inadvertently be exposed to very high energy particles.

34
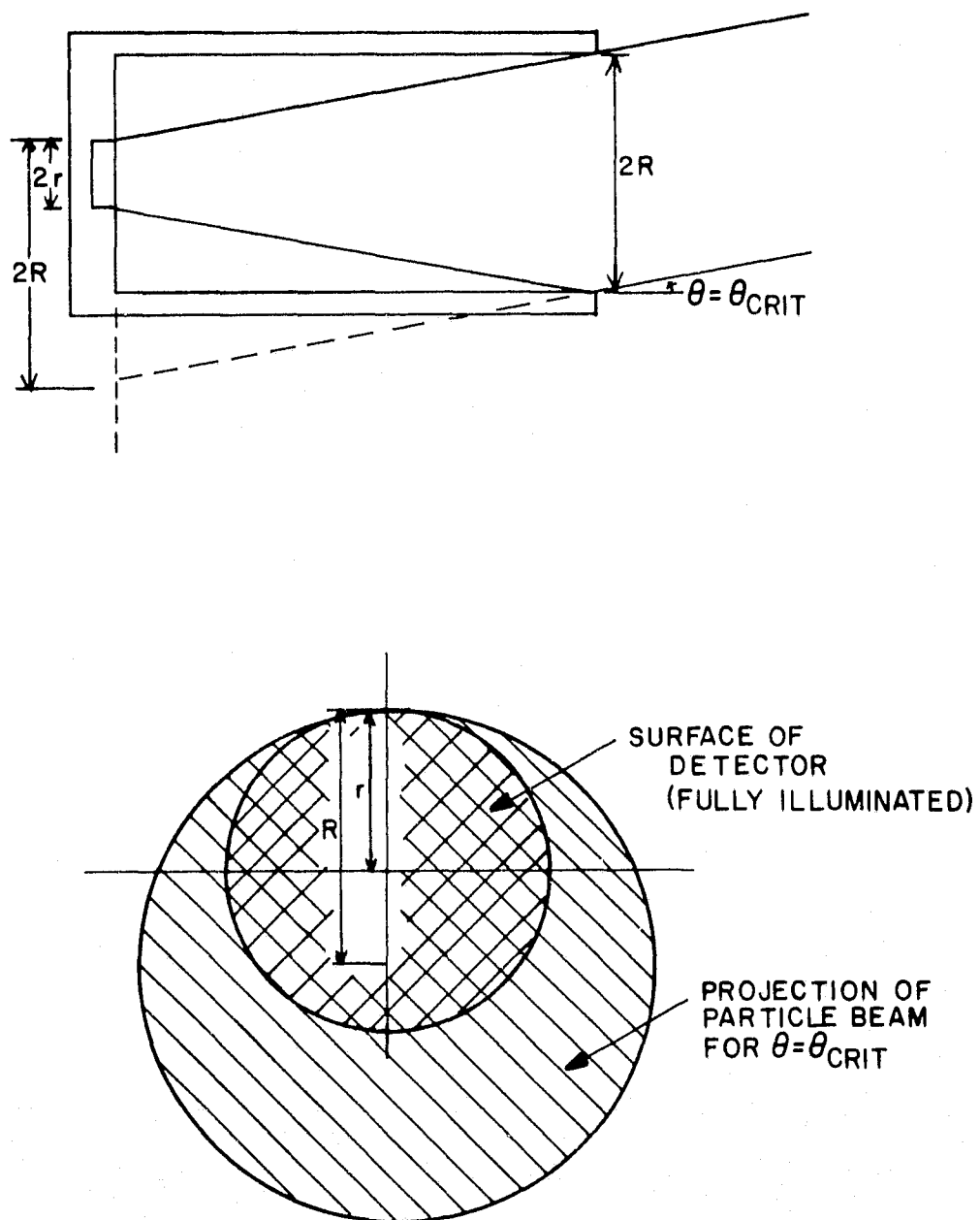
Figure 3.8   Illustration of illumination of detector for θ = θ$_{crit}$.

$a = t \tan \theta$

= DISPLACEMENT OF
CENTER OF IMAGE
FROM CENTER OF
DETECTOR

SURFACE OF DETECTOR

ILLUMINATED PORTION
OF DETECTOR, A

PROJECTION OF
PARTICLE BEAM
FOR $\theta_{CRIT} < \theta < \theta_{MAX}$
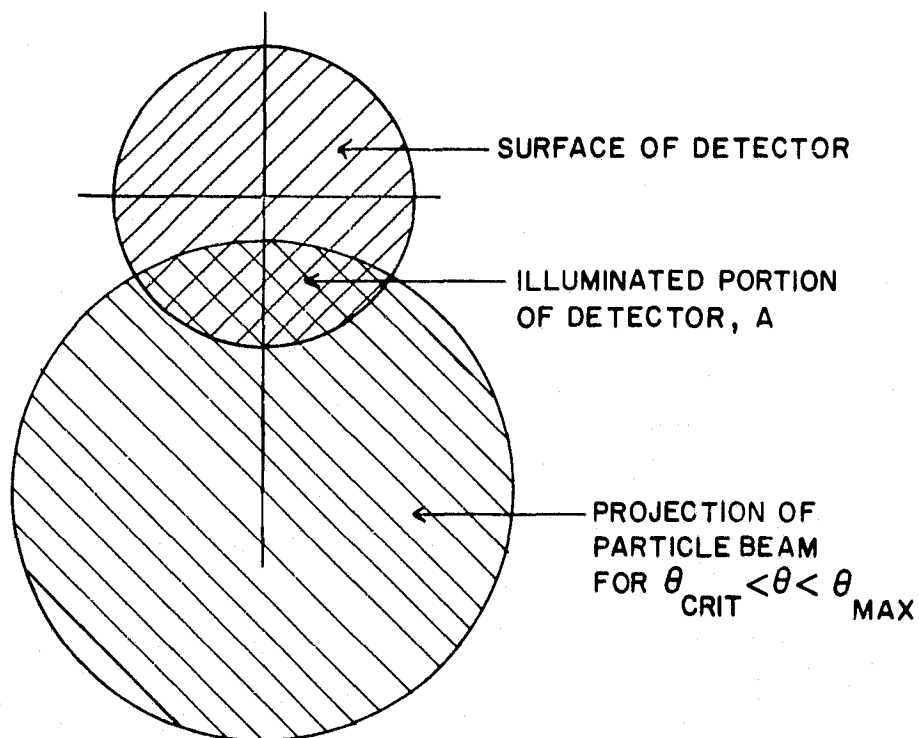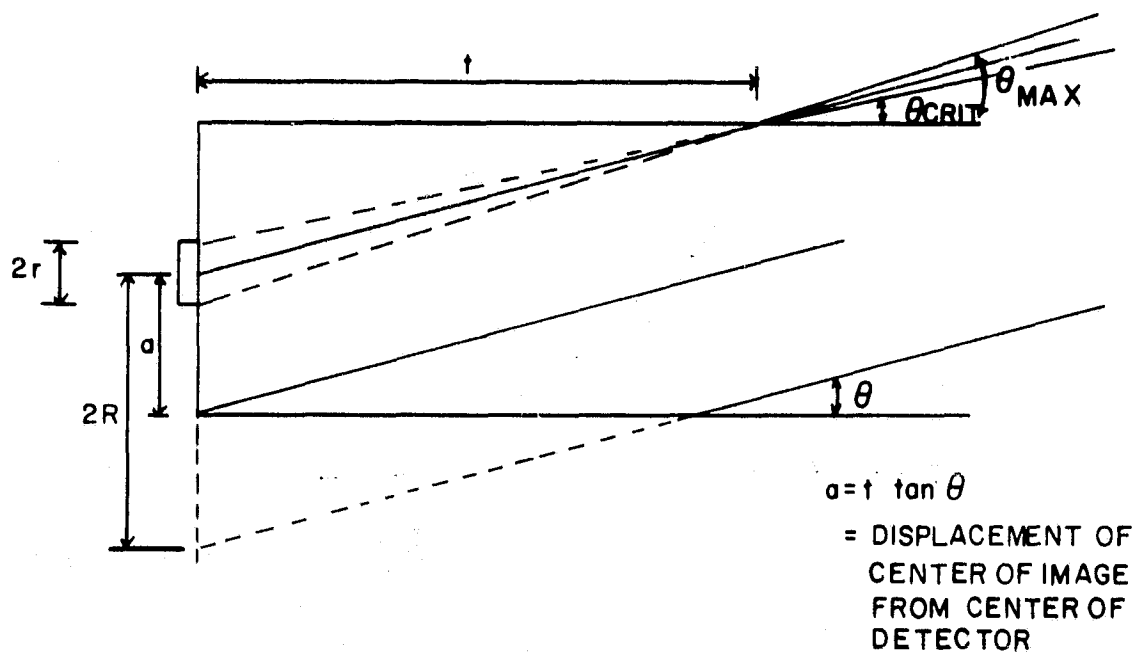
Figure 3.9   Illustration of illumination of detector for $\theta_{crit} < \theta < \theta_{max}$.
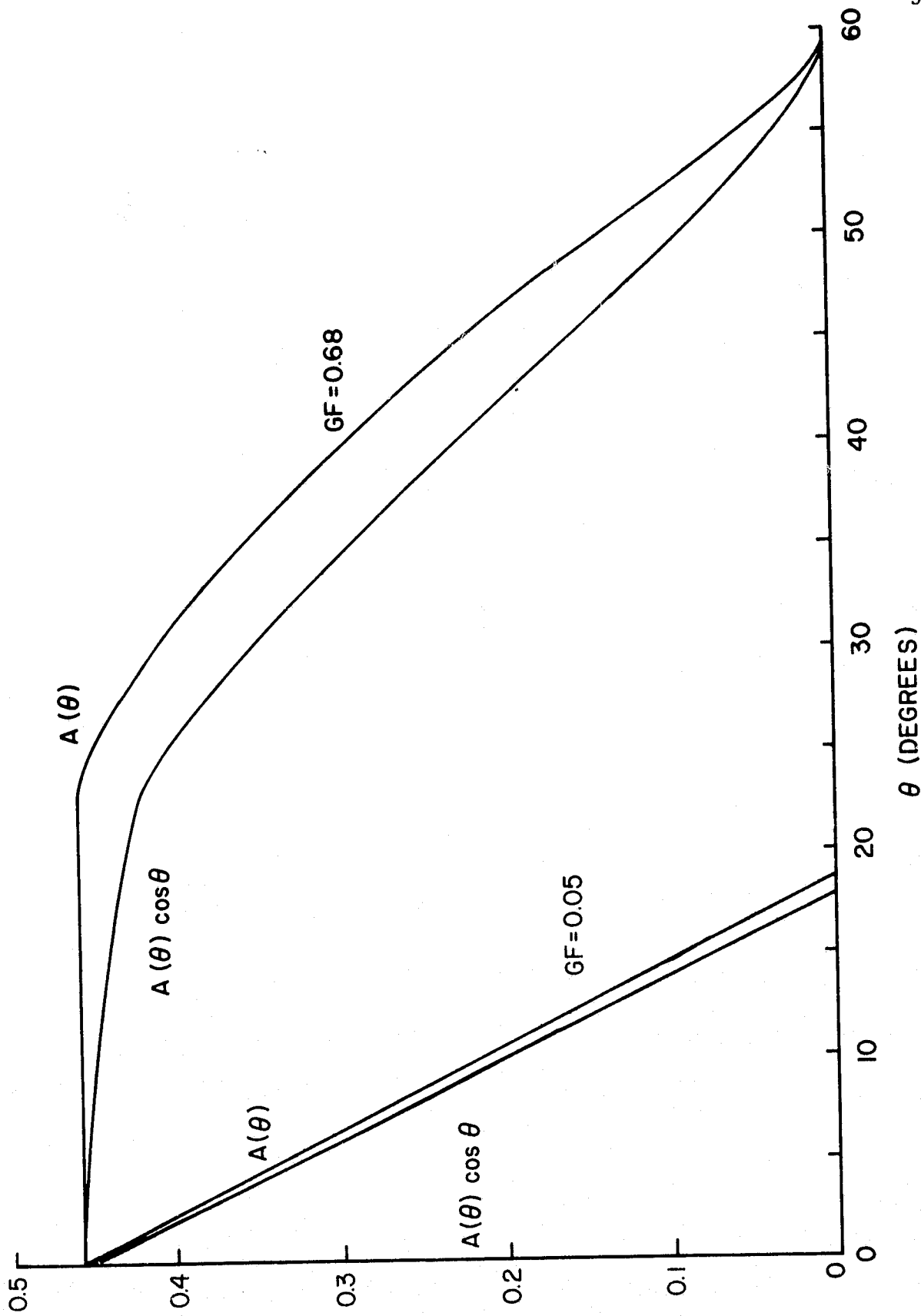
Figure 3.10 The relationship of A cos θ versus θ for two different collimators. The JASPIC collimator corresponds to GF = 0.05 cm^{-2} ster.

During the flight the detectors are in a vacuum; prior to the flight, however, care must be taken to keep the detectors in a dry environment. Moisture and ionizable impurities can cause an increase in the detector leakage current, thus an increase in noise. Contaminants can also react with the surface metal or silicon producing harmful effects. Figure 3.11 illustrates the effect of the atmosphere on detector noise performance. If the detector is exposed to a contaminant or is unused for an extended period of time, the bias voltage should slowly be increased allowing any contaminants to drift out of the depletion region. Because of the harmful effects of moisture, if a detector is cooled while operating in an atmosphere (e.g., in the laboratory or on the launch pad) precautions must be taken to prevent condensation on the detector. Also mercury diffusion vacuum pumps should be avoided because the mercury vapor reacts with the gold used in some of the detectors.

Mechanically the detectors are rugged enough for normal handling and launch. They are insensitive to pressure changes and reasonable temperature variation. If it is to be cooled to low temperatures, a special detector should be used so that the thermal coefficient of expansion is the same for the mount and the silicon, otherwise cracking may result.

Exposure to light will usually cause the detector to saturate. If the light consists of wavelengths (<1.12 nm) with photon energy greater than the band-gap of silicon (1.11 eV), it may excite carriers and contribute to the leakage current. Thin layer surface-barrier detectors are the most sensitive; for example, 40 µg cm^{-2} gold detectors must either be covered to keep light from reaching the detector, or used in darkness.

3.4 *Particle Identification using Multiple Detectors*

The detector dead zone and its application in particle identification was discussed qualitatively in Section 3.2.3. The use of a detector array will be quantitatively discussed in this section. Although a magnet can be used to reject electrons below a certain energy, as was done on one of the JASPIC detectors, this will not provide any additional information about the particle type. Identification using the dead zone will be discussed here.

3.4.1 *Theoretical calculations.* The specific energy loss, *dE/dx*, of energetic particles in a material depends upon the type of particle, the energy of the particle, and the material in question. The effect of the
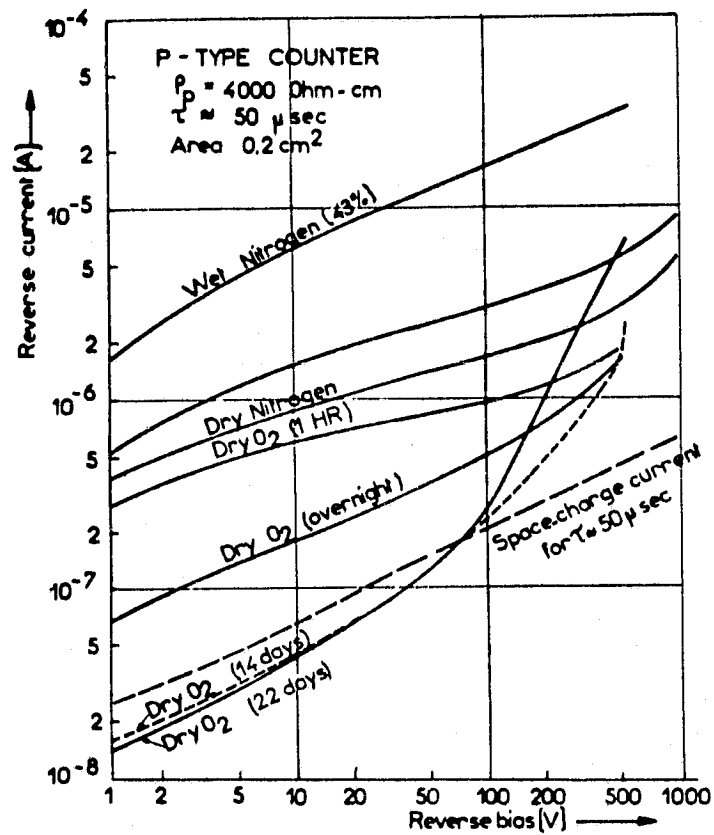
Figure 3.11 Reverse current versus reversed bias voltage showing the strong dependence upon the external air environment. Data taken by *Buck* [1961].

first two variables in silicon was presented in Figure 3.3. That is, the amount of energy that a particle will lose while traveling through the dead zone depends upon its mass and energy; in fact, the rate of energy loss changes as the particle travels through the dead zone and loses energy.

Specific energy loss, also called stopping power, has been measured for many particles and substances. Measurements and extrapolations from measurements are presented in *Northcliffe and Schilling* [1970]. The dE/dx values of interest are plotted in Figure 3.12. We see that the shape of the dE/dx curves, as well as the magnitude, vary with the type of material.

A functional representation was obtained for each of the curves in Figure 3.12 by using a fourth-order least-squares fit: we denote this function by $F(E)$. This function is different for each combination of particle and material. The specific energy loss is related to $F(E)$ as follows:

$$\frac{dE}{dx} = F(E) \tag{3.9}$$

We would like to find the energy of a particle leaving the dead zone (the energy that would be measured by the detector) as a function of the surface material, particle type, and incident particle energy. To obtain this result, equation (3.9) is integrated:

$$\int_{E_i}^{E_f} \frac{1}{F(E)}\, dE = \int_{0}^{x} dx = x \tag{3.10}$$

The function $F(E)$ is fourth-order polynomial whose coefficients are known. This has been numerically integrated for various values of F_i with $E_f = 0$; the results are given in Figure 3.13. These curves can be interpreted as giving the distance x (vertical axis) that a particle of incident energy E (horizontal axis) will travel before all of its energy is lost. The points marked are the result of the numerical integration. The curves that are superimposed represent a least-squares fit. At this point we have

$$\int_{E_i}^{E_f} \frac{1}{F(E)}\, dE = G(E_f) - G(E_i) = x \tag{3.11}$$

where $G(E)$ is the polynomial obtained from the least-squares fit to the curves of Figure 3.13. By rearranging equation (3.11) we obtain a relationship for
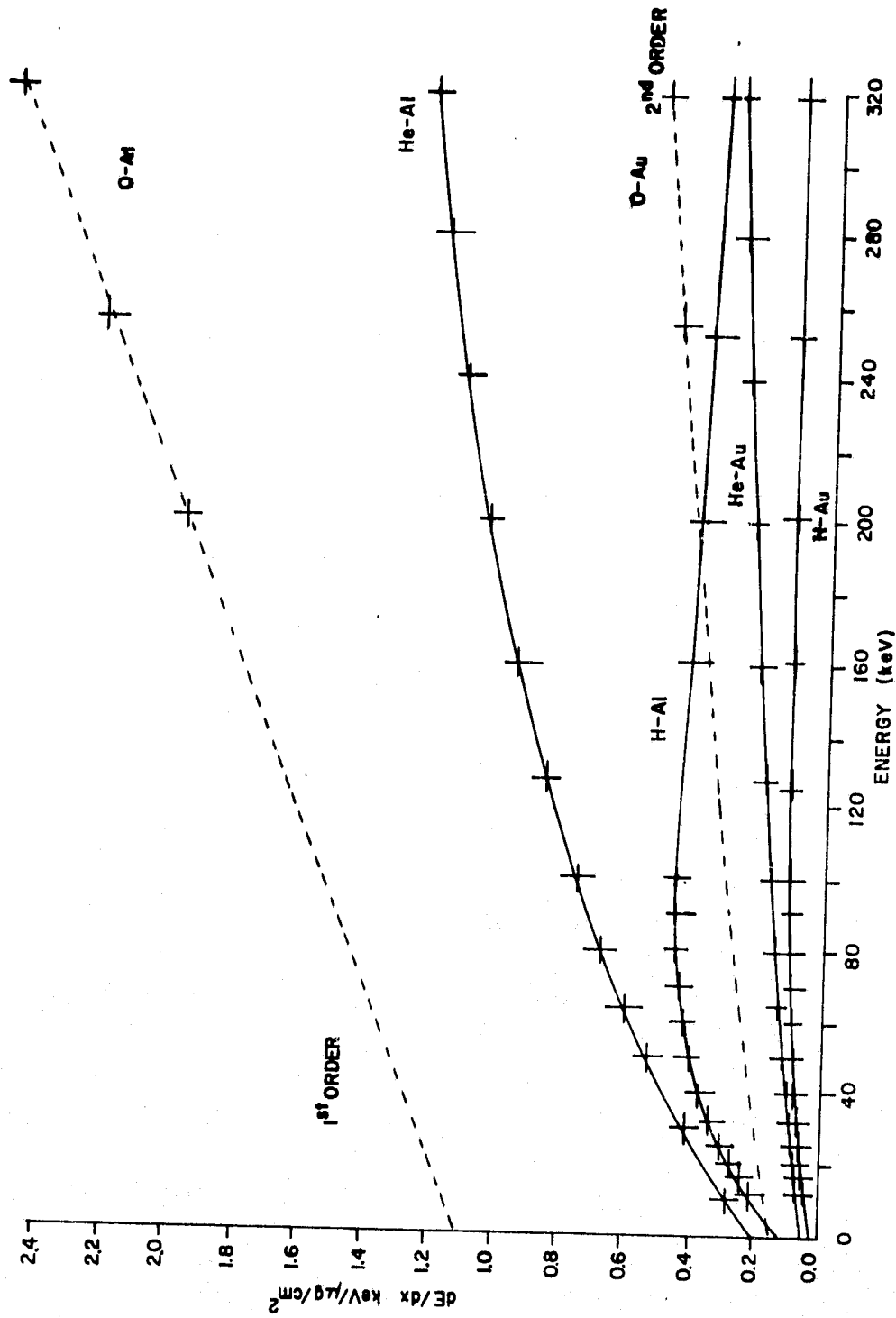
Figure 3.12 dE/dx values for various metals. Data points are obtained from measurements. The curves are least-squares fits to the data points.
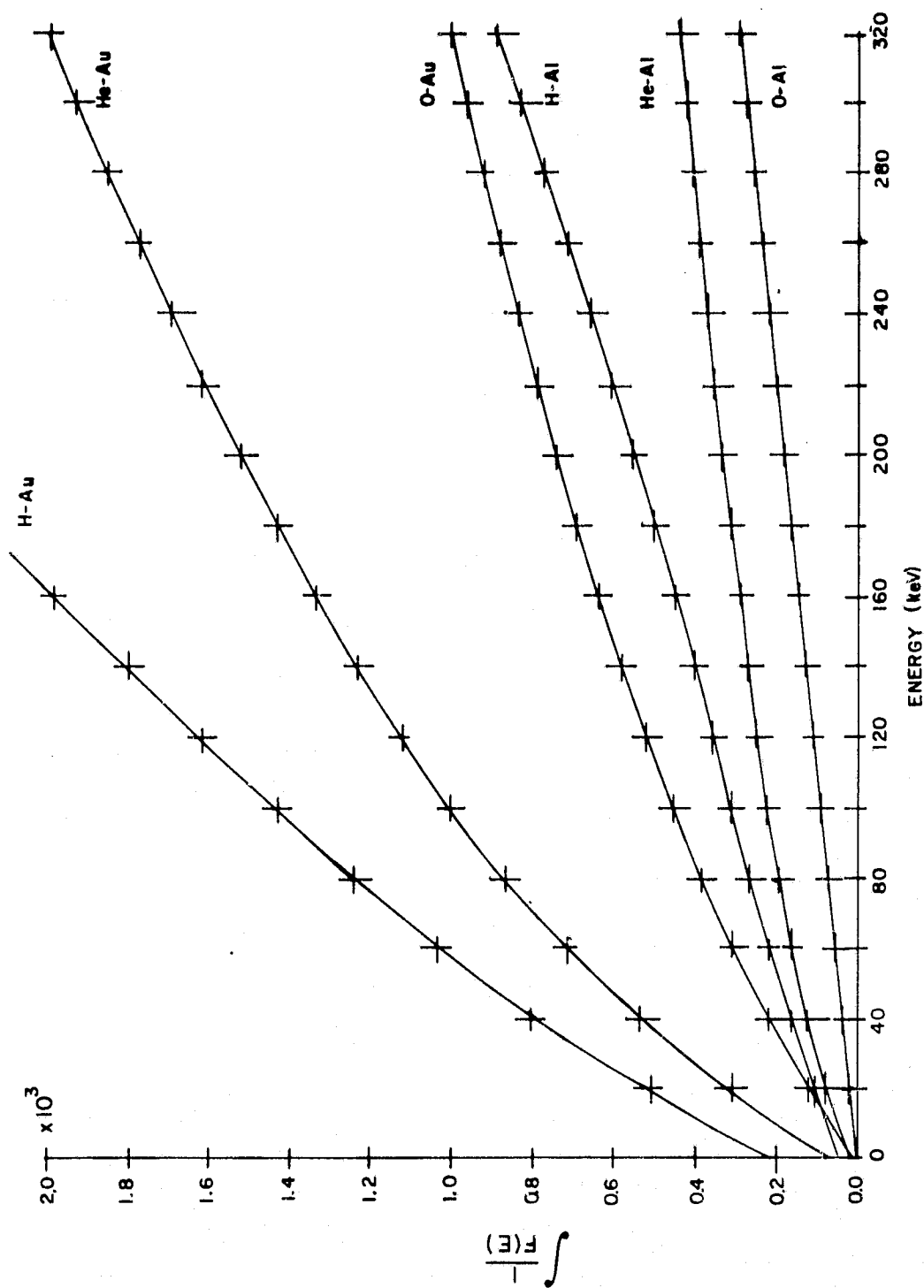
Figure 3.13 The results obtained from equation 3.10. The data points represent the results of numerical integration for various energies E. The curves are least-square fits to the data points.

the energy of the particle as it leaves the dead zone, E_f (final energy), given the incident energy, E_i, and the thickness of the dead zone, x:

$$G(E_f) = x + G(E_i) \qquad (3.12)$$

Since $G(E)$ is a second-order polynomial, we can solve for E_f using the quadratic equation. Plots can then be made describing the energy of a particle of a given incident energy at any point within the dead zone. Figures 3.14 and 3.15 are two plots of this type. Lines have been drawn indicating the thickness of the dead zone. Note that the dead zone thickness is actually a surface density; since this is how the surface material of the detector is specified it is convenient to work with this form of thickness or distance.

It should be noted that the loss mechanisms are non-linear. An incident oxygen particle with an energy of 150 keV will lose about 65 keV of energy; that is, it would be measured as an 85 keV particle. But for the same detector, an oxygen particle with 75 keV of energy would lose 50 keV in the dead zone; it would be measured as a 20 keV particle.

Since we are interested in particle identification by comparing the ratios of outputs from various types of detectors for a given unknown particle, the above data is in a form that is difficult to use. For a given input energy, the ratios of output energy of a given particle-detector surface material versus the actual particle energy can be plotted. This is shown for several different detector-particle combinations in Figure 3.16. The Au detector referred to as a reference has a surface layer of 40 μg cm^{-2}. In this plot the energy on the horizontal scale is the actual particle energy; for better accuracy the curves should be modified slightly so that the horizontal scale represents the energy that would be measured by a 40 μg cm^{-2} Au detector. The 40 μg cm^{-2} Au detector has very small dead zone losses; from Figure 3.15 we see that a 75 keV energetic proton would only lose 4 keV in the dead layer, as compared with 25 keV for a 40 μg cm^{-2} Al detector and 60 keV for a 100 μg cm^{-2} Al detector.

The next section describes the identification of an unknown particle using Figure 3.16; measurements taken during the instrument calibration are used.

3.4.2 *Experimental example*. The EPS was calibrated at Goddard Space Flight Center in Maryland. At this time the performance of the detectors
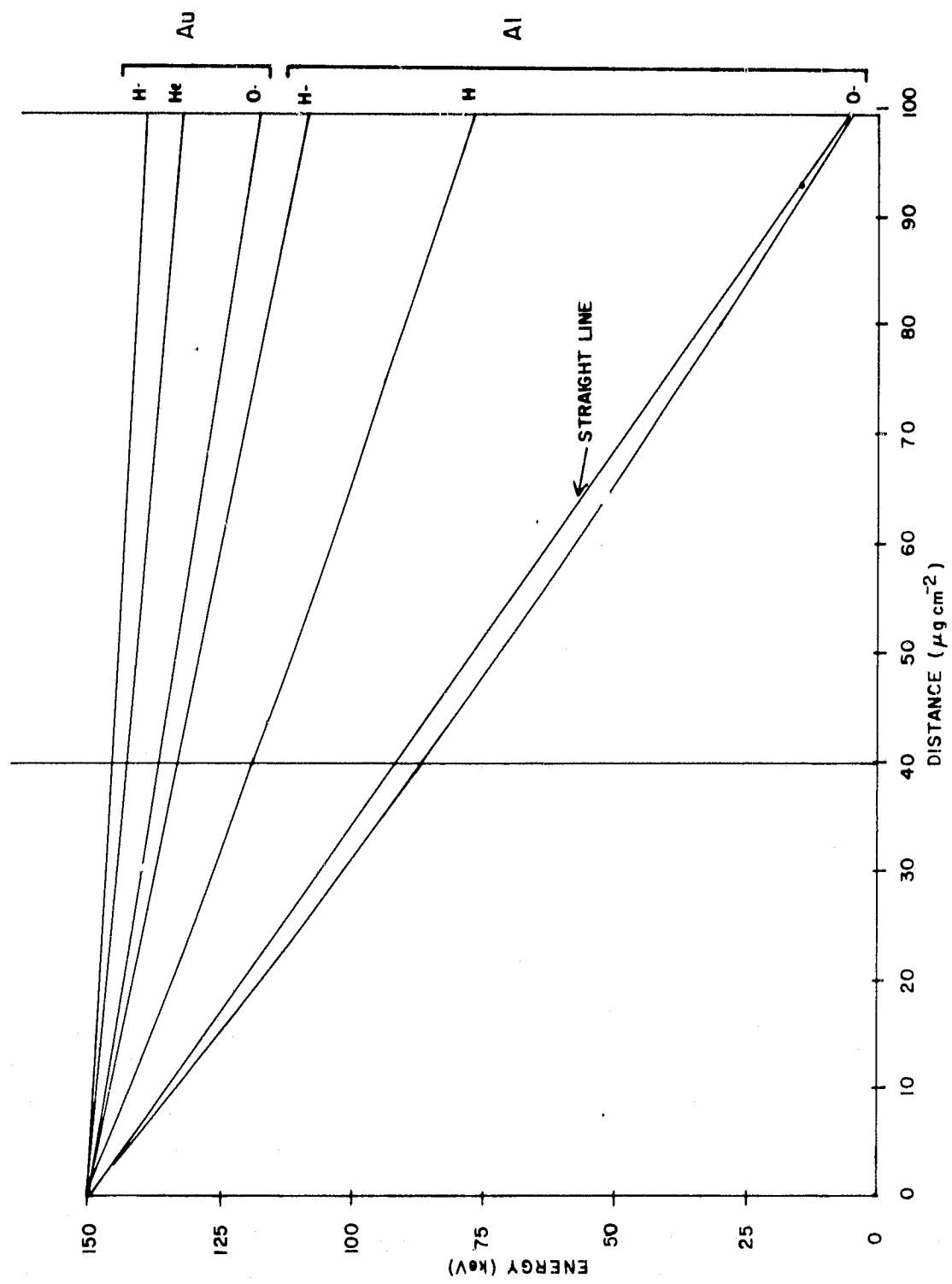
Figure 3.14 Energy of particle leaving the dead zone as a function of particle type, type of surface layer, and density of dead zone for 150 keV incident particles. Vertical lines indicate "distance" for a 40 µg cm⁻² and 100 µg cm⁻² surface layers.
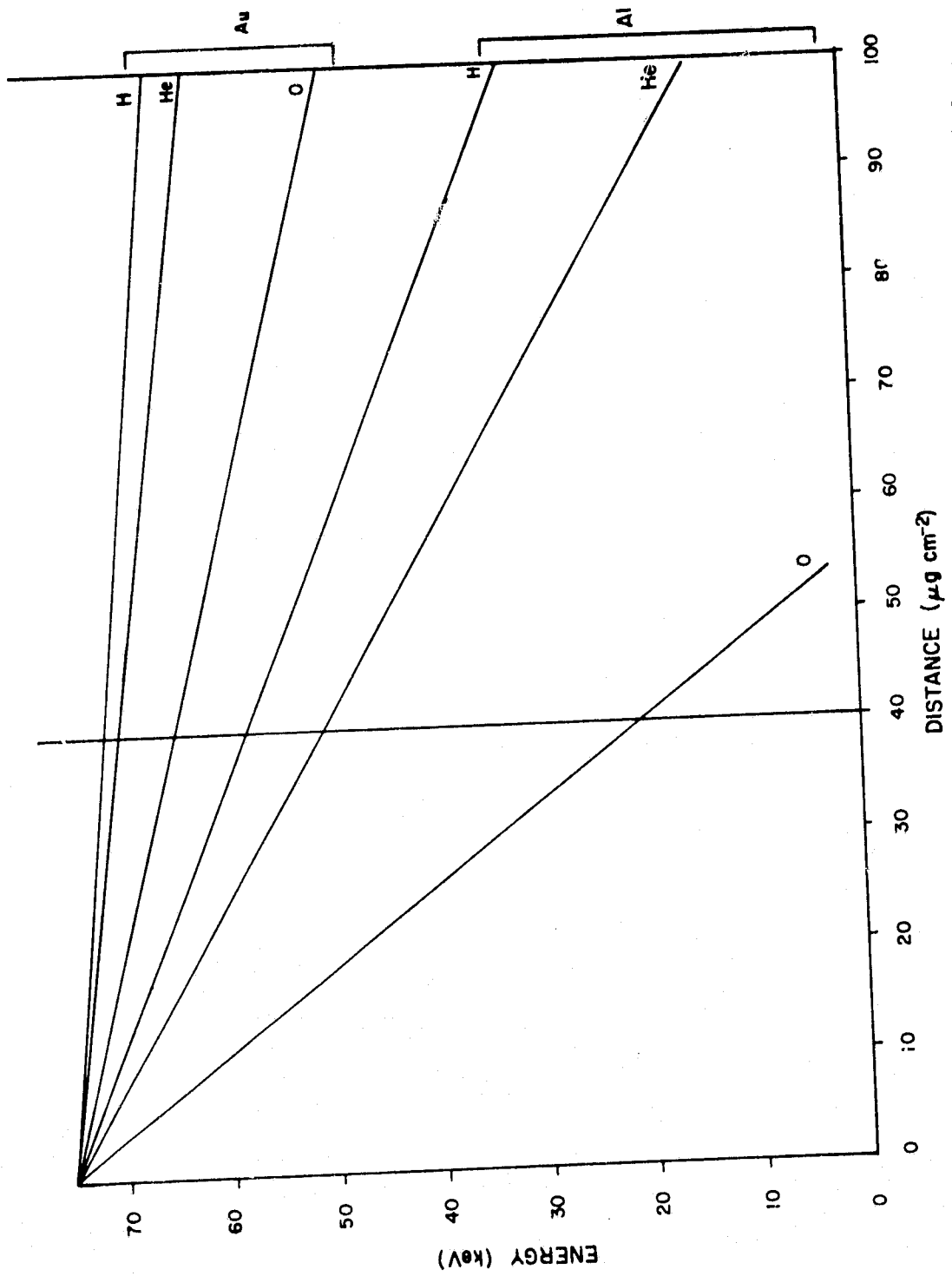
Figure 3.15 Energy of particle leaving the dead zone as a function of particle type, type of surface layer, and density of dead zone for 75 keV incident particles.
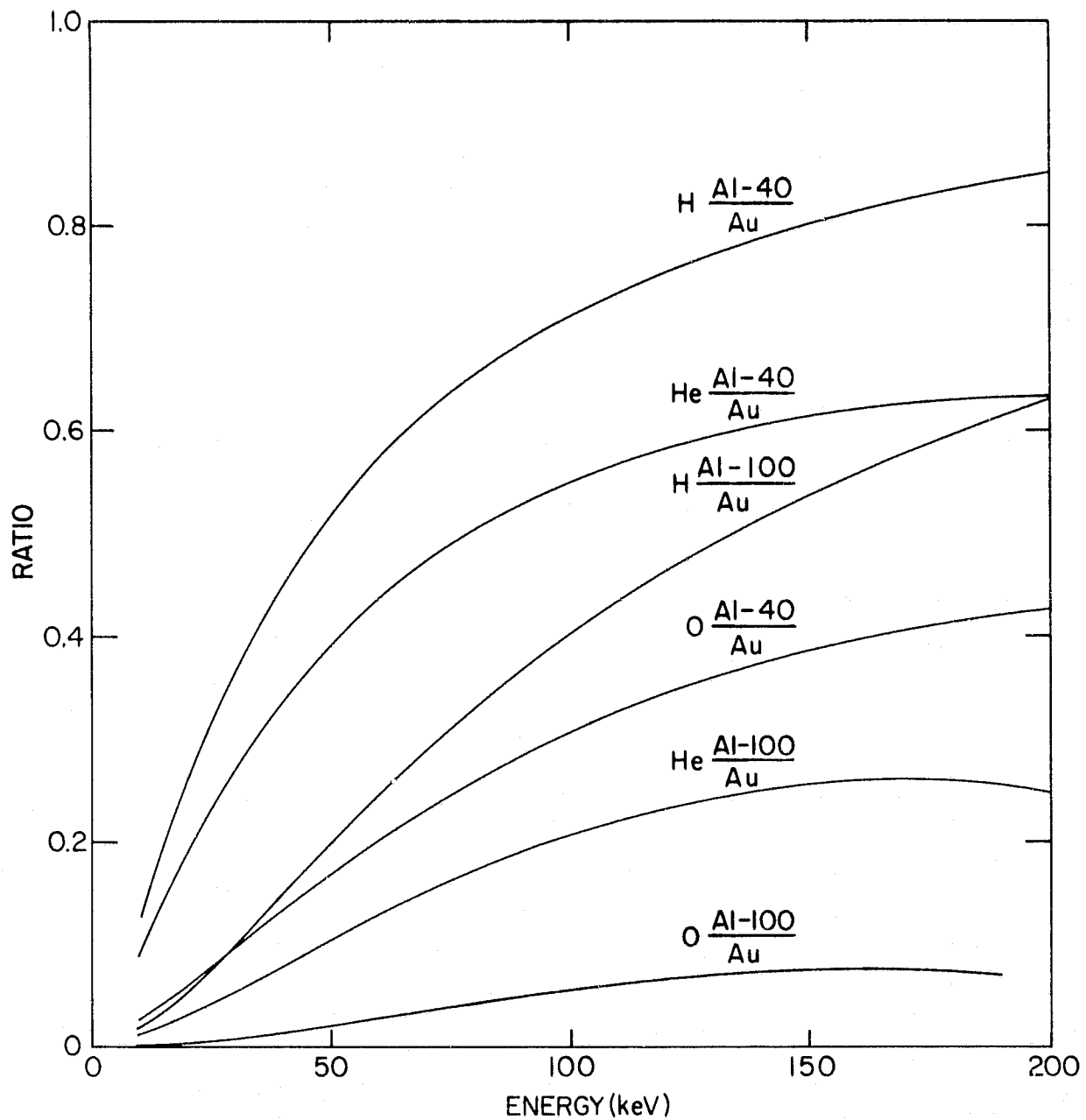
Figure 3.16 Ratios of fluxes recorded by detectors having different
metallic surface layers. For electrons the ratio is
unity (no attenuation).

and the electronics was checked. A 256-channel pulse-height analyzer, a very
low pressure vacuum chamber and a particle accelerator were available.
Some of the measurements taken included electrons and hydrogen ions (H^- in
this case) at various energies.

Figures 3.17 through 3.20 contain enough information to calibrate the
particle accelerator and to compare the ratio of energies obtained from the
EPS for H^- ions from 100 µg cm^{-2} Al detectors and 40 µg cm^{-2} Au detectors.
The data will now be described and then the particle identification will be
performed.

The data plots, Figures 3.17 through 3.20, were made using information
obtained from a pulse-height analyzer. The horizontal scale represents
energy level, or the pulse height. The vertical scale represents the number
of pulses that occurred with the energy level represented at that point on
the horizontal axis. Because of the noise in the system, the monoenergetic
particle flux produced a spread of measured energies. The actual particle
energy is the energy corresponding to the center of the spread. The plots
shown here show several different monoenergetic fluxes on one graph. The
line on the left of the plot for measurements using particles or the Ortec
signal generator denotes the noise of the EPS. The Am^{241} radioactive
source emits low energy particles and produces high count rates at low
energies; this causes the line described above to shift to the right and
is simply an indication of a high count rate.

The Am^{241} radioactive source produces 60 keV gamma rays that are used
to calibrate the EPS. Because the pulse-height analyzer channel zero does
not necessarily correspond to 0 V, some additional information is required
to use the PHA data; this is provided by an Ortec test generator. For a
more detailed description of EPS calibration see Chapter 6.

Unfortunately, test generator data were not available for detector 2 up.
For this reason the information contained in Figures 3.17 and 3.18 is used
to calibrate the accelerator. The Am^{241} source determines the channel that
corresponds to 60 keV. The Ortec test generator provided information on
the energy difference between channels (x channels per 20 keV),
Figure 3.17.

Using this information we go to Figure 3.18 to calibrate the accelerator.
Two accelerator scales are used (denoted high and low accelerator scales).
The energy displayed on the accelerator instruments differs from the actual
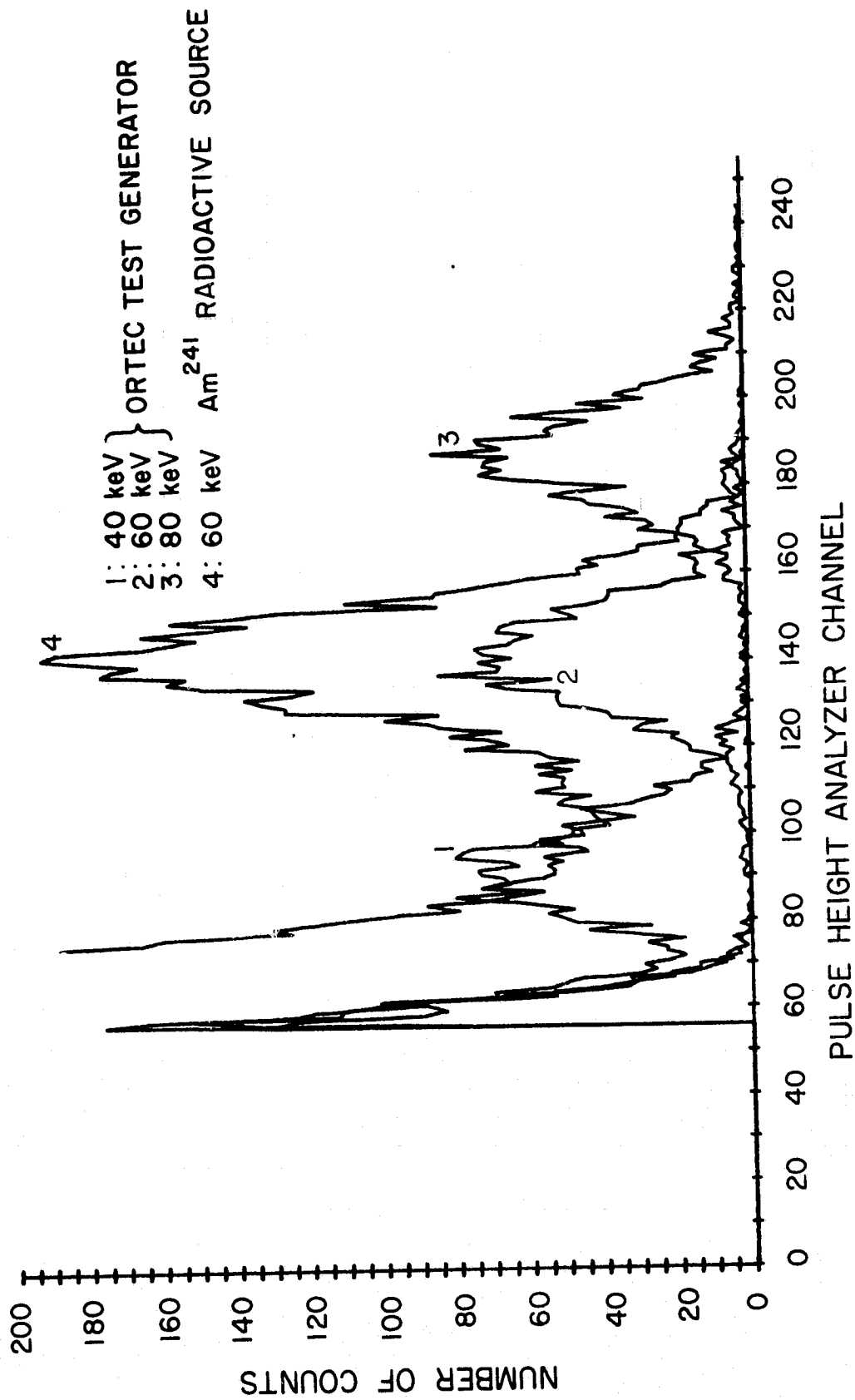
Figure 3.17 EPS intercalibration data for rocket 14.542 detector 1 down (40 μg cm^{-2} Au).
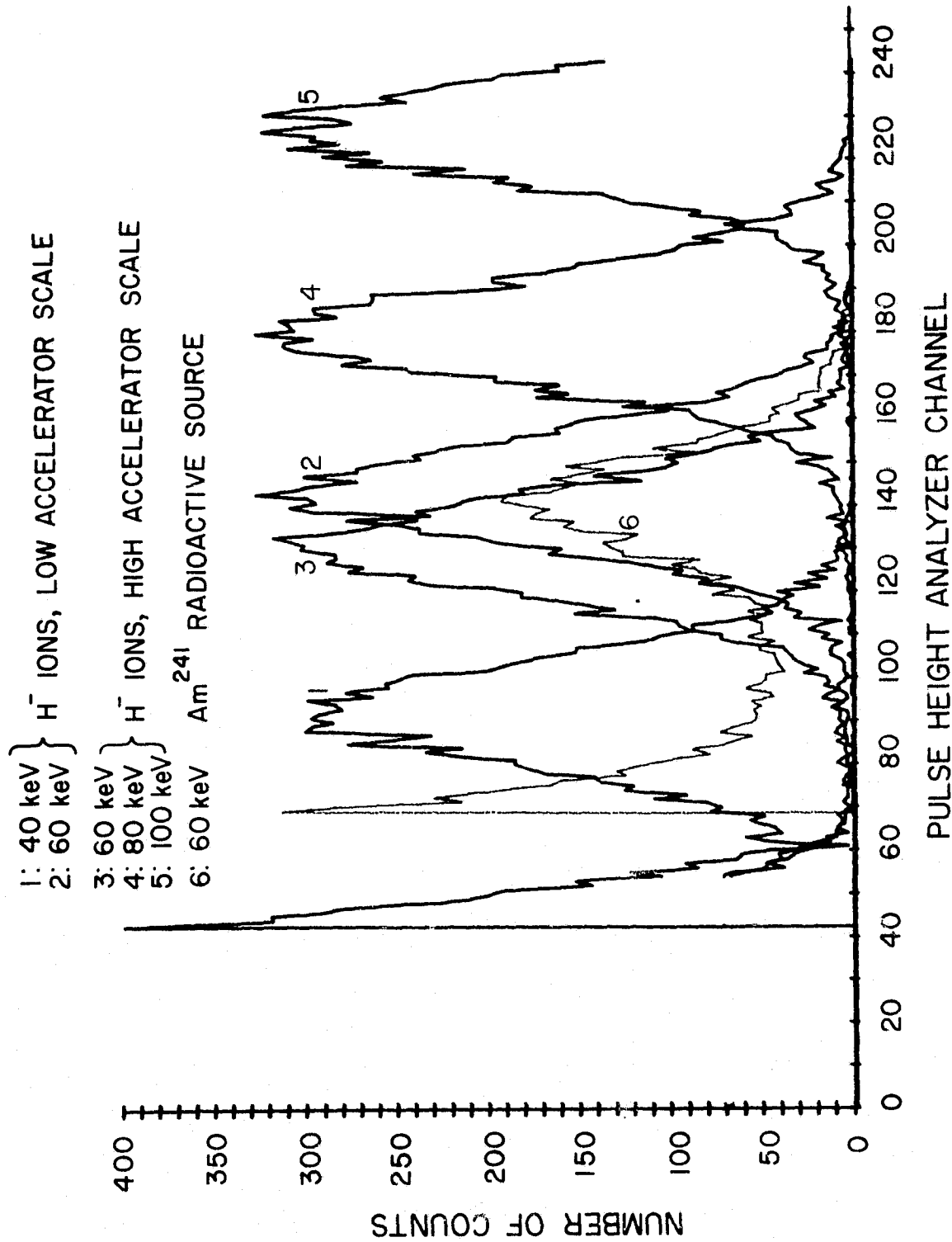
Figure 3.18 EPS intercalibration data for rocket 14.542 detector 1 down (40 μg cm^{-2} Au).

1: 40 keV ⎫
2: 60 keV ⎬ H⁻ IONS, LOW ACCELERATOR SCALE

3: 60 keV ⎫
4: 80 keV ⎬ H⁻ IONS, HIGH ACCELERATOR SCALE
5: 100 keV ⎭

6: 60 keV Am²⁴¹ RADIOACTIVE SOURCE

PULSE HEIGHT ANALYZER CHANNEL

NUMBER OF COUNTS
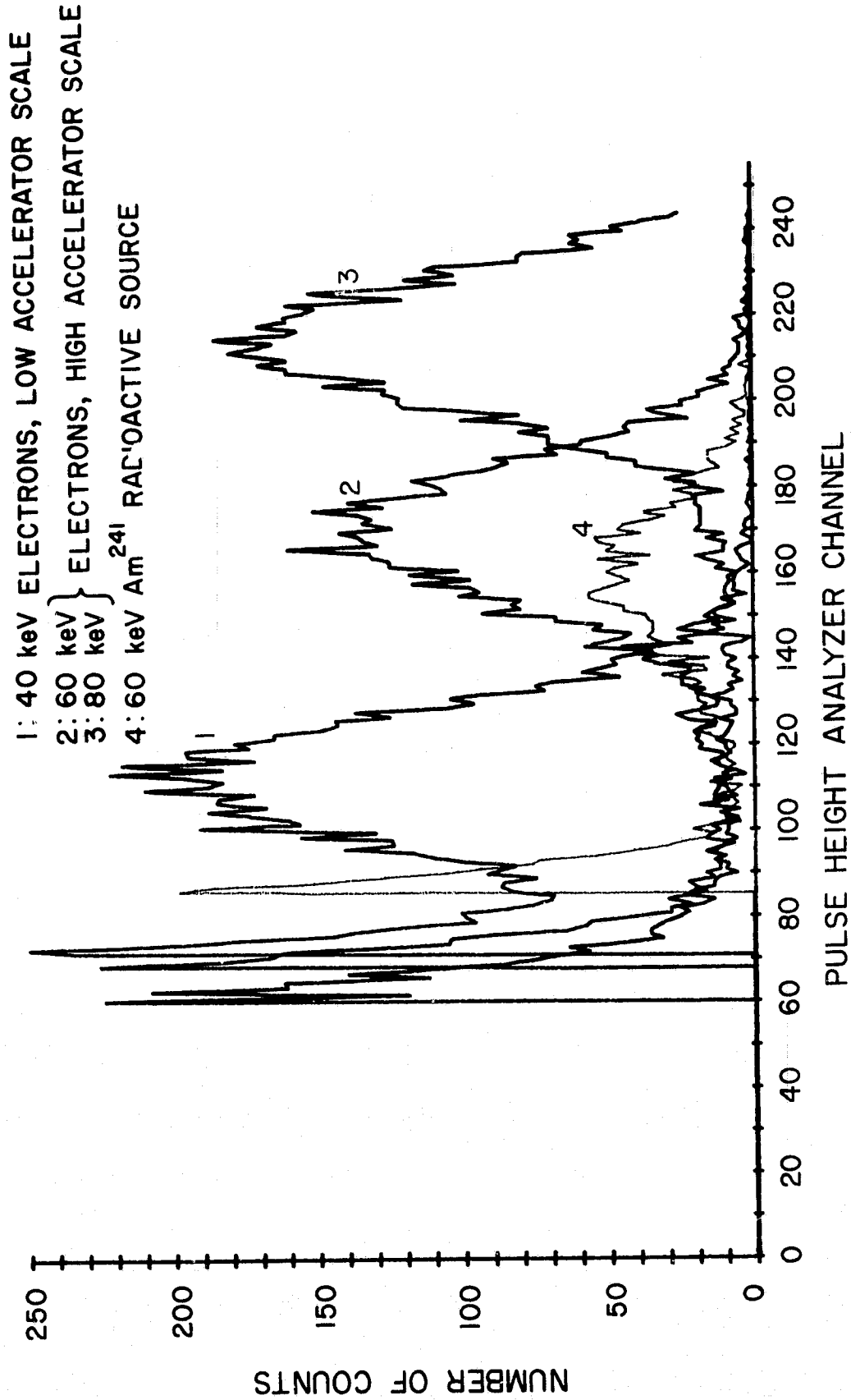
Figure 3.19   EPS intercalibration data for rocket 14.542 detector
2 up (100 μg cm^{-2} Al).

1: 90 keV ⎫
2: 100 keV ⎭ H⁻ IONS, HIGH ACCELERATOR SCALE

2

1

NUMBER OF COUNTS

PULSE HEIGHT ANALYZER CHANNEL
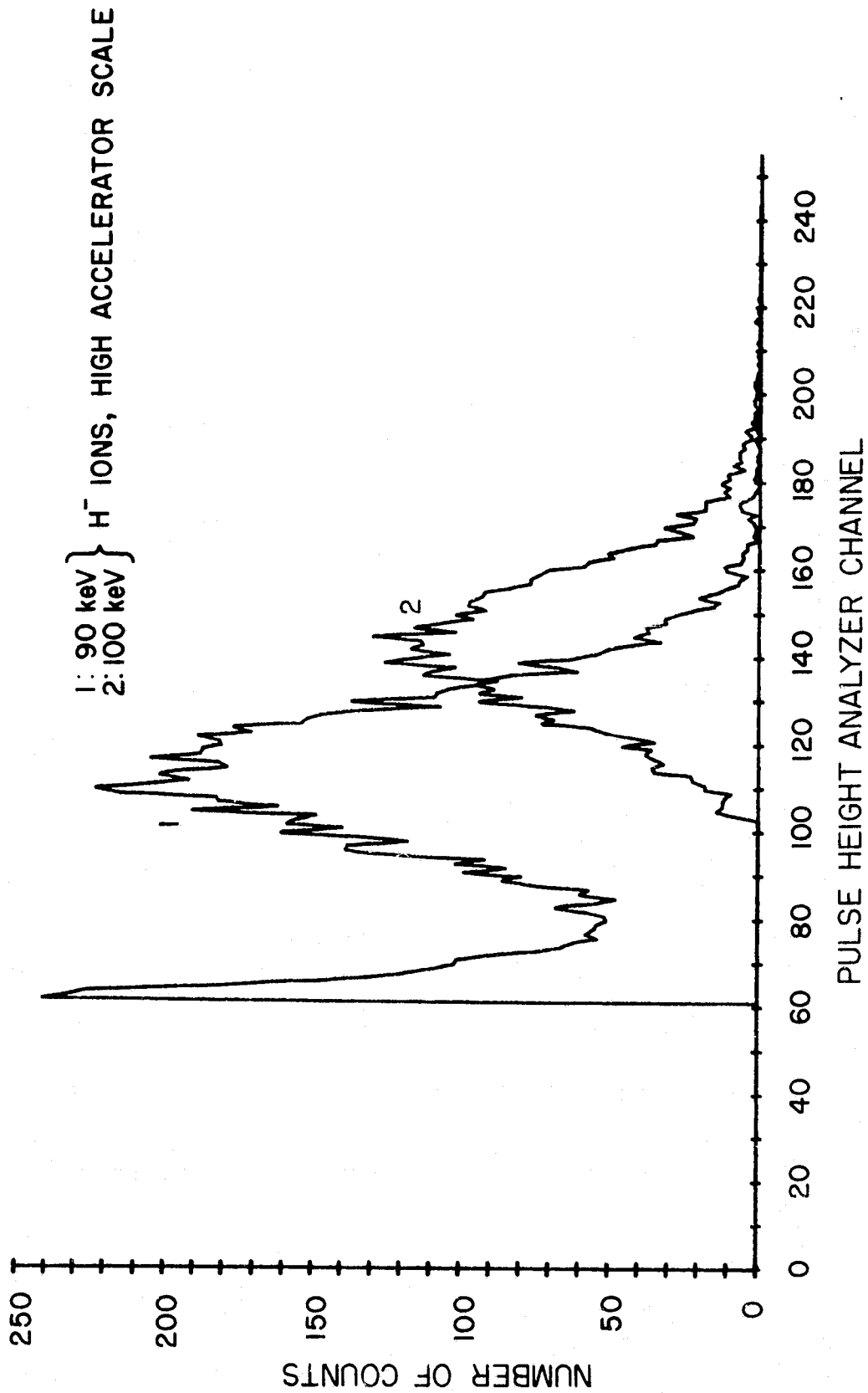
Figure 3.20 EPS intercalibration data for rocket 14.542 detector
2 up (100 μg cm⁻² Al).

energy by a constant. Since the number of channels between the 60 keV peaks for the high and low accelerator scales and the Am^{241} peak can be obtained from the graph, and the energy per channel is known, the accelerator instruments can be found. In this case we find that the high accelerator scale reads 1.3 keV higher than the actual particle energy, and the low accelerator scale reads 3.67 keV lower than the actual particle energy. It has been assumed that the H^- ions lose 2 keV in the 40 μg cm^{-2} Au detector dead zone. The Ortec test generator was used to prove peaks at 20 keV intervals, rather than using the H^- peaks since the loss in the dead layer varies with particle energy.

Figure 3.19 is used to calibrate the PHA for detector 2 up. Because different electronics are used, the channel corresponding to 60 keV and the energy per channel will differ from the previous measurements. Here we use the Am^{241} radioactive source to find the 60 keV channel, and the 60 keV and 80 keV peaks to determine the energy per channel. There is virtually no loss of energy for electrons in the dead zone, so in this case we can use this information. We have now calibrated the PHA channel numbers in terms of energy.

The information in Figure 3.20 will be treated as experimental data obtained from measurements of an unknown particle. From our calibration of the accelerator we know that the two peaks actually correspond to 88.7 keV and 98.7 keV H^- ions. From the calibration of the PHA for detector 2 up we find that these two peaks correspond to 40.5 keV and 53.6 keV particles (scale calibrated with electrons) for the 100 μg cm^{-2} Al detector. The same unknown particles were measured with a 40 μg cm^{-2} Au detector, Figure 3.18, and found to be around 90 and 100 keV (actually, the 90 keV energy was not measured for detector 1 down). Since the curves in Figure 3.21 were drawn with energy corresponding to the actual particle energy rather than the energy measured on a 40 μg cm^{-2} Au detector, we will use the actual particle energies when determining the ratio of measured energies between the detectors; the curves could be re-calculated so that the energy scale does correspond to the energy measured with a 40 μg cm^{-2} detector.*

---

*For electrons and gamma rays the difference effects of the dead zone are negligible. But for heavier particles the energy measured by a 40 μg cm^{-2} Au detector and the actual energy will differ slightly (a few of keV) because of losses in the dead zone.
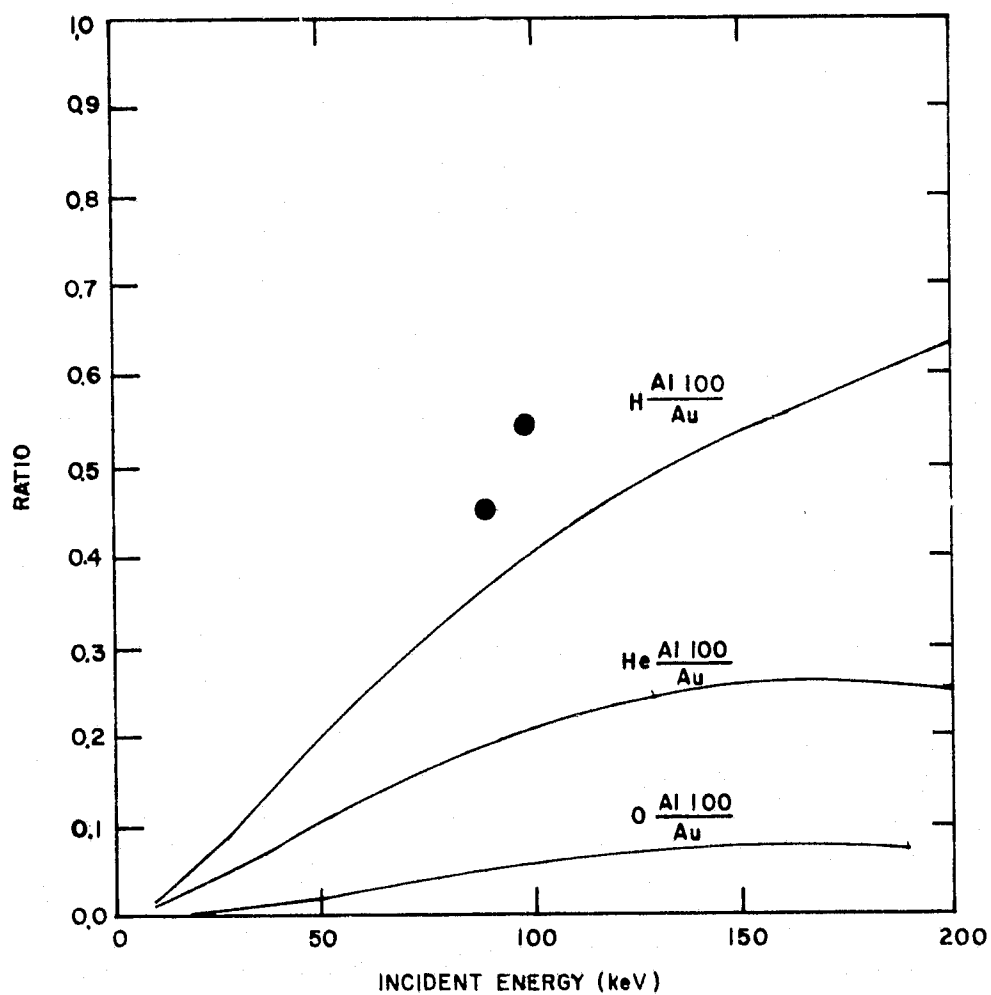
Figure 3.21　Ratios of fluxes recorded by 100 µg cm^{-2} aluminum detectors to those recorded by 40 µg cm^{-2} gold detectors. For electrons the ratio is unity (no attenuation). Two experimental measurements are recorded for energetic hydrogen particles.

For the 88.7 keV particle we have a ratio of Al-100/Au-40 of 0.45, the 98.7 keV ratio is 0.54. These two points are plotted on the graph in Figure 3.21; this figure contains the appropriate curves from Figure 3.16. We see that the experimental data fall near the curve corresponding to hydrogen; the unknown energetic particles have been correctly identified. The slight discrepancy between the experimental results and the theoretical prediction is being studied. It should be noted that drift in the accelerator voltage and the limited resolution of the voltmeter on the accelerator are responsible for some measurement errors.

This example has shown how several detectors can be used to identify the energetic particles. The procedure required to use the calibration data was outlined here in order to describe the process. When working with a calibrated instrument the particle energy (on a scale calibrated for electrons) would be obtained directly, and the ratio of measurements for various detectors could immediately be taken.

When several different types of energetic particles are present, the analysis becomes more involved. By using additional detectors (e.g., 40 μg cm^{-2} Al and a detector with a broom magnet) the various particles can be identified.

4. NOISE AND SIGNAL PROCESSING

4.1 *Introduction*

The energy resolution and the minimum measurable energy of the energetic particle spectrometers are limited by noise generated within the instruments. In the system described here the effect of noise is minimized in two ways. First, by considering the ultimate sources of noise in the system, the generated noise can be made as small as possible. Second, the signal can be processed by filtering (i.e., pulse-shaping) to give further reduction in the effect of noise.

The important sources of noise are the detector and the first stage of amplification. The different types of noise, their sources, and techniques used to maximize system performance will be discussed in this chapter. The implementation of noise reduction in electronic circuitry will be presented in the next chapter.

One can derive mathematically the linear filtering system that will provide the optimum performance in the presence of noise. Unfortunately the problem is complicated: in addition to a high signal-to-noise ratio we require causality, we desire relatively simple circuitry, and we must place some constraints on the output pulse shape. The signal processing circuit (the filter) is followed by a pulse-height analyzer which presents limitations regarding the input signal rise time and the duration of the pulse peak that it is to latch on to. Problems will also arise if another input occurs while there is still a non-zero output due to the previous input; this effect, called pile-up, is very important and will be discussed later. Voltages and currents derived from a random process are, in this text, understood to be rms values.

4.2 *Types of Noise*

4.2.1 *Thermal noise.* Thermal noise (Johnson noise) is caused by the random thermal motions of charge carriers within a conductor: a change in direction of travel corresponds to a change in the velocity component in the direction of current flow. This is a white noise process, that is, the power spectral density of the noise is constant over all frequencies. Actually, the power spectral density decays at a very high frequency (as one would expect, since a white process would possess infinite energy). Such approximations are typical, and allow straightforward analysis without

detracting from the usefulness of the solution. The spectral density of the square of the voltage is found to be*

$$S_{v^2} = 2kTR \qquad (4.1)$$

where k is Boltzmann's constant 1.38×10^{28} J/°K; T is the temperature of the conductor; and R is the resistance of the conductor.

Any material resistance that is a property of bulk material is a source of thermal noise. For example: eddy current losses in an inductor will contribute to thermal noise, but the radiation resistance (not the loss resistance) of an antenna will not introduce thermal noise. The resistors used in constructing a circuit and the distributed resistance within a semiconductor (e.g., R_p and R_s in Figure 3.6) are thermal noise sources.

The effect of the noise generated by a given component in a circuit depends on its relation to the rest of the circuit. To determine the effects of a noisy resistance it can be replaced by a noiseless resistor and a voltage or current source, Figure 4.1. Conventional circuit analysis techniques can then be used to determine the noise component at any other part of the circuit. Since the noise powers from different noise sources are independent, they add; therefore, when summing noise voltages it is often easier to work with mean square values (e.g., $v_t^2 = v_1^2 + \ldots + v_n^2$) The main point here is that associated circuit components affect the noise levels; the shunt capacitance in the detector, C_p (Figure 3.6) is large enough to reduce the contribution of the thermal noise of R_p to the level of secondary effect. Similarly, R_s and C_s are small enough to be negligible and the primary factor determining noise will be C_p and I_L (these are not thermal effects and will be discussed later).

---

*The rms noise voltage for band-limited thermal noise is $v_{rms} = \sqrt{4kTRB} = \sigma$ where B is the bandwidth and σ is the standard deviation. Since we are dealing with a zero mean process

$\sigma^2 = R(0)$, the auto-correlation function at $\tau = 0$.

$R(\tau) = \frac{1}{2\pi} \int_{-\infty}^{\infty} S(\omega) \, e^{j\omega\tau} \, d\omega$, evaluating at $\tau \geq 0$.

$v^2_{rms} = \int_{-\infty}^{\infty} S(2\pi f) df = 2 \int_{f_1}^{f_2} 2kTR \, df = 4kTRB.$
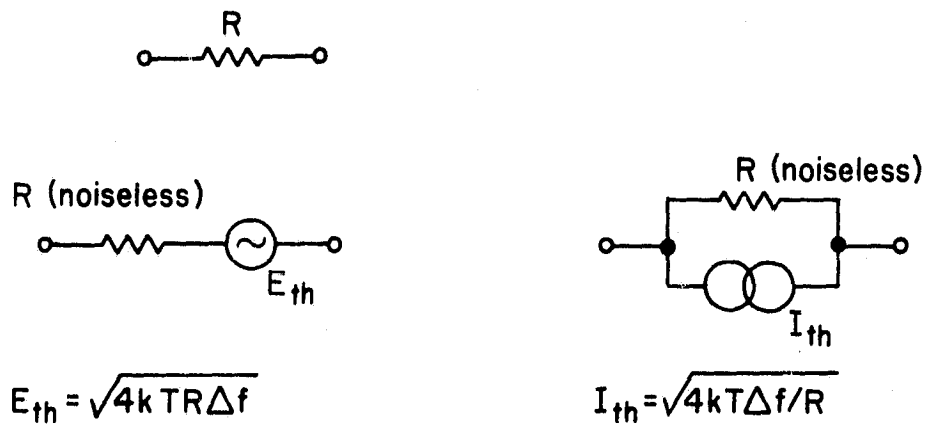
Figure 4.1 Representation of a noisy resistance by a noiseless
resistor with a noise source. Special symbols are
used for noise sources in order to distinguish them
from conventional sources. The voltage and current
levels indicated are rms values.

4.2.2 *Shot noise*. Shot noise results from fluctuations in the number of charge carriers, as compared with fluctuations in the velocity of the carriers which produces thermal noise. Shot noise is associated with tubes, transistors, and diodes.

In particular, consider a reverse-biased junction, as in a solid-state detector. In this case the effects of trapping and recombination are usually negligible and the charge carriers are assumed to be generated independently. The noise is essentially shot noise, given by

$$S_{i2} = I_1 e \tag{4.2}$$

where I_1 is the reverse leakage current and e is the electronic charge. The form of equation (4.2) is typical of the spectral density of the square of the current for shot noise. We see that shot noise is a white noise process.

4.2.3 *Flicker noise*. Flicker noise is a noise source observed in tubes, transistors, diodes, thin films and other components. The magnitude of the noise component is variable between different samples of the same device. The origin of flicker noise has not been completely explained; however, improved surface treatment in the manufacturing of devices has reduced the noise. The power spectrum of flicker noise approximates a $1/f$ characteristic.

4.2.4 *Excess noise*. Excess noise is a term often applied to the noise present in resistors. When a direct current is applied, this noise is observed in addition to thermal noise. This noise is most pronounced in carbon-composition resistors. Wire-wound resistors and metal-film resistors have less excess noise. Also, the use of a higher power resistor (e.g., 1/2 or 1/4 W instead of 1/8 W) results in less excess noise [*Allen Bradley*, personal communication]. In order to reduce excess noise, metal-film resistors should be used in critical parts of a circuit. Excess noise has a power spectral density that varies as $1/f$.

4.2.5 *Practical considerations*. During the discussion of the four types of noise some of the consequences of noise were mentioned; methods of reducing this noise at the source will now be considered.

Two methods of reducing thermal noise are available; one is to lower the temperature of the noise sources, the other is to reduce the bandwidth of the system. System bandwidth is determined by the filtering used and

will be discussed later. Lowering the temperature actually produces additional benefits. For the detector and the first transistor (FET) it will reduce the leakage currents, thereby reducing the shot noise. Unfortunately, at least in the case of thermal noise, the temperature must be lowered substantially in order to obtain a significant improvement in noise performance. If a device is normally operated at a room temperature of 20°C (293°K), the thermal noise power would only be reduced by a factor of two by cooling the device to -126°C (146°K).

Careful selection of components will also result in improved noise performance. Low-noise transistors approach ideal components; sorting a batch of low-noise parts would be advantageous, though it would be expensive. The noise performance of transistors is dependent on the source resistance, collector or drain currents and frequency of operation [*Motchenbacher and Fitchen,* 1973]; the circuit design should reflect this. The use of metal-film resistors to reduce excess noise has been noted. Quality capacitors and inductors have low resistive components and contribute less noise than lower quality components (e.g., mylar capacitors and NPO ceramic versus bypass ceramic capacitors).

Although interference and unwanted feedback are not noise in the sense used above, careful shielding, de-coupling, and attention to ground loops will result in improved performance.

4.3 *Signal Processing*

There are several different approaches to analyzing the effects of noise on a system's performance; the development that follows will parallel the analysis presented by *Nicholson* [1974]. Alternative treatments have been given by *Motchenbacher and Fitchen* [1973] and *Goulding* [1972].

After describing the figures of merit that will be used for evaluating various filtering (pulse-shaping) schemes, the optimal filter will be derived and practical filters will be discussed. The results derived will differ from Nicholson's by a constant which is due to differences in the definition of power (actually: voltage squared) spectral density, and in the Fourier-transform relationship between power spectral density, S_x, and the auto-correlation function, R_x. For general discussions of stochastic processes and communications theory see *Papoulis* [1965] and *Taub and Schilling* [1971], respectively.

4.3.1 *System resolution.* The various noise mechanisms outlined in Section 4.2 will here be treated as zero-mean stationary random processes with Gaussian distributions. The noise sources will be considered as independent additive random processes.

Consider the system shown in Figure 4.2; a signal pulse and additive noise are illustrated. The relative probability density shown in Figure 4.2 is analogous to the information obtained from a pulse-height analyzer. The noise affects the level of the pulse at the output of the system. If several pulses of amplitude α were measured at v_o and plotted as the number of occurrences of a given voltage as a function of the voltage, the plot would look similar to the relative probability distribution shown for $v_o(t_o)$. Since the amplitude of the noise is usually small, noise measurements will be clustered around α; however, there will be infrequent noise pulses of large magnitude causing $v_o(t_o)$ to be quite different from α, possibly even negative.

The peak of the relative probability density becomes wider when more noise is present. This phenomenon is of particular significance in the measurement of energetic particles. It is often desired to measure two energy levels that are almost the same. The spreading effect of the noise will cause the two pulses to overlap.

A figure of merit describing the resolution of the system is the full width at half maximum (FWHM). The FWHM is defined as the width of the interval (centered at the mean) where the relative probability fails to halve its maximum value, as indicated in Figure 4.2.

For a Gaussian distribution, the probability density is given by

$$P_{v_o}(v) = \frac{1}{\sqrt{2\pi\,\sigma^2}}\, e^{-(v-v_o)^2/2\sigma^2} \tag{4.3}$$

To find the two voltages that occur with probability 1/2, let

$$P_{v_o}(v) = (1/2)\, P_{v_o}(v_o) = 1/2\,\frac{1}{\sqrt{2\pi\,\sigma^2}}$$

so that

$$v = v_o \pm \sigma\,(2\ln 2)^{1/2} = v_o \pm (1/2)v_{\text{fwhm}} \tag{4.4}$$
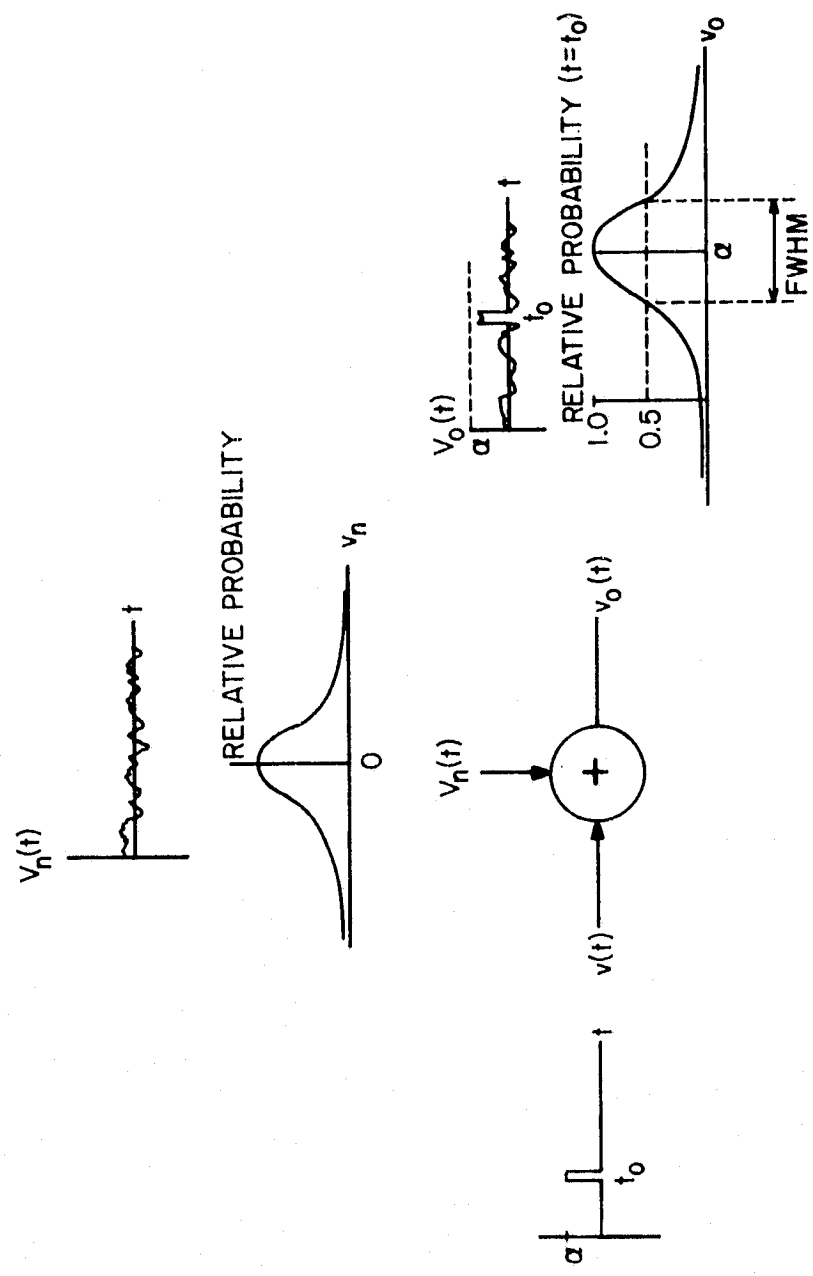
Figure 4.2 A signal in the presence of additive noise. The time domain and probability density function (normalized scale) for random processes are shown.

The standard deviation, σ, is the rms noise voltage, v_n. The general result for a Gaussian process is

$$v_{fwhm} = 2(2 \ln 2)^{1/2} v_n = 2.36 v_n \tag{4.5}$$

If the energy level corresponding to the voltage v_{fwhm} is known, the FWHM can be quoted in terms of electron volts (eV).

The rms noise voltage can be measured in the laboratory, but some precautions must be taken. Many ac voltmeters are averaging meters with scales calibrated such that the meter will indicate the rms value of a sinusoidal input. Since noise is not sinusoidal, a different correction factor must be used. For Gaussian noise the average value is 0.798 of the rms value (it is 0.636 for a sine wave). To obtain the correct value from an average-responding meter, the reading must be multiplied by 1.11.

Another problem results from the random nature of noise. Most averaging meters limit the peak signal. This can result in an erroneous noise measurement. The crest or peak factor of a signal is defined as the ratio of the peak value to the rms value of the wave form. A peak value cannot be assigned to a noise signal. The crest factor for Gaussian noise is greater than 3 about 1% of the time, and is greater than 4 less than 0.01% of the time. As a protection mechanism many averaging meters saturate on over-range readings corresponding to a crest factor in the range of 1.4 to 2. For accurate readings an instrument with a high crest factor must be used. Alternatively readings may be taken below half scale as this effectively doubles the crest factor. Whenever possible a true rms meter should be used for these measurements.

4.3.2 *Equivalent noise charge*. For many systems a signal-to-noise ratio is used as a figure of merit. As discussed in the Section 4.3.1, the figure of merit should give an indication of the resolution of the system as well as describing the minimum detectable signal. The FWHM is a useful specification, but it is not convenient for analysis. Accordingly, we will now define a figure of merit that specifies the output noise level (after processing) in terms of the amount of charge required at the input of the system in order to obtain the same output level. This is termed the equivalent noise charge (ENC) which is related to other figures of merit: if a particle of energy E produces a charge Q on the detector and gives a voltage, V, at the output we can write

$$\frac{ENC}{Q} = \frac{v_n}{V} = \frac{v_{fwhm}/2.36}{V} = \frac{E_{fwhm}}{2.36} \tag{4.6}$$

For a silicon detector E/Q has a value of 3.5 eV per carrier (for germanium it is 2.9 eV):

$$E_{fwhm} = 5.30 \times 10^{19} \, ENC \tag{4.7}$$

4.3.3 *Preamplifier noise model.* In a well-designed preamplifier, the noise performance is usually determined by the quality of the first stage. It will be assumed here that all the significant noise sources of the system are present in the first stage; the remaining stages provide additional amplification and filtering but no additional noise.

The noise model of the preamplifier is given in Figure 4.3. For reasons to be discussed in the next chapter, the preamplifier is a charge amplifier rather than a voltage amplifier. Detector, transistor [FET], and circuit shunt capacitances are collected in C_t; similarly the shunt resistances are combined as R_t. The feedback network consists of a capacitor and a resistor. The transistor noise sources have been reflected to the input. The "power" spectral densities are actually squared-voltage or squared-current spectral densities; they will both be referred to as power spectral densities, using subscripts to distinguish the two. The noise sources in the model are identified as follows:

(a) $S_{v_1}2 = \frac{2}{3}\left(\frac{2kT}{g_m}\right)$

Noise arising from majority carriers in the channel; allows modeling as a Johnson noise source across source drain. Reflected to the input.

(b) $S_{v_f}2 = \frac{A_f}{2f}$

The flicker noise of the FET. The constant A_f is determined experimentally.

(c) $S_{i_2}2 = \frac{kT\omega^2 C_{gs}^2}{2g_m}$

Fluctuations in the channel currents are coupled through the gate source capacitance and are modeled by i_2^2.

(d) $S_{i_3}2 = I_g e$

Shot noise arising from the gate leakage current, I_g. (A reversed biased junction).
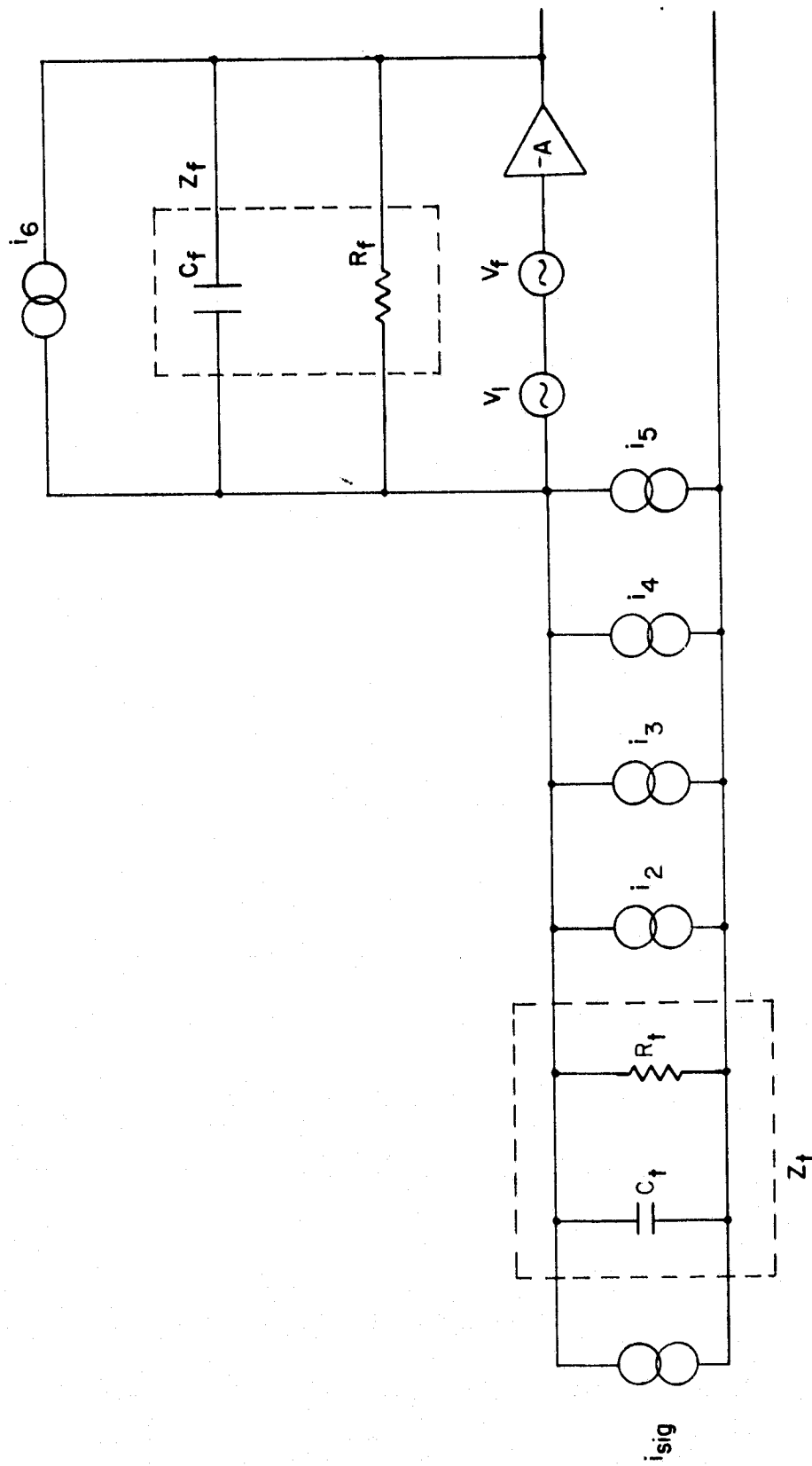
Figure 4.3 Noise model for the preamplifier. The individual sources are identified in the text.

(e) $S_{i_4}2 = I_1 e$ Shot noise arising from the detectors reverse leakage current.

(f) $S_{i_5}2 = \dfrac{2kT}{R_t}$ Johnson noise of the shunt resistances, modeled by R_t.

(g) $S_{i_6}2 = \dfrac{2kT}{R_f}$ Johnson noise of the feedback resistor, R_f.

The noise sources in the model are identified as follows: assuming that A is much greater than 1, that Z_f is much greater than Z_t, and that the amplifier has a relatively low output impedance (i.e., it is not loaded by Z_f), the model can be reduced to the circuit of Figure 4.4. In Chapter 5 these assumptions will be shown to be valid, in addition, Z_f and Z_t will be shown to be capacitative. By taking $Z_t = 1/(2\pi f C_t)$ and $Z_f = 1/(2\pi f C_f)$ we find the Thevenin equivalent circuit given in Figure 4.5 (which eliminates i_{sig} and just considers noise). Referencing the noise to the input has resulted in a power spectral density that has components that remain constant with frequency (called A noise), vary as $1/\omega^2$ (the B noise), and vary as $1/\omega$ (the C noise). Notice that the A-noise component is due to variations in the channel current, the B noise is due to thermal and leakage effects, and the C noise is the flicker noise component.

4.3.4 *The optimal filter.* The optimal filter for the system is determined, in principle, by applying the techniques used in analyzing communication systems. It can be shown that, in general, the optimal linear filter will have an impulse response that is the mirror image of the signal at the input of the system when dealing with white noise. If the noise is not white, the signal and noise can be processed by a pre-whitening filter that produces white noise at its output; the optimal filter is then designed using the modified signal pulse shape.

It will be assumed that the flicker noise (C noise) makes a negligible contribution to the input noise. By selecting transistors with low flicker noise this approximation becomes reasonable. We then have the noise spectral density (see Figure 4.5)

$$S_{v_{eff}} = a^2 + b^2/\omega^2 = a^2(1 + \omega_c^2/\omega^2) \tag{4.8}$$
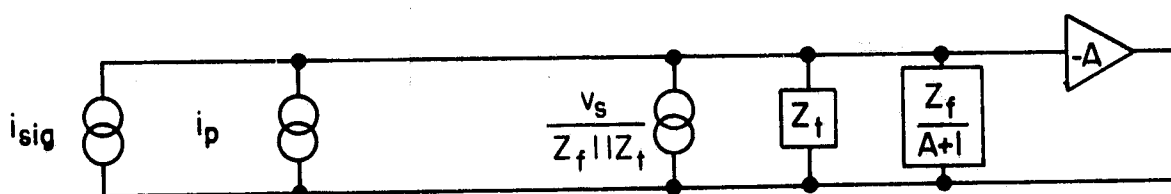
$$\overline{v_s^2} = \overline{v_1^2} + \overline{v_f^2}$$

$$S_{v_s}^2 = \frac{2}{3}\frac{2kT}{gm} + \frac{A_f}{2_f}$$

$$\overline{i_p^2} = \sum_{k=2}^{6} \overline{i_k^2}$$

$$S_{i_p}^2 = e(I_g + I_1) + 2kT\left(\frac{1}{R_t} + \frac{1}{R_f}\right) + \frac{kT\omega^2 C_{g_s}^2}{2gm}$$

Figure 4.4   Equivalent noise model of the preamp.
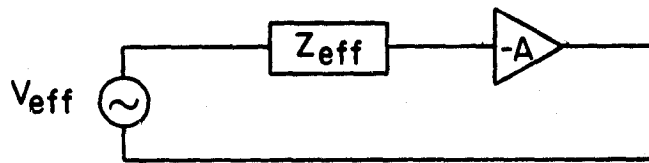
$$S_{v^2_{\mathbf{eff}}} = (a^2 + \frac{b^2}{\omega^2} + \frac{c^2}{\omega})$$

where

$$a^2 = \frac{kT \, C_{g_s}^2}{2gm \, C_t^2} + \frac{4}{3} \frac{kT}{gm} \frac{(C_f + C_t)^2}{C_f^2}$$

$$b^2 = \frac{(I_g + I_1)e}{C_t^2} + \frac{2kT \, (R_t + R_f)}{R_t \, R_f \, C_t^2}$$

$$c^2 = \pi \frac{A_f}{C_t^2} [C_f + C_t]^2$$

Figure 4.5   Thevenin equivalent noise model.

where $\omega_c (= b/a)$ is called the noise corner frequency, i.e., the frequency at which the A-noise component is equal in magnitude to the B-noise component. The noise corner time, τ_c, is $1/\omega_c$. The pre-whitening filter and the modified signals are shown in Figure 4.6. The input is modeled as a step function because a charge pulse across the input capacitance will produce a voltage step (Z_{eff} is capacitive, denoted C_{eff}). The output of the pre-whitening filter can be found using Laplace transform techniques. The noise power spectral density is modified according to

$$S_{out} = |H(j\omega)|^2 S_{in} \tag{4.9}$$

as developed in texts on stochastic processes.

The impulse response of the optimal filter, which follows the pre-whitening filter, is shown in Figure 4.7. The impulse response of the optimal filter is the mirror image of the signal at the output of the pre-whitening filter. The signal pulse at the output of the optimal filter is cusp shaped, as shown in Figure 4.8. Since the optimal filter is non-causal, it is not of practical use; however, by comparing the noise performance of realizable filters with that of the optimal filter we can determine if attempts to improve performance are justified.

Since the noise has zero mean (the mean is still zero after filtering), the auto-correlation function, $R_{v_{no}}(\tau)$, evaluated at $\tau = 0$ is the variance of this process, $\sigma^2_{v_{no}}$. Therefore, the rms noise voltage at the output of the optimal filter is given by

$$v_{no} = \sigma_{v_{no}} = \sqrt{R_{v_{no}}(0)} = \left[\frac{1}{2\pi} \int_{-\infty}^{\infty} S_{v_{no}}(\omega)\,d\omega \right]^{1/2}$$

$$v_{no} = a\sqrt{\tau_c/2} \tag{4.10}$$

Then from equation (4.6)

$$ENC = \frac{Q v_{no}}{V} = C_{eff}\sqrt{2ab} \tag{4.11}$$

This is the equivalent noise charge for the optimal filter, which has a cusp-shaped output signal pulse.

The optimal linear filter was derived; it has been shown [Bertolaccini et al., 1966] that this is also the optimal pulse shape for non-linear, time variant systems.

$v_{sig} = Q/C_{eff}\, u(t)$

$v_w = Q/C_{eff}\, e^{-t/\tau_c} u(t)$

v_{sig}

IN $\quad H_w(j\omega) = \dfrac{1}{1 + \omega_c/j\omega}$ OUT

v_w

$S_{vn} = a^2(1 + \omega^2/\omega^2)$

$S_{vn_w} = a^2$
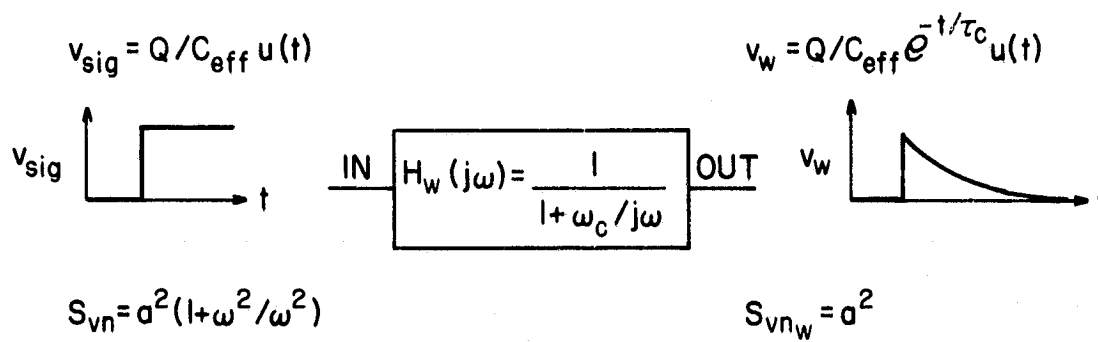
Figure 4.6 The pre-whitening filter.

$$h_0(t) = e^{t/\tau_c} u(-t)$$

$$H_0(j\omega) = \frac{1}{\omega_c - j\omega}$$
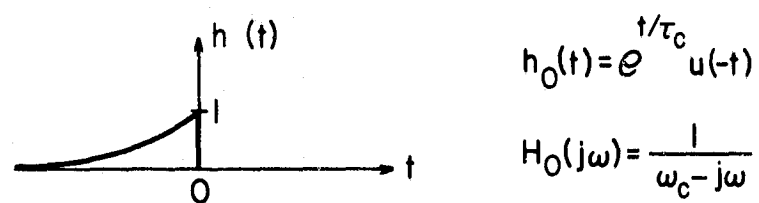
Figure 4.7   Optimal filter parameters.

$$v_w = Q/C_{eff}\, e^{-t/\tau_c}\, u(t)$$

$$v_O = Q\tau_c/2C_i\, e^{-|t|/\tau_c}$$

$$H_O(j\omega) = \frac{1}{\omega_c - j\omega}$$

$$S_{vn_w} = a^2$$

$$S_{vnO} = \frac{a^2}{\omega^2 + \omega_c^2}$$
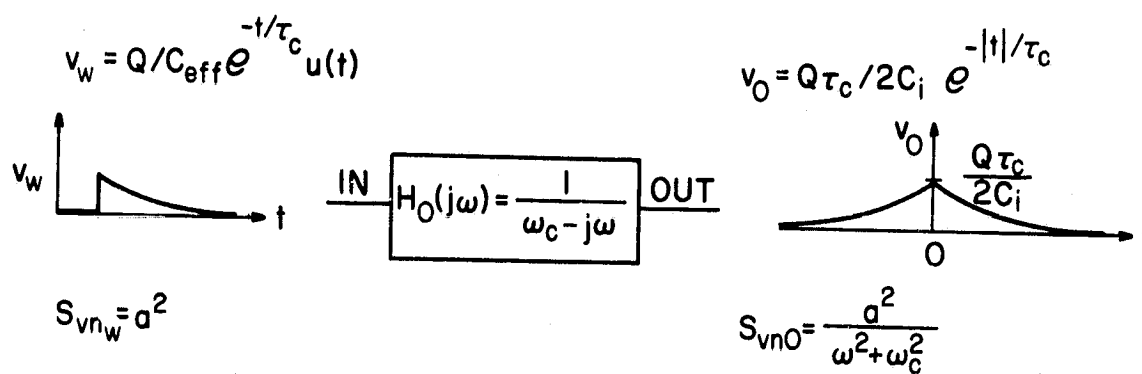
Figure 4.8   The optimal filter.

4.3.5 *Non-optimal filters.* Theoretically, the performance of any linear filter can be calculated using the methods outlined above. Difficulties occur in evaluating the integral in equation (4.10).

It has been shown [*Bertolaccini et al.*, 1969] that the optimum pulse shape with the added restraint of finite duration is also cusp-shaped. A triangular pulse is often considered as an approximation to the finite cusp. The sharp peak of the cusp or the triangle is undesirable for use in pulse-height detection, and not often used.

The CR-RC filter is of particular interest. *Nicholson* [1974], has shown that

$$v_n^2 = \frac{a^2}{2\lambda(\lambda+1)\tau_1} + \frac{b^2\tau_1}{2(\lambda+1)} + \frac{c^2}{\lambda^2-1}\frac{\ln(\lambda)}{\pi}$$ (4.12)

where

$\lambda = \tau_2/\tau_1$
τ_1 = high-pass filter time constant
τ_2 = low-pass filter time constant

The output signal pulse has a maximum value of

$$v_{max} = \frac{Q}{C_i} \lambda^{\lambda/(1-\lambda)}$$ (4.13)

and the equivalent noise charge is given by

$$ENC = e\, C_{eff} \left(\frac{a^2}{4\tau} + \frac{b^2\tau}{4} + \frac{c^2}{2} \right)^{1/2}$$

where $\tau = \tau_1 = \tau_2$; $\lambda = 1$ is the optimum case. Notice that τ does not affect the flicker noise component; the available trade-off occurs between the A noise and the B noise. The minimum *ENC* occurs for $\tau = \tau_c = a/b$.

The noise performance of several filter types is listed in Figure 4.9, together with the corresponding signal pulse shapes. The selection of the non-optimal filter that is to be used in the system deals with trade-offs in hardware and noise performance, therefore the selection will be saved for Chapter 5.
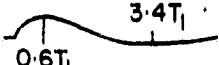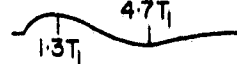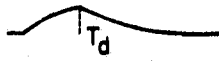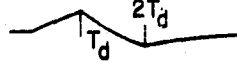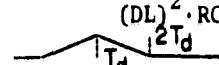
Filter	Conditions	Equivalent noise charge relative to the optimal filter.
To give a cusp-shaped pulse	Rise and fall time constants $= \frac{a}{b}$ Time to peak $= \frac{2a}{b}$	1.0
CR·RC T_1	$T_1 = T_2 = \frac{a}{b}$	1.36
C R·(RC)^2 $2T_1$	$T_1 = T_2 = \frac{1}{\sqrt{3}}\frac{a}{b}$	1.215
CR·(RC^4) $4T_1$ Semi-Gaussian (for a true Gaussian ENC relative $= 1.120$)	$T_1 = T_2 = \frac{1}{\sqrt{7}}\frac{a}{b}$	1.16
(CR)^2·RC $3\cdot4T_1$ $0\cdot6T_1$	$T_1 = T_2 = \sqrt{3}\,\frac{a}{b}$	1.43
(CR)^2·(RC)^2 $4\cdot7T_1$ $1\cdot3T_1$	$T_1 = T_2 = \frac{a}{b}$,	1.36
DL·RC T_d	$T_d = 1.036T_2$ $T_2 = 1.29\,\frac{a}{b}$	1.096
(DL)^2·RC T_d $2T_d$	$T_d = T_2$ $T_2 = 2.2\,\frac{a}{b}$	1.37
(DL)^2·RC T_d $2T_d$	$T_d = \sqrt{3}\,\frac{a}{b}$ (true integration)	1.075

Figure 4.9   Noise performance of various filters [from data compiled by *Herbst*, 1970].

5. LINEAR ELECTRONIC CIRCUITS

5.1 *Introduction*

The linear portion of the energetic particle spectrometer is described in this chapter. The principal elements are the preamplifier, the switching circuit, and the shaping filter. Problems and the resulting trade-offs are discussed and the actual circuits used on the JASPIC program are analyzed. Because of the limited development time, the circuits used are modified versions of those in the Nucleometrics, Inc., Model 101 charge-sensitive amplifier.

5.2 *The Charge Preamplifier*

5.2.1 *Function of the charge preamplifier.* The detector was described in detail in Chapter 3. The detector model was given in Figure 3.6. This model can be simplified by considering R_s, C_s, and Z as secondary effects; the detector impedance then becomes the parallel combination of R_p, C_p, and C_w. At the frequencies of interest the detector will be primarily capacitive and R_p can be omitted. It was noted that C_p is dependent upon the detector temperature and bias voltage.

The simplified detector model is presented in Figure 5.1 together with a voltage sensitive amplifier which is represented by an input impedance Z_{in} and a voltage gain A_v. A charge pulse from the detector will produce a voltage, v_{in}, across the effective input capacitance, C_{eff} (the combined effect of C_p, C_w, and Z_{in}) described by $v_{in} = Q_{in}/C_{eff}$. To evaluate the performance of this system, we must consider C_{eff}. A high resistive component for Z_{eff} is desired to prevent the effective input capacitance from being discharged during the measurement interval. This means that Z_{eff} is essentially capacitative, and $C_{eff} = C_p + C_w + C_{in}$, where C_{in} is the capacitative portion of Z_{in}. We see that for a voltage-sensitive configuration $v_{in} = Q_{in}/(C_p + C_w + C_{in})$. If C_{in} is made small to increase the signal level, the variations in C_p, the detector capacitance, will cause fluctuations in the gain of the preamplifier (gain is measured in terms of the output voltage produced by the quantity of charge corresponding to one electron volt at the input). Conversely, if C_{in} is made large in order to minimize the effect of the variations in C_p, the input signal level is substantially reduced.

It should be noted that very low-level signals are present at this point, and that signal level cannot be indiscriminately traded for gain
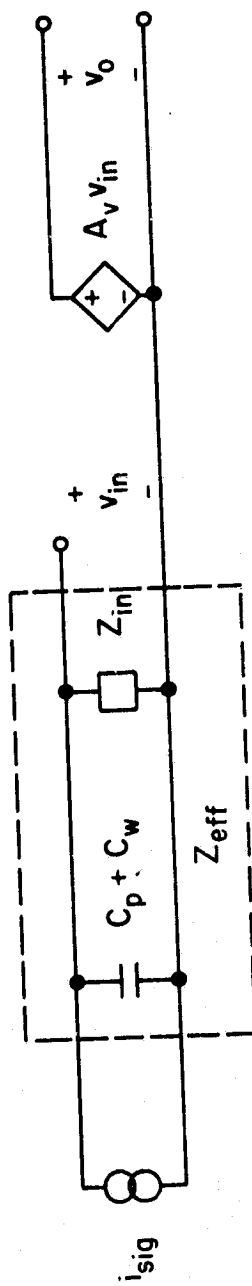
Figure 5.1   A voltage sensitive preamplifier.

stability. To create a carrier in the detector requires 3.5 eV of energy (for silicon). A 50 keV energetic particle will produce about 1.43×10^4 carriers. With each carrier providing 1.6×10^{-19} C of charge, only 2.3×10^{-15} C of charge is available from the detector*. This corresponds to an input signal of 2.3 mV/pF. Considering C_{eff} to be of the order of 250 pF we obtain 9 μV as the signal into the voltage-sensitive amplifier.

By using a charge-sensitive preamplifier it is possible to achieve good gain stability with a small loss in input sensitivity. Figure 5.2 shows (a) the general feedback amplifier, and (b) the charge-sensitive configuration, which is a special case. For the reasons cited when considering the voltage-sensitive amplifier we can neglect R_p and the resistive part of Z_{in}. In general, the feedback impedance, Z_f, can be reflected into the input and be combined with Z_{in}. If Z_f is resistive the voltage-sensitive configuration, discussed earlier, is obtained. If, however, Z_f is capacitive, as represented in Figure 5.2(b) the relations given below are obtained

$$Z_{in} = \frac{1}{\{jw[C_{in} + (1+A)C_f]\}} \tag{5.1}$$

$$C_{eff} = C_{in} + (1+A)C_f \tag{5.2}$$

$$v_o = \frac{-A_v Q_s}{(C_{in} + C_f) + A_v C_f} \tag{5.3}$$

If $A_v C_f \gg C_{in} + C_f$, then $v_o = Q_s/C_f$.

The effective input capacitance, C_{eff}, can be much larger than the detector capacitance if a high gain amplifier is available. This will have the effect of eliminating any effect of variation in the detector capacitance. Also, with a large gain, A_v, the output voltage is related to the input charge by $1/C_f$. By using a charge-sensitive configuration a large effective input capacitance has been obtained together with a stable gain relationship.

---

*For comparison purposes, a typical E_{fwhm} for the JASPIC EPS was 1.3 keV for the electronics alone, and 7.5 keV with a detector connected (the increased capacitance on the input increases the noise). Using the results of Chapter 4, this corresponds to an ENC of 2.5×10^{-17} C and 1.4×10^{-16} C, respectively.
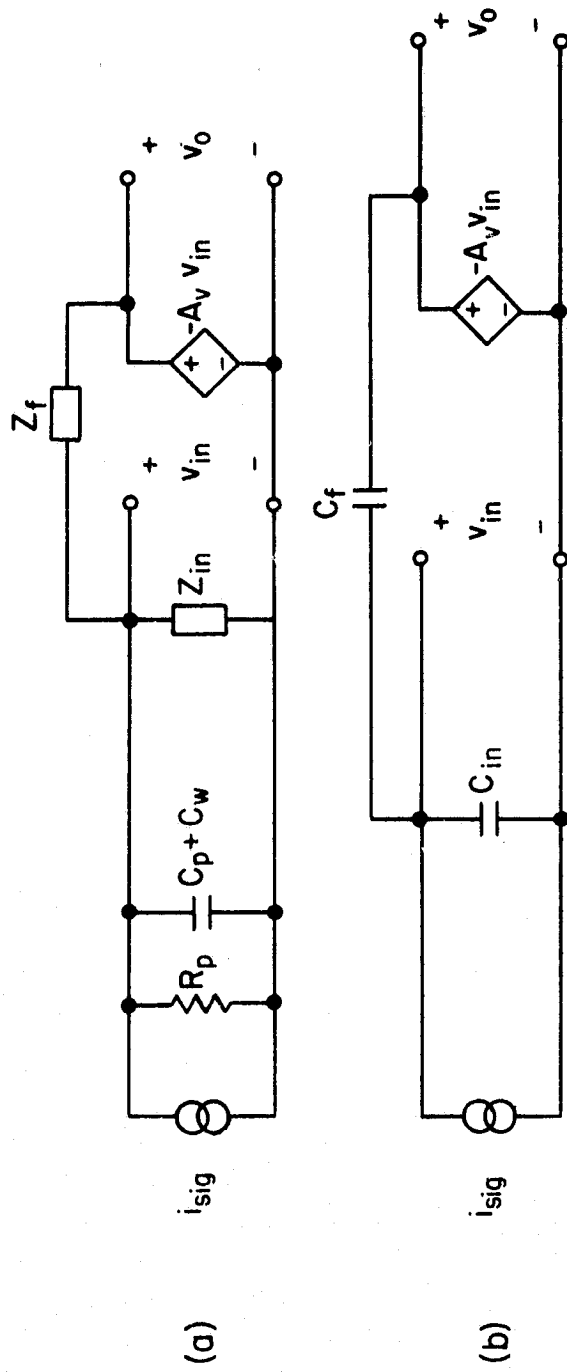
Figure 5.2 (a) A feed-back amplifier with simplified detector equivalent circuit. (b) The feed-back amplifier in the charge-sensitive configuration with the resistive components neglected, $C_{in} = C_p + C_w + C_{in}$ (C_{in} is the capacitive component of Z_{in}).

When the effective input capacitance is required for noise performance calculations, one determines the effective input capacitance without considering the effects of feedback. It is for this reason that $C_f + C_t$ appears in the equations of Figure 4.5 when the noise analysis is performed. Since C_f is usually quite small compared to C_t, there is little increase in noise.

It is clear from the above analysis that a charge-sensitive configuration is desirable. The preamplifier should have a high input impedance and high gain. An amplifier designed with these properties will match the assumptions made in Chapter 4 regarding noise performance, allowing a straightforward analysis of performance. The actual design of the charge preamplifier will be considered in the next section.

5.2.2 *Circuit description.* The charge preamplifier circuit is given in Figure 5.3; a photograph of the preamplifier is shown in Figure 5.4. The input transistor, a 2N6451 JFET, is designed for low-noise preamplifier applications. Because of its specialized nature the data sheet is reproduced in Table 5.1.

A functional description of the circuit follows. The JFET Q_2 is a common-source amplifier having a high input impedance that will not disturb the charge on the input capacitance. The load of Q_2 is a common-base amplifier Q_3; Q_2 and Q_3 together form a cascode amplifier. Transistor Q_1 acts as a constant-current source and provides bias current for Q_2 and Q_3. The output is taken from the emitter follower Q_4. Zener diode D_1 is included for biasing and diode D_2 is a field-effect current-regulator diode. D_2 provides a constant bias current and presents a very high ac impedance.

A detector-bias filter circuit is formed by C_1, C_2, R_1, and R_2. C_3 and R_3 are associated with the test input. Power supply decoupling is provided by R_9, R_{10}, C_4, and C_9. The dc supplies are filtered by feedthrough capacitors C_{11}, C_{12}, and C_{13}. Typical dc operating point voltages are included on the schematic.

The midband small signal model of the charge preamplifier is given in Figure 5.5. A voltage divider is formed by C_f and C_{in}; this is a voltage-feedback current-error configuration. The internal capacitances of the transistors, except for y_{is} of Q_2, are considered negligible. The various bypass capacitors are considered to be short circuits. The input impedance of Q_2 is primarily capacitive, and is included in C_{in} with C_3, detector
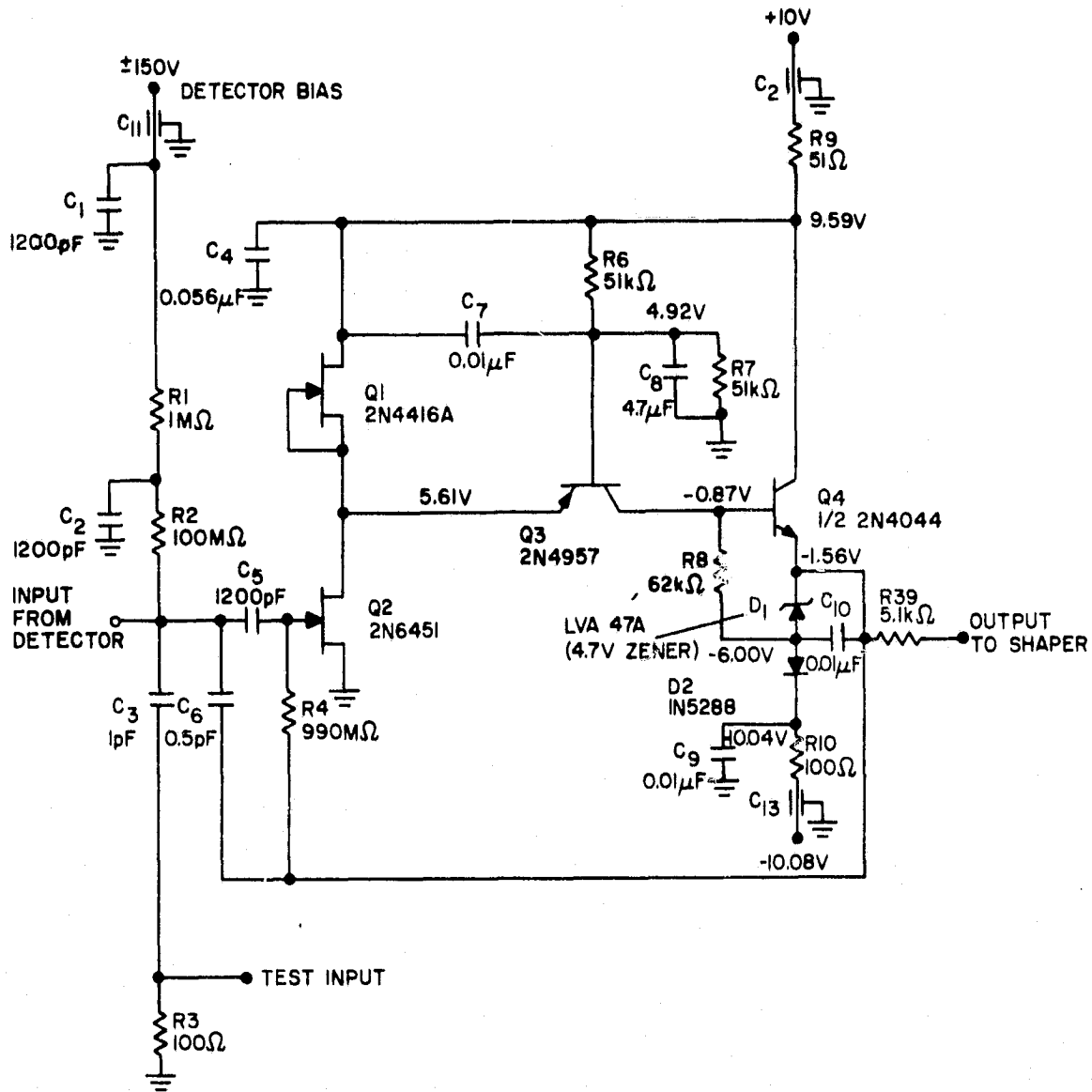
Figure 5.3 Schematic of charge preamplifier.
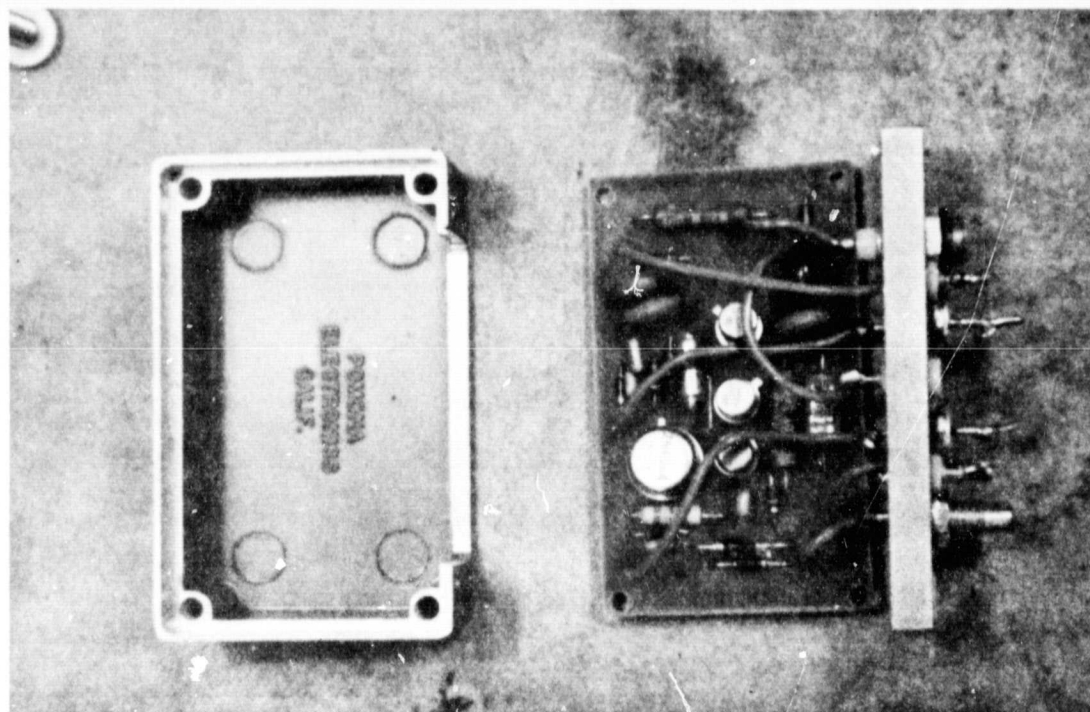
Figure 5.4   The charge preamplifier used in the JASPIC program.

Table 5.1

Specifications for Texas Instruments N-channel silicon junction Field-Effect Transistor types 2N6451 through 2N6454. Designed for low-noise preamplifier applications, especially hydrophones, IR sensors, and particle detectors.

*absolute maximum ratings at 25°C free-air temperature (unless otherwise noted)

	2N6451 2N6452 2N6453 2N6454
Drain-Gate Voltage.	20 V 25 V
Reverse Gate-Source Voltage	-20 V -25 V
Continuous Forward Gate Current	← 10 mA →
Continuous Device Dissipation at (or below) 25°C Free-Air Temperature (See Note 1). . .	← 360 mW →
Storage Temperature Range	-65°C to 200°C
Lead Temperature 1/16 inch from case for 10 seconds	← 300°C →

NOTE 1: Derate linearly to 175°C free-air temperature at the rate of 2.4 mW/°C.
*JEDEC registered data.

*electrical characteristics at 25°C free-air temperature (unless otherwise noted)

PARAMETER		TEST CONDITIONS[†]		2N6451 MIN	2N6451 MAX	2N6452 MIN	2N6452 MAX	2N6453 MIN	2N6453 MAX	2N6454 MIN	2N6454 MAX	UNIT
$V_{(BR)GSS}$	Gate-Source Breakdown Voltage	$I_G = 1$ μA,	$V_{DS} = 0$	-20		-25		-20		-25		V
I_{GSS}	Gate Reverse Current	$V_{GS} = -10$ V, $V_{DS} = 0$			-0.1				-0.1			nA
		$V_{GS} = -15$ V, $V_{DS} = 0$					-0.5				-0.5	nA
		$V_{GS} = -10$ V, $V_{DS} = 0$	$T_A = 125$°C		-0.2				-0.2			μA
		$V_{GS} = -15$ V, $V_{DS} = 0$					-1				-1	μA
$V_{GS(off)}$	Gate-Source Cutoff Voltage	$V_{DS} = 10$ V,	$I_D = 0.5$ nA	-0.5	-3.5	-0.5	-3.5	-0.75	-5	-0.75	-5	V
I_{DSS}	Zero-Gate-Voltage Drain Current	$V_{DS} = 10$ V, $V_{GS} = 0$, See Note 2		5	20	5	20	15	50	15	50	mA
$|y_{fs}|$	Small-Signal Common-Source Forward Transfer Admittance	$V_{DS} = 10$ V, $I_D = 5$ mA, f = 1 kHz		15	30	15	30					mmho
		$V_{DS} = 10$ V, $I_D = 15$ mA, f = 1 kHz See Note 3						20	40	20	40	mmho
$|y_{os}|$	Small-Signal Common-Source Output Admittance	$V_{DS} = 10$ V, $I_D = 5$ mA, f = 1 kHz			50		50					μmho
		$V_{DS} = 10$ V, $I_D = 15$ mA, f = 1 kHz, See Note 3							100		100	μmho
C_{iss}	Common-Source Short-Circuit Input Capacitance	$V_{DS} = 10$ V, $I_D = 5$ mA, f = 1 MHz			25		25					pF
		$V_{DS} = 10$ V, $I_D = 15$ mA, f = 1 MHz, See Note 3							25		25	pF
C_{rss}	Common-Source Short-Circuit Reverse Transfer Capacitance	$V_{DS} = 10$ V, $I_D = 5$ mA, f = 1 MHz,			5		5					pF
		$V_{DS} = 10$ V, $I_D = 15$ mA, f = 1 MHz, See Note 3							5		5	pF

*operating characteristics at 25°C free-air temperature

PARAMETER		TEST CONDITIONS[†]	2N6451 MIN	2N6451 MAX	2N6452 MIN	2N6452 MAX	2N6453 MIN	2N6453 MAX	2N6454 MIN	2N6454 MAX	UNIT
F	Common-Source Spot Noise Figure	$V_{DS} = 10$ V, $I_D = 5$ mA, $R_G = 10$ kΩ, f = 10 Hz		1.5		2.5		1.5		2.5	dB
V_n	Equivalent Input Noise Voltage	$V_{DS} = 10$ V, $I_D = 5$ mA, f = 10 Hz		5		10		5		10	nV/√Hz
		$V_{DS} = 10$ V, $I_D = 5$ mA, f = 1 kHz		3		8		3		8	nV/√Hz

*JEDEC registered data
[†]The fourth lead (case) is connected to the source for all measurements.
NOTES: 2. This parameter must be measured using pulse techniques. $t_W = 300$ μs, duty cycle ≤ 2%.
  3. To obtain repeatable results, this parameter must be measured with bias conditions applied for less than five seconds.
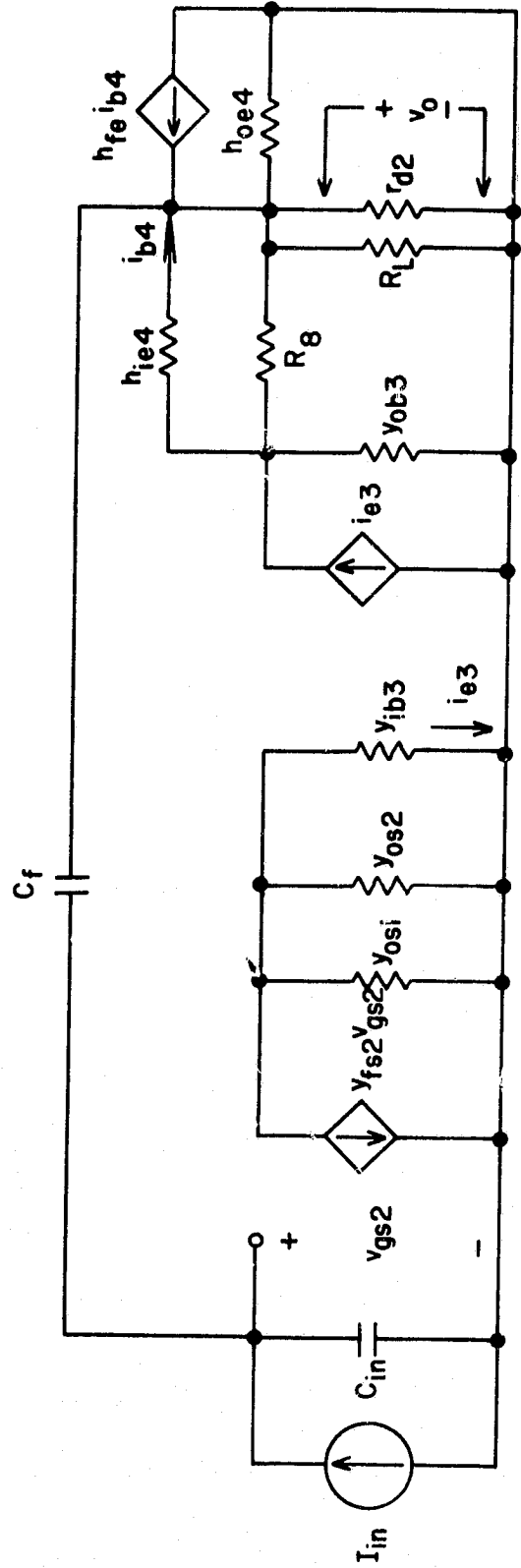
Figure 5.5 Small signal model of charge preamplifier (midband frequencies).

capacitance, and stray shunt capacitances.

At 1 MHz the susceptance of C_f is about 3% of the conductance present at the output; it will be assumed that this added capacitance does not affect the phase relationships at that point in the circuit. With this assumption, C_{in} and C_f will divide v_o while maintaining the phase at v_o. The small signal models used for feedback calculations are shown in Figure 5.6.

The parameters used for the active devices are summarized in Table 5.2. These values represent the information that is available for the appropriate operating conditions. It should be noted that y_{ob} and y_{rb} for Q_3 represent upper bounds; no information was available regarding how close these parameters come to the upper bound.

The input impedance of the shaper will be shown later to be much less than 5 kΩ so that R_L in the equivalent circuits is taken as 5 kΩ (pure resistance) (i.e., R_{39}).

The output portion of the small signal model will be considered first, Q_3 and Q_4. The relationship between i_{e3} and v_o is given below:

$$\frac{v_o}{i_{e3}} = \frac{1}{y_L\{(y_{ob3} + 1/h_{ie4} + y_8)/[(h_{fe4} + 1)/h_{ie4} + y_8]\} + y_{ob3}}$$

(5.4)

Simplification of this expression is difficult to justify. If y_{ob3} is assumed to be 10 µS (recall that we only have a bound on y_{ob3}, not a typical value) and use the typical values for the other parameters, we find that

$$\frac{v_o}{i_{e3}} = \frac{1}{(1+10)} \qquad \text{(megohm)}$$

and we simplify equation (5.4) so that

$$\frac{v_o}{i_{e3}} = \frac{1}{y_{ob3}}$$

(5.5)

If we consider $y_{ob3} = 1$ µS, we find

$$\frac{v_o}{i_{e3}} = \frac{1}{0.93 + 1} \approx \frac{1}{2} \qquad \text{(megohm)}$$
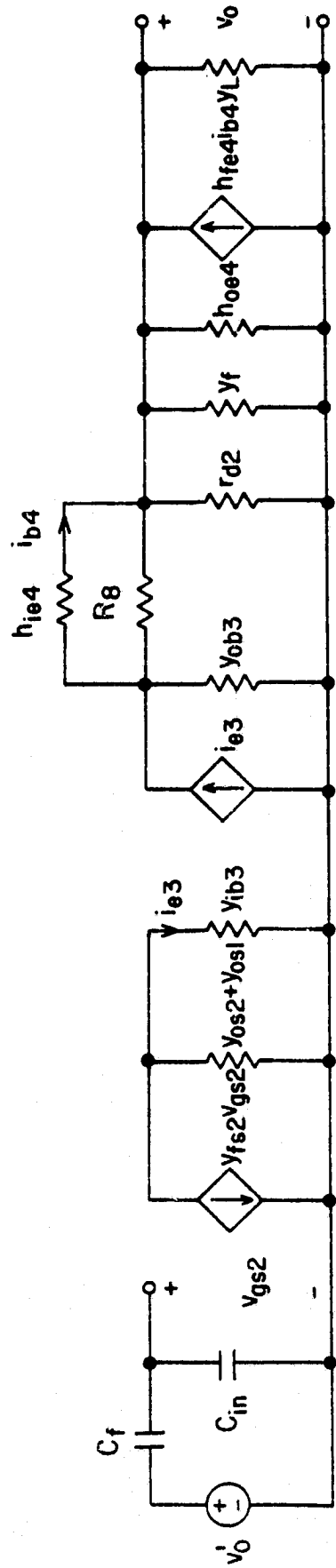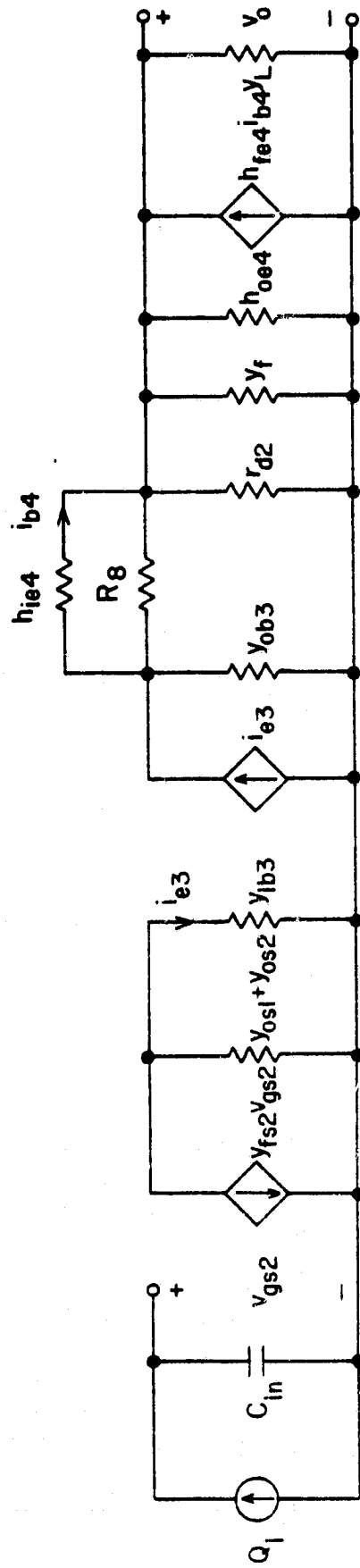
Figure 5.6 Models used for feedback calculations. (a) Model for calculating loop gain. (b) Model for calculating open-loop gain.

Table 5.2

Active device parameters.

DEVICE	PARAMETER	CONDITION
Q_1 2N4416	$y_{is} = 0.1 - j\ 2.5$ mS max	$V_{gs} = 0$ V, $f = 100$ MHz
	$\|y_{os}\| = 0.05$ mS max	$V_{gs} = 0$ V, $f = 1$ kHz
	$\|y_{fs}\| = 4.5$ mS min, 7.5 mS max	$V_{gs} = 0$ V, $f = 1$ kHz
	$I_{GSS} = -0.1$ nA max	$T_A = 25°C$, $V_{GS} = -20$ V, $V_{DS} = 0$
	$I_{DSS} = 5$ mA min, 15 mA max	$V_{GS} = 0$ V, $V_{DS} = 15$ V
Q_2 2N6451	$C_{iss} = 25$ pF max	$V_{DS} = 10$ V, $I_D = 5$ mA, $f = 1$ MHz
	$C_{rss} = 5$ pF max	$V_{DS} = 10$ V, $I_D = 5$ mA, $f = 1$ MHz
	$\|y_{fs}\| = 15$ mS min, 30 mS max	$V_{DS} = 10$ V, $I_D = 5$ mA, $f = 1$ kHz
	$\|y_{os}\| = 50$ μS max	$V_{DS} = 10$ V, $I_D = 5$ mA, $f = 1$ kHz
	$I_{DSS} = 5$ mA min, 20 mA max	$V_{DS} = 10$ V, $V_{GS} = 0$ V
	$I_{GSS} = -0.1$ nA	$T_A = 25°C$, $V_{GS} = -10$ V, $V_{DS} = 0$ V
Q_3 2N4957	$h_{FE} = 20$ min 40_{TYP}	$I_C = 2$ mA, $V_{CE} = 10$ V
	$g_{ib} = 56$ mS$_{TYP}$	$V_{CB} = 10$ V, $I_C = 2$ mA, $f = 45$ MHz
	$g_{fb} = -58$ mS$_{TYP}$	$V_{CB} = 10$ V, $I_C = 2$ mA, $f = 45$ MHz
	$y_{ob} < 0.05$ mS$_{TYP}$	$V_{CB} = 10$ V, $I_C = 2$ mA, $f = 45$ MHz
	$y_{rb} < 0.005$ mS$_{TYP}$	$V_{CB} = 10$ V, $I_C = 2$ mA, $f = 45$ MHz
Q_4 2N4044	$H_{FE} = 225$ min	$I_C = 1$ mA, $V_{CE} = 5$ V
	$C_{cbo} = 0.8$ pF max	
	$I_{CBO} = 0.1$ nA	
	Noise = 2 dB max	
	$f_t = 200$ MHz	$I_C = 1$ mA
	$h_{fe} = 250$ TYP	$I_C = 1$ mA, $V_{CE} = 5$ V
	$h_{ie} = 9.6$ kΩ TYP	$I_C = 1$ mA, $V_{CE} = 5$ V
	$h_{re} = 4.2 \times 10^{-4}$ TYP	$I_C = 1$ mA, $V_{CE} = 5$ V
	$h_{oe} = 12$ μS TYP	$I_C = 1$ mA, $V_{CE} = 5$ V
D_2 1N5288	Field-effect current regulator diode	
	Regulator current:	
	0.39 mA nom, 0.351 mA min, 0.429 mA max	$V_T = 25$ V
	Minimum dynamic impedance:	
	4.10 MΩ	$V_T = 25$ V
	Minimum knee impedance:	
	1.00 MΩ	$V_K = 6.0$ V
	Maximum limiting voltage	
	1.05 V	$I_L = 0.81$ (regulating current)

we see that we cannot simplify equation (5.4) when y_{ob3} becomes small. In this case we may only make one assumption, $(h_{fe4}+1)/h_{ie4} \gg y_8$, and obtain

$$\frac{v_o}{i_{e3}} = \frac{(h_{fe4} + 1)/h_{ie4}}{y_L(y_{ob3} + 1/h_{ie4} + y_8) + y_{ob3}[(h_{fe4} + 1)/h_{ie4}]} \tag{5.6}$$

To continue the circuit description equation (5.5) is used because of its simpler form. The only place that $1/y_{ob3}$ occurs is in the v_o/i_{e3} relation, so we must use equation (5.6) rather than equation (5.5) in the following analysis when the magnitude of y_{ob3} is in doubt.

The relation between v_{gs2} and i_{e3} is given by

$$i_{e3} = \frac{-y_{ib3}}{y_{ib3} + (y_{os1} + y_{os2})} y_{fs2} \, v_{gs2} \tag{5.7}$$

Since y_{os1} and $y_{os2} \gg y_{ib3}$, we have

$$i_{e3} \approx -y_{fs2} \, v_{gs2} \tag{5.8}$$

Combining equations (5.8) and (5.5) we obtain the open-loop voltage gain

$$A_v = \frac{v_o}{v_{gs2}} = \frac{-y_{fs2}}{y_{ob3}} \tag{5.9}$$

The open-loop charge gain, A_Q, is found by considering $v_{gs} = Q_i/C_{in}$, so that

$$A_Q = \frac{v_o}{Q_i} = \frac{-y_{fs2}}{y_{ob3} \, C_{in}}$$

Up to this point we have not considered the effects of feedback. Having obtained the open-loop gain, and noting that the open-loop input capacitance is C_{in}, we apply the feedback relations to find the voltage gain, charge gain, and input capacitance with feedback (A_{vf}, A_{Qf}, C_{eff}).

$$A_{vf} = \frac{A_v}{1-T} \qquad A_{Qf} = \frac{A_Q}{1-T} \qquad C_{eff} = C_{in}(1-T) \tag{5.11}$$

Where T is the loop gain, v_o/v_o', modeled in Figure 5.6(a).

The only difference between Figures 5.6(a) and 5.6(b) is the capacitive divider on the input of 5.6(a). We find directly that

$$T = \frac{C_f}{C_f + C_{in}}$$

and

$$A_v = \frac{-y_{fs2}}{y_{ob3}} \left[\frac{C_f}{C_f + C_{in}} \right] \tag{5.12}$$

Using $y_{fs} = 30$ μS; $C_{in} = 250$ pF, and $y_{ob3} = 1$μS we find that $T = -30$ (here equation (5.6) was used rather than equation (5.5)). With this value of loop gain $1-T$ can be approximated by $-T$. Inserting equation (5.12) into the feedback relationships (5.11) we find

$$A_{vf} \approx \frac{-C_{in}}{C_f} ; \qquad A_{Qf} \approx \frac{-1}{C_f} ; \text{ and } C_{eff} \approx \frac{y_{fs1}}{y_{ob3}} C_f = A_v C_f \tag{5.13}$$

Note that the relationships of equations (5.13) are the same as the relationships of equations (5.1), (5.2), and (5.3).

If worst-case values are considered for y_{ob3}, y_{fs2}, h_{ie4}, and C_{in}, the loop gain can become rather small due to the large attenuation of the feedback signal by the voltage divider formed by C_f and C_{in}. This will be considered again in Chapter 8.

Up to this point R_4 has been ignored; since it only seems to degrade the preamplifier performance as described, its presence must be explained. The ideal charge preamplifier would produce a staircase output waveform; the size of the steps would correspond to the energy of the incident particle that produced the step. A practical amplifier, with finite supply voltages, would eventually be driven into saturation. To prevent this a resistor is included across the feedback capacitor to discharge the accumulated voltage.

The time constant of $C_f R_f$ should be large compared to the time constants associated with the pulse-shaping electronics, τ, in order to prevent degradation of the filtered (shaped) signal. In this circuit $C_f R_f = 500$ μs while τ is between 0.5 and 2 μs.

The time constant of $C_f R_f$ must be small enough to insure that saturation will not occur during periods of high count rates. More sophisticated methods of discharging C_f have been developed but because of their complexity they are not well suited for rocket-borne applications and they will not be considered here.

C-2

5.2.3 *The test input.* To fully calibrate the system requires a vacuum chamber, a calibrated particle accelerator, and a detector. This test setup is inconvenient for bench work. The EPS is checked with a particle accelerator before launch to ensure proper operation; but much information can be obtained with a pulse generator before this time. A test input is provided in the preamplifier that allows calibration and testing using a pulse generator rather than a particle flux incident on a detector.

The components associated with the test input are C_3 and R_3. The model of the test input is given in Figure 5.7; C_{eff} is the effective input capacitance of the amplifier, discussed in Section 5.2.1. The pulse generator used is an Ortec Model 448 pulse generator. This pulse generator will provide a pulse with a very short rise time, 20 ns, and a long decay time constant, 1000 µs; the pulse height can be varied between 0.0000 V and 10.0000 V. Built-in attenuators and a normalization control can be used to calibrate the pulse generator scale in terms of simulated particle energy.

The pulse generator has an output impedance of 100 Ω. Resistor R_3 is included to terminate the cable connecting the pulse generator and the preamplifier. The capacitor C_3 and the effective input capacitance (C_{eff}) form a voltage divider that attenuates the test signal, v_{gen}. This attenuation is described in equation (5.14)

$$v_{gs2} = \left(\frac{C_3}{C_3 + C_{eff}} \right) v_{gen} \approx \frac{1 \text{ pF}}{C_{eff}} v_{gen} \tag{5.14}$$

For a typical preamplifier this corresponds to an attenuation of about 5000.

A test pulse with a short rise time is required to simulate the charge pulse of a detector. Ideally the generator would produce a staircase waveform to simulate the increasing voltage across C_{eff} due to periodic charge pulses; C_3 and C_{eff} form a voltage divider and v_{gs} should follow v_{gen}. In reality, there is a shunt resistance across C_{eff} which will discharge C_{eff} even if v_{gen} was held constant. The decay time constant of the pulse generator should be longer than the decay time constant of the preamplifier ($R_f C_f = 0.5$ ms) in order to simulate a charge pulse. Photographs of the test signal, v_{gen}, and the resulting preamplifier output, v_o, are shown in Figure 5.8.

The entire EPS can be tested using the test input: signal shape, linearity, and gain can be measured using the simulated input. If C_{eff} is
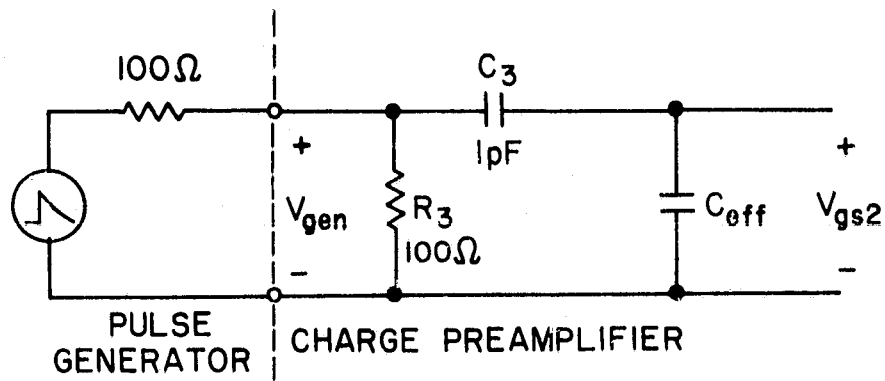
Figure 5.7 Model of test input.

(a)

(b)
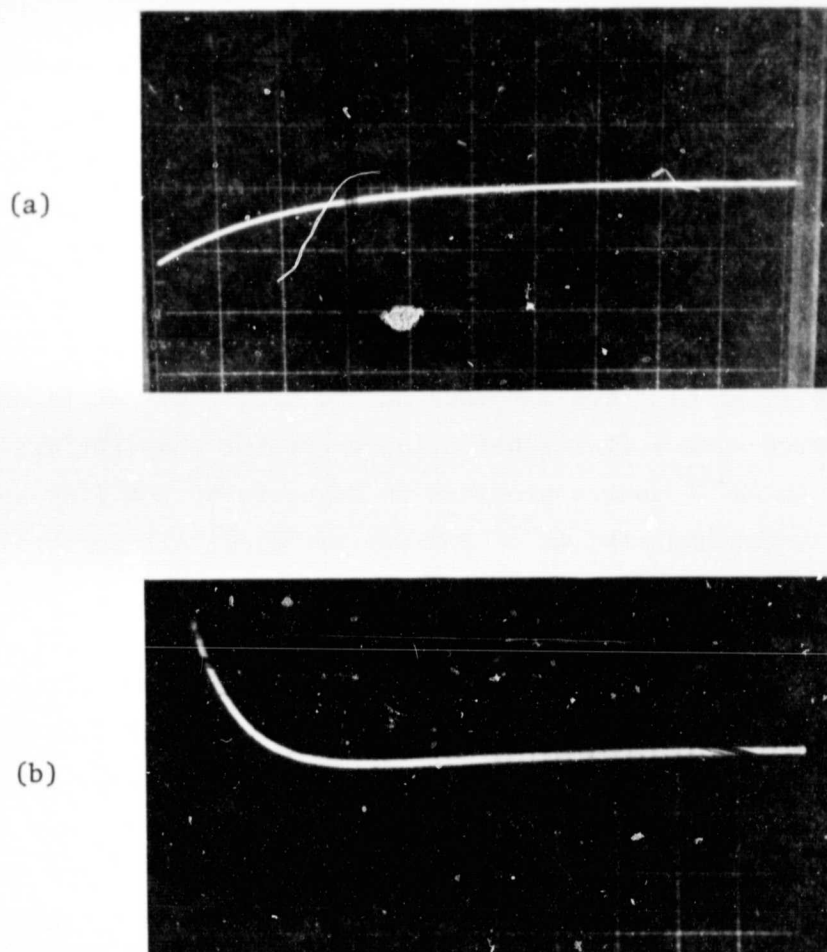
Figure 5.8   (a) The signal from the pulse generator; and (b) the
            resulting preamplifier output. The input signal
            was applied to an external test box rather than
            the test input. In this case the value correspond-
            ing to C_3 is 260 pF, not 1 pF. Horizontal scale
            0.5 ms/div; vertical scale 5 mV/div.

accurately known, the pulse generator output voltage can be adjusted to correspond to a given energy level. However, a more accurate and convenient method is available: a detector is connected to the preamplifier and a suitable radioactive source is used to provide a calibrated signal.

An X-ray source can be used with the detector on the bench and no vacuum chamber is required. This also has the advantage of allowing gold detectors to be covered to prevent light from saturating the detectors; the X-rays will pass through the covering. X-rays are not affected by the detector dead zone; however, the majority of X-rays will pass through the detector without transferring energy to an electron and thus not be measured. It is necessary to use an X-ray source with a flux substantially greater than the desired measurement rate. An Am^{241} source provides an accurate 60 keV line and has a long half-life. Unfortunately, Am^{241} sources are difficult to obtain. A Cd^{109} source will provide 22 keV X-rays and 88 keV gamma rays. Another useful source is Co^{57} which provides 122 keV and 136 keV gamma rays.

To calibrate the pulse generator, the pulse amplitude due to the radioactive source and the corresponding energy is noted. Then the pulse generator dial is set to the energy level measured and the attenuators and normalization control are adjusted until the pulse height matches the pulse height obtained from the radioactive source. Since electrons encounter little attenuation in the dead zone, the pulser is calibrated in terms of energetic electrons.

In addition to convenience the use of the pulser has another advantage. The higher the shunt capacitance on the preamplifier input the higher the noise on the output. By removing the detector one obtains improved resolution for system tests.

5.2.4 *Measurement of preamplifier parameters*. The model of the charge preamplifier presented in Section 5.2.2 gave a general indication of the operation of the preamplifier. Many of the parameters of the resulting equations are, however, transistor parameters which tend to be quite variable from unit to unit. To confirm that the preamplifier operates as expected, some measurements were taken on a typical unit.

The low signal levels and the requirement of dynamic measurement present problems. The primary parameters of interest are A_v and C_{eff}. To measure these parameters a special test box was built; this box will now be described, then the measurements will be discussed.

The schematic of the test box and its relation to the preamplifier input circuit is shown in Figure 5.9. The test box is connected between the preamplifier input and the pulse generator output. The operation is similar to the test circuit that is internal to the preamplifier; however, the series capacitance of the test box is composed of two equal capacitors in series. The test box is well shielded because of the low signal levels; and it provides two test points to allow measurement of v_s.

To measure C_{eff}, we make use of the fact that capacitors in series all have the same charge. Therefore,

$$Q_{C_{eff}} = v_s C_t = v_{gs} \, C_{eff} \tag{5.15}$$

Using the relationship for a capacitative divider

$$v_{gs} = \left[\frac{C_t/2}{C_t/2 + C_{eff}} \right] v_t \tag{5.16}$$

we find

$$C_{eff} = C_t \left[\frac{1}{v_t/v_s - 2} \right] \tag{5.17}$$

The measurement points on the test box allow us to determine v_t and v_1; C_t is known, so C_{eff} can be calculated. Once C_{eff} is calculated, it can be used in equation (5.16) to determine v_{gs}; if the output voltage is also measured, A_v can be determined.

The voltage v_s will change as C_{eff} discharges through R_f (time constant given by $C_{eff} R_f$); this requires a dynamic measurement. v_t and v_1 can be measured with an oscilloscope. A high input impedance and low shunt capacitance is required to prevent interaction with the test box. This implies that C_t should be large; however, to provide attenuation and obtain a large sample voltage a small C_t is desirable.

A Tektronix 7A18 plug-in with a P6011 ×1 probe was used to measure v_t and v_1. This results in an impedance of 1 MΩ shunted by approximately 32 pF at the test point. To swamp out the effects of the oscilloscope probe, C_t was chosen as 510 pF; unfortunately this requires operation of the preamplifier with unusually high input levels in order to obtain a measurable sample voltage, v_s. Fortunately, the gain measurements indicate linear operation of the preamplifier even at the high input levels.
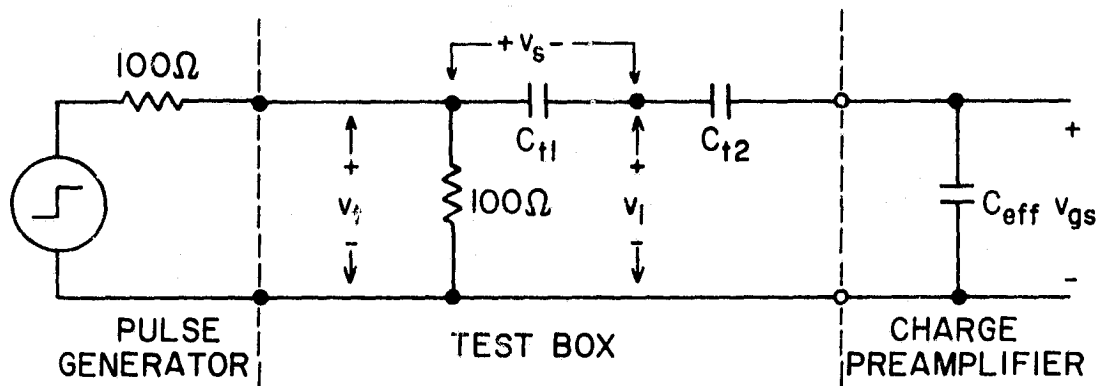
Figure 5.9   Schematic diagram of the test box.   For analysis purposes
$C_{t1} = C_{t2} = C_t$.

After the test box was constructed, several tests were made using known capacitances across the output. With $C_{t1} = C_{t2}$, v_s was larger than expected. To correct this, several different capacitors were tried across C_{t1} to reduce v_s to the expected level; the results obtained with two of these capacitors are tabulated in Table 5.3. Since the expected value of C_{eff} is on the order of 5000 pF, the 68 pF shunt capacitor (across C_{t1}) was chosen because of the more accurate results obtained when a short was used in place of C_{eff}. Larger values of known capacitance were not used because of connection problems. The voltage measurements are only accurate to about ±150 μV because of the minimum scale of 5 mV/cm. It should also be noted that high frequency oscillations were present (2 mV p-p at 100 MHz); since these were observed when the oscilloscope was measuring v_t whether the pulse generator or the preamplifier was connected or not, it is assumed the oscillation was internal to the oscilloscope. By using the 20 MHz band-limiting filter that is built into the oscilloscope the oscillations were eliminated.

The data taken on the charge preamplifier is summarized in Table 5.4. The measurements with a pulser setting of 100 and 200 were discarded because of the high percentage error in the measurements. The measurement with a pulser setting of 400 is discarded because of the large disagreement with the remaining measurements. Averaging the remaining measurements we find

$$|A_v| = 7500 \qquad C_{eff} = 5500 \text{ pF} \qquad (5.18)$$

To check for any variation in A_v or C_{eff} with a change in the input capacitance a length of cable corresponding to approximately 40 pF was added between the test box and the preamp. The readings were identical indicating good stability for moderate changes in input capacitance.

The experimental data can be compared with the model derived in the previous section. Additionally, some interesting parameters, such as typical v_{gs} and v_o values, will be calculated.

Using the relations given at (5.13) we see

$$|A_{v,\text{model}}| = \frac{C_{eff,\text{measured}}}{C_f} = 11,000 \qquad (5.19)$$

Considering that C_f is specified as 0.5 ±0.25 pF this agrees fairly well with the value of 7500.

Table 5.3

Data from evaluation of test box.

SHUNT ACROSS C_{t1} (pF)	v_t (mV)	v_1 (mV)	v_s (mV)	CALCULATED		MEASURED	
				C_{eff} (pF)	v_{gs} (mV)	C_{eff} (pF)	v_{gs} (mV)
100	20	10.3	9.7	(expect v_s = 10.0 mv)		short	-
100	15	9.9	5.1	542	4.80	510	4.8
100	20	12.5	7.5	765	5.00	750	4.9
68	20	10.0	10.0	(expect v_s = 10.0 mv)		short	-
68	15	9.8	5.2	577	4.6	510	4.8
68	20	12.4	7.6	808	4.8	750	4.9

Table 5.4

Data from measurements of charge preamplifier.

PULSER SETTING	v_t (mV)	v_1 (mV)	v_s (mV)	v_o (V)	C_{eff} (pF)	v_{gs} (µV)	$|A_v|$
100	2.9	1.5	1.4	1.05	7140	100	10,500
200	6.2	3.1	3.1	2.10	-	-	-
300	9.4	4.9	4.5	3.15	5740	400	7,870
400	12.6	6.7	5.9	4.20	3760	800	5,250
500	15.9	8.3	7.6	5.20	5540	700	7,430
600	19.1	10.0	9.1	6.35	5160	900	7,060

The charge sensitivity is given by

$$A_{Q_f,\text{model}} = - \frac{1}{C_f} = -2 \times 10^{12} \text{ V/C} \qquad (5.20)$$

Consider a 50 keV energetic electron: this particle will produce a charge $Q_{in} = 2.3 \times 10^{-15}$ C. Using the measured values of C_{eff} and A_v, we find $v_{gs} = 0.42$ μV and $v_o = 3.13$ mV. Equation (5.20) predicts $v_o = 4.6$ mV, which is quite a reasonable agreement.

Using the measured value of A_v in equation (5.9) with $y_{fs2} = 15$ mS, we find $y_{ob3} = 2.0$ μS; with $y_{fs2} = 30$ mS we obtain $y_{ob3} = 4.0$ μS, (these are minimum and maximum values of y_{fs2}). This implies an effective value of y_{ob3} of about 3 μS, an effective value because a y_{ob3} as small as this requires the use of equation (5.6) rather than equation (5.5). The value for y_{ob} is reasonable for relatively low frequencies. All the above results indicate good agreement between the model and the actual preamplifier.

5.3 *Shaping Filter*

5.3.1 *Selection of the filter.* Chapter 4 describes the noise sources within the preamp and presented the optimal filter characteristics (optimal in terms of noise performance). The results of the analysis of several practical filters are presented in Figure 4.9. In this section we explain why the $(CR)^i \cdot (RC)^j$ family of filters was selected.

Reviewing Figure 4.9 and using the relative equivalent noise charge as a figure of merit, we see that the filters using delay lines have the best noise performance. In fact the $(DL)^2 \cdot RC$ filter closely approximates the optimal time-limited filter response.

Delay line shaping involves sampling the input signal, delaying the sample for a fixed time, multiplying the delayed sample by a constant, and then adding the modified sample to the actual. A schematic representation of a delay line filter is given in Figure 5.10(a). The input signal is actually a decaying exponential ($\tau = C_f R_f$, from the preamplifier) and this produces some undershoot in the output pulse, Figure 5.10(b). Losses in the delay line will result in a delayed signal that is smaller than the non-delayed signal, producing an offset voltage (by adjusting the level of the signals at the difference amplifier this can be eliminated). Problems arise related to the quality of the delay line. Improper termination, due to changes in the characteristic impedance of the line, or due to changes in the terminating resistors Z_o, produce reflections resulting in ringing
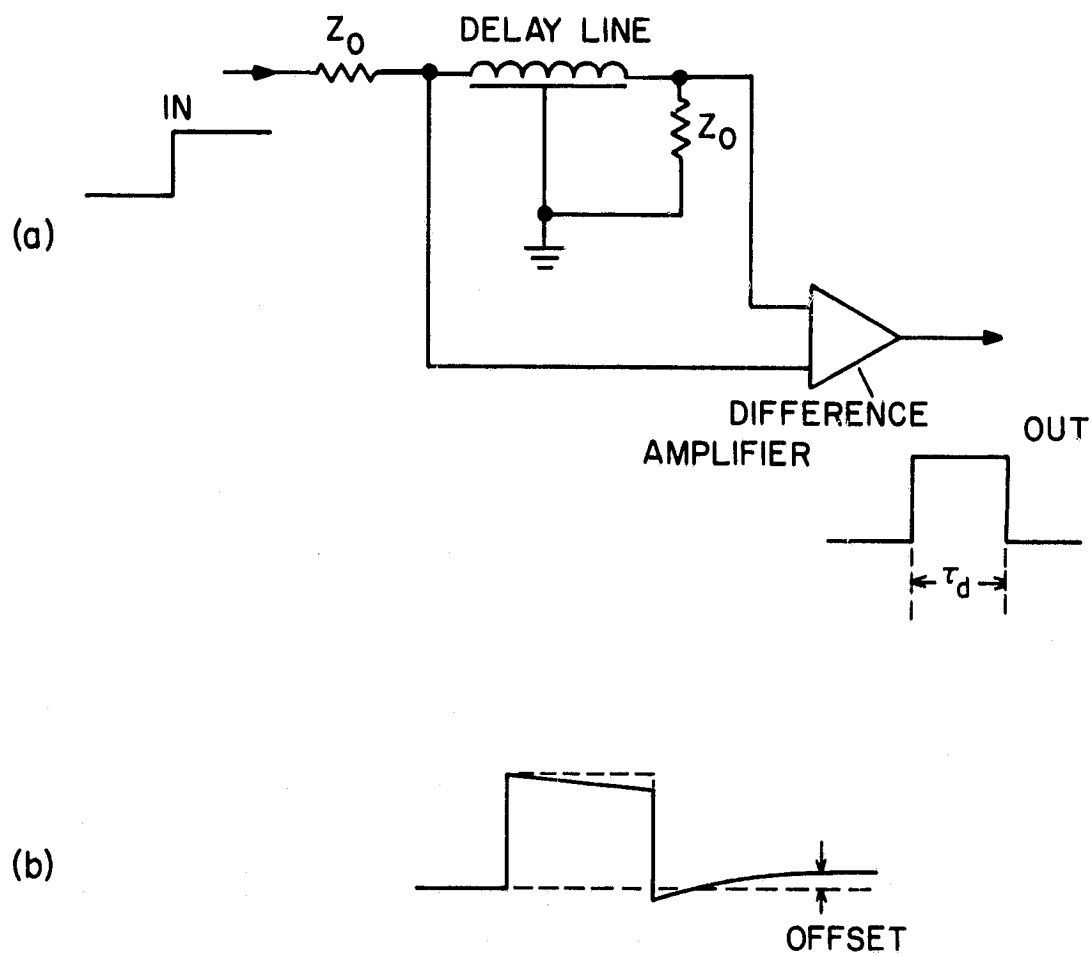
Figure 5.10 Delay-line pulse shaping. (a) Schematic representation
of delay line in pulse shaping applications. (b) A
more practical output pulse for the circuit of figure a,
showing some of the non-ideal characteristics.

and small amplitude variations of the output signal. Mismatches internal to the delay line will also produce these effects. Because of the problems discussed above th` delay line filters will not be considered for this application.

The $(CR)^i \cdot (RC)^j$ filters are attractive because of their straightforward and simple implementation (resistors, capacitors and amplifiers); these are two important requirements for rocket-borne applications where size, stability and high reliability are required. These filters will be divided into two groups, $(CR) \cdot (RC)^j$ and $(CR) \cdot (RC)^j$ filters.

The response obtained from a typical $(CR) \cdot (RC)^3$ filter is shown in Figure 5.11(a) and 5.11(b); two different time constants are represented. This type of filter produces a unipolar output, that is, the output of an ideal filter would never cross zero. Because of practical limitations the preamplifier and pulse-shaping electronics are ac coupled. In an ac-coupled system it is impossible to have a unipolar pulse (a qualification is noted here: zero cancelling is discussed below).

The output pulse has a small overshoot when it returns to zero (the pulse-height analyzer requires a negative signal pulse). Because of the low level this overshoot will persist for a long time, relative to the shaper time constant. This overshoot can be seen in Figure 5.11 and is expanded in Figure 5.12.

If a second pulse occurs before the tail due to the first pulse has decayed, the measured pulse height for the second pulse will be in error by an amount equal to the magnitude of the tail due to the first pulse. If the frequency of the unwanted zeros are known (one zero, $CR = \tau$, is desired to limit the duration of the signal pulse, i.e., low-pass filtering) a pole can be added to cancel the unwanted zero; this is termed zero cancelling.

If the interval between pulses is so short that the tail due to the previous pulse produces a significant error, a $(CR)^2 \cdot (RC)^j$ filter can be used. Figure 5.11(c) shows an output pulse from $(CR)^2 \cdot (RC)^2$ shaping filter; this particular filter produces a positive pulse. The second zero causes the magnitude of the undershoot to be about that of the main pulse; but the output returns to zero long before the output of a $(CR) \cdot (RC)^j$ filter.

From Figure 4.9 it can be seen that a $(CR)^2 \cdot (RC)^j$ filter has poorer noise performance than a $(CR) \cdot (RC)^j$ filter, given the same number of RC

(a)

(b)

(c)
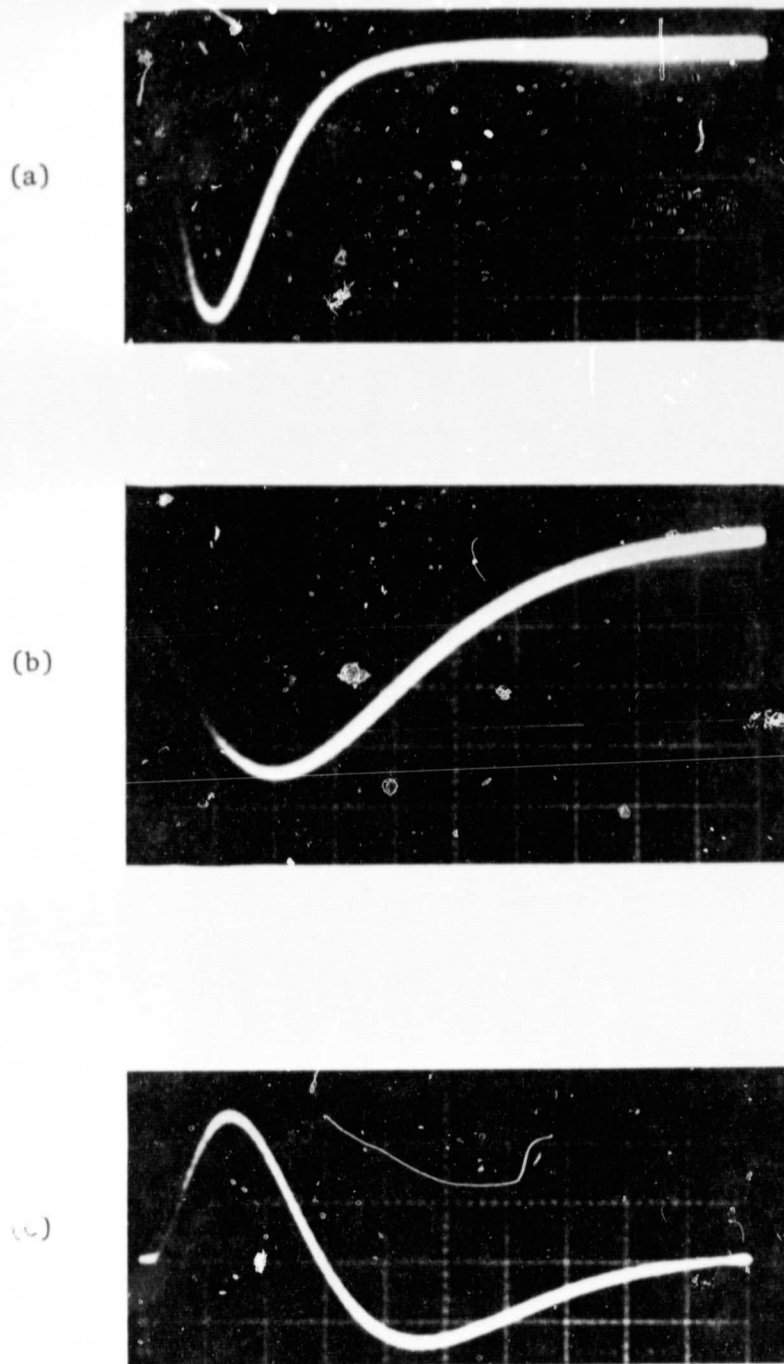
Figure 5.11 Photographs of output pulses obtained using various
shaping methods and time constants. (a) $(CR) \cdot (RC)^3$
shaper, $\tau = 1$ μs. Horizontal scale 2 μs/div; vertical
scale 2 V/div. (b) $(CR) \cdot (RC)^3$ shaper, $\tau = 2$ μs.
Horizontal scale 2 μs/div; vertical scale 2 V/div.
(c) $(CR)^2 \cdot (RC)^2$ shaper, $\tau = 0.5$ μs. Note that (c)
has a positive output pulse, as compared to the negative
output pulses for (a) and (b). Horizontal scale 0.5 μs/
div; vertical scale .2 V/div.

(a)

(b)
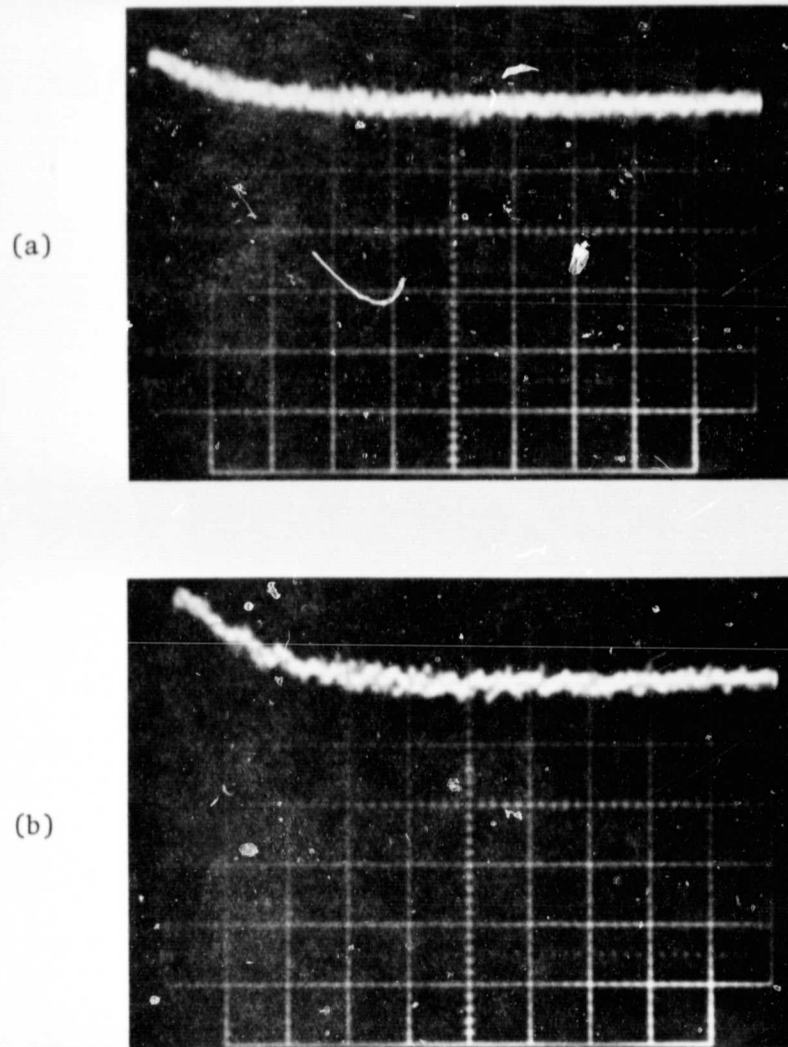
Figure 5.12   Photographs of the overshoot obtained when using a
               single (CR) stage. These are oscilloscope traces of
               the tails of the pulses shown in Figure 5.11(a) and
               5.11(b), respectively. The main pulse is off scale in
               these photographs. Horizontal scale 0.1 ms/div; vertical
               scale 0.5 V/div.

sections. For this reason a single CR section is desirable, if its use is possible. If the unwanted zeros vary with transistor parameters or temperature, zero cancelling may not be helpful and one would be forced to use a $(CR)^2 \cdot (RC)^j$ configuration. It should be noted that if pile-up occurs with a $(CR)^2 \cdot (RC)^j$ filter, very large errors will result; this is due to the large undershoot.

When choosing the number of (RC) sections (i.e., the value of j) the rule obtained from Figure 4.9 is: *the more the better!* By adding (RC) sections the filter step response becomes a better approximation to a Gaussian pulse. The choice of j is based on diminishing returns, for each section added the size and complexity of the shaping electronics increases. For the JASPIC system, $i = 1$, $j = 3$ was chosen. This results in a relative ENC between 1.22 and 1.16.

Having selected the filter type, $(CR) \cdot (RC)^3$, we must select τ. Chapter 4 discussed the selection of τ based upon noise considerations using the physical parameters of the preamplifier. Rather than attempting to model the preamplifier one can simply try different values of τ for the actual circuit. The designer must consider pile-up probabilities as well as noise performance when choosing τ.

Table 5.5 presents the probability of i pulses occurring in an interval of T seconds for two different particle fluxes. The count rate of 2000 s^{-1} was observed during high fluxes at high latitudes (actually the 1979 solar eclipse at Red Lake, Ontario). The count rate of 40 s^{-1} is representative of particle fluxes in the equatorial regions. Of particular interest is the column labelled $P\{X \geq 2\}$; this is the probability that two or more particles will be measured in the specified time interval. The probabilities of $P\{X \geq 2\}$ are used in determining the pile-up effects of a given shaping time constant, τ.

The probabilities of Table 5.5 were obtained by modeling the number of energetic particles measured in an interval of length T as a Poisson random process with $\lambda = $ flux $\times T$ (the flux measured in particles/s). The random variable X represents the number of energetic particles measured in the interval T. Thus $P(X = 1)$ is the probability of one particle being measured in the interval T, described by equation (5.21).

$$p(i) = P(X = i) = e^{-\lambda} \frac{\lambda^i}{i!}$$

(5.21)

Table 5.5

Probabilities of i particles being measured in an interval of length T. The process is modeled as a Poisson random process with the indicated τ.

INTERVAL, T (μs)	FLUX (PARTICLE/S)	λ	$P(x=i)$				$P(x \geq 2)$
			0	1	2	3	
5	2000	0.01	0.9900	0.00990	$4.950 \cdot 10^{-5}$	$1.650 \cdot 10^{-7}$	$4.967 \cdot 10^{-5}$
10		0.02	0.9802	0.01960	$1.960 \cdot 10^{-4}$	$1.307 \cdot 10^{-6}$	$1.974 \cdot 10^{-4}$
20		0.04	0.9608	0.03843	$7.686 \cdot 10^{-4}$	$1.025 \cdot 10^{-5}$	$7.790 \cdot 10^{-4}$
40		0.08	0.9231	0.07385	0.002954	$7.887 \cdot 10^{-5}$	0.003034
80		0.16	0.8521	0.1363	0.01091	$5.817 \cdot 10^{-4}$	0.01151
160		0.32	0.7261	0.2324	0.03718	0.003966	0.04148
320		0.64	0.5273	0.3375	0.1080	0.02304	0.1352
640		1.28	0.2780	0.3559	0.2278	0.09718	0.3661
1280		2.56	0.0773	0.1979	0.2533	0.2162	0.7248
2560		5.12	0.0598	0.0360	0.07833	0.1337	0.9634
5	40	0.0002	0.9998	$2.000 \cdot 10^{-4}$	$2.000 \cdot 10^{-8}$	$1.333 \cdot 10^{-12}$	$2.000 \cdot 10^{-8}$
10		0.0004	0.9996	$3.998 \cdot 10^{-4}$	$7.997 \cdot 10^{-8}$	$1.066 \cdot 10^{-11}$	$8.000 \cdot 10^{-8}$
20		0.0008	0.9992	$7.994 \cdot 10^{-4}$	$3.197 \cdot 10^{-7}$	$8.527 \cdot 10^{-11}$	$3.198 \cdot 10^{-7}$
40		0.0016	0.9984	0.001597	$1.278 \cdot 10^{-6}$	$6.816 \cdot 10^{-10}$	$1.279 \cdot 10^{-6}$
80		0.0032	0.9968	0.003190	$5.104 \cdot 10^{-6}$	$5.444 \cdot 10^{-9}$	$5.109 \cdot 10^{-6}$
160		0.0064	0.9936	0.006359	$2.035 \cdot 10^{-5}$	$4.341 \cdot 10^{-8}$	$2.039 \cdot 10^{-5}$
320		0.0128	0.9873	0.01264	$8.088 \cdot 10^{-5}$	$3.451 \cdot 10^{-7}$	$8.122 \cdot 10^{-5}$
640		0.0256	0.9747	0.02495	$3.194 \cdot 10^{-4}$	$2.726 \cdot 10^{-6}$	$3.221 \cdot 10^{-4}$
1280		0.0512	0.9501	0.04864	0.001245	$2.125 \cdot 10^{-5}$	0.001267
2560		0.1024	0.9027	0.09243	0.004733	$1.615 \cdot 10^{-4}$	0.004898

From Figures 5.11 and 5.12 we obtain the following values:

Filter type	τ	Time after event	Magnitude of tail
$(CR)^2 \cdot (RC)^2$	0.5 µs	4.5 µs	2%
		5.0 µs	~0
$(CR)^3 \cdot (RC)^3$	1 µs	10 µs	6%
		200 µs	1%
		400 µs	~0
	2 µs	20 µs	11%
		200 µs	4%
		400 µs	~0

Considering the probabilities given in Table 5.5 for a count rate of 2000 s^{-1} we see that the probability of pile-up producing any error for a 0.5 µs $(CR)^2 \cdot (RC)^2$ shaping filter is 0.005%. If a 1 µs $(CR) \cdot (RC)^3$ shaping filter is used, there is a probability of 0.02% that an error greater than 6% will result due to pile up, a 6% probability that an error greater than 1% will result due to pile up, and a 20% chance that some pile up (unspecified resulting error) will occur.

The results given above would be used in determining the filter characteristic and time constant to be used on a flight where a count rate of 2000 s^{-1} is expected. If an error of >6% is acceptable 0.02% of the time, a 1 µs $(CR) \cdot (RC)^3$ filter could be used. One must weigh the cost of those errors against the increase in noise (which can be modeled as an error) that will result by going to a $(CR)^2 \cdot (RC)^2$ filter. It should be noted that the percentage error that was specified above assumed that the second pulse was the same energy as the first; the error is actually additive, not multiplicative. The deviation from zero at a given time after a pulse is dependent on the specific electronics, and should be measured.

The noise performance of the electronics used on the JASPIC program improved as τ was increased (checked up to $\tau = 2$ µs). In general, the optimal time constant is in the range of 1 µs to 10 µs. The actual value depends upon the FET used in the input circuit. Therefore, there will usually be a trade-off between noise performance and pile-up. However, certain devices may actually perform best with smaller values of τ, so this should be checked for each transistor.

A block diagram of a $(CR)^i \cdot (RC)^3$ shaping amplifier is shown in Figure 5.13. In this case i can be equal to 1 or 2, depending on whether

104

DETECTOR | PREAMPLIFIER

SHAPING AMPLIFIER

C_3 SHORTED

C_3 INCLUDED

$(CR)(RC)$

$(CR)(RC)^2$

$(CR)(RC)^3$

$(CR)\cdot(RC)$

$(CR)^2\cdot(RC)$
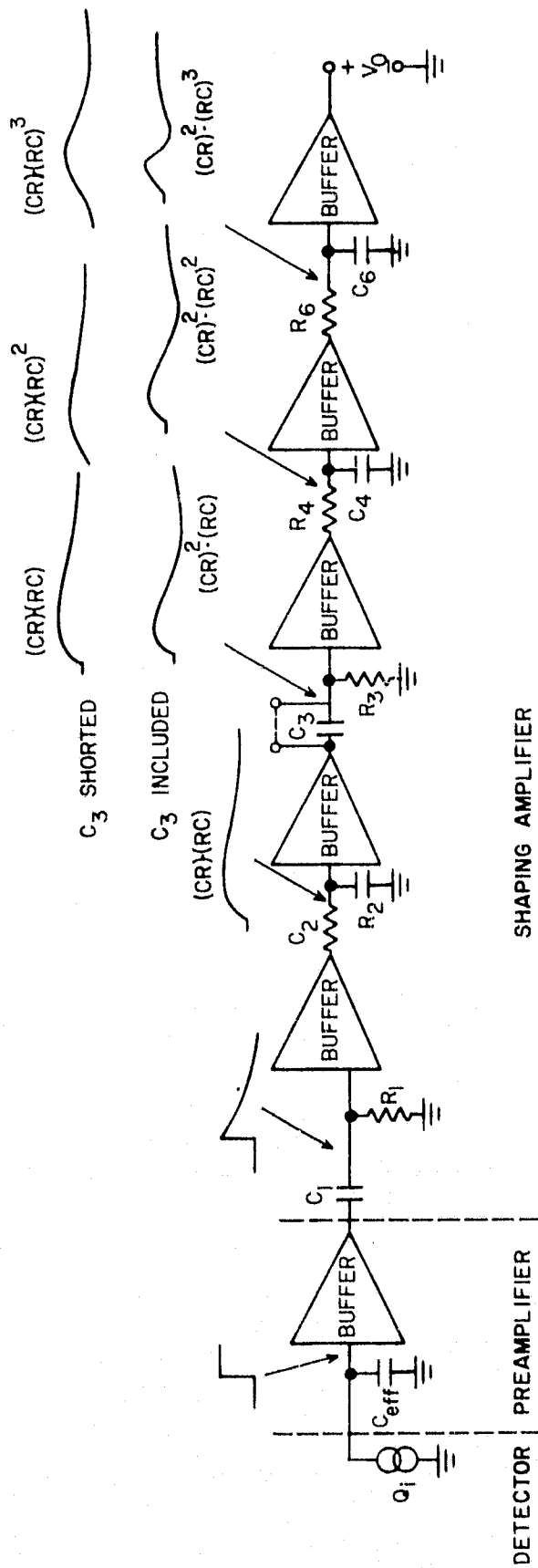
$(CR)^2\cdot(RC)^2$

$(CR)^2\cdot(RC)^3$

$C_1 R_1 = C_3 R_3 = \tau_1$

$R_2 C_2 = R_4 C_4 = R_6 C_6 = \tau_2$

$\tau_1 = \tau_2 = \tau$

Configuration shaper transfer function

$(CR) \cdot (RC)^3$

$$H(s) = \frac{\tau_1}{(1 + s\,\tau_1)\,(1 + s\,\tau_2)^3}$$

$(CR)^2 \cdot (RC)^3$

$$H(s) = \frac{\tau_1^2}{(1 + s\,\tau_1)^2\,(1 + s\,\tau_2)^3}$$

Figure 5.13 Block diagram and transfer function for $(CR)^i \cdot (RC)^3$ shaping filters (i = 1,2).

C_3 is shorted, or whether it is included. The transfer function and the signal shape at various points internal to the shaper are also shown. The only parameter of interest is the transfer function, any circuits can be used to realize the desired transfer function. When a circuit configuration is considered, the amplitude of the signal at various points in the circuit must be investigated to be sure that a section is not driven into saturation.

An amplifier that can be configured as a unipolar or bipolar (i.e., i = 1 or 2) pulse-shaping configuration is desirable because it allows selection of the filter type and time constants dependent upon the expected particle flux. The shaping amplifier should also be configured so that it can be used as an inverting or non-inverting amplifier. Gold and aluminum detectors require opposite polarity bias voltages, and produce opposite polarity charge pulses. Since the pulse-height analyzer used in the EPS only works with one polarity pulse (negative), the shaper must provide the correct polarity pulse.

The general properties of shaping amplifiers and the procedure used in selecting the filter characteristic and time constant have been discussed. In the next section the actual electronics used on the JASPIC flights will be discussed.

5.3.2 *Shaping amplifier circuit description*. The schematic of the shaping amplifier is given in Figure 5.14; a photograph is included in Figure 5.15. The shaping amplifier includes the switch that selects one of the two preamplifiers and the amplifier that determines whether the unit is inverting or non-inverting. Table 5.6 lists values for the components that are selected based on the specific shaping requirements.

The analog switch, U_i, is optional. If two detectors are to be used with one shaper (to minimize capacitance added by long cables, two preamplifiers are required) R_1, R_2, and U_1 are included; if the switching capability is not needed, a jumper is installed between J_1 and the input side of C_{40}. The on-and-off resistances of the switch are low and high enough to prevent interference with operation of the shaping amplifier.

The pulse shaping is accomplished in three gain blocks, consisting of Q_1/Q_2, Q_3/Q_4, and Q_5/Q_6. The small signal configuration is almost identical for each of the three gain blocks. The Q_1/Q_2 pair is configured slightly differently for biasing purposes. The small signal model of a gain
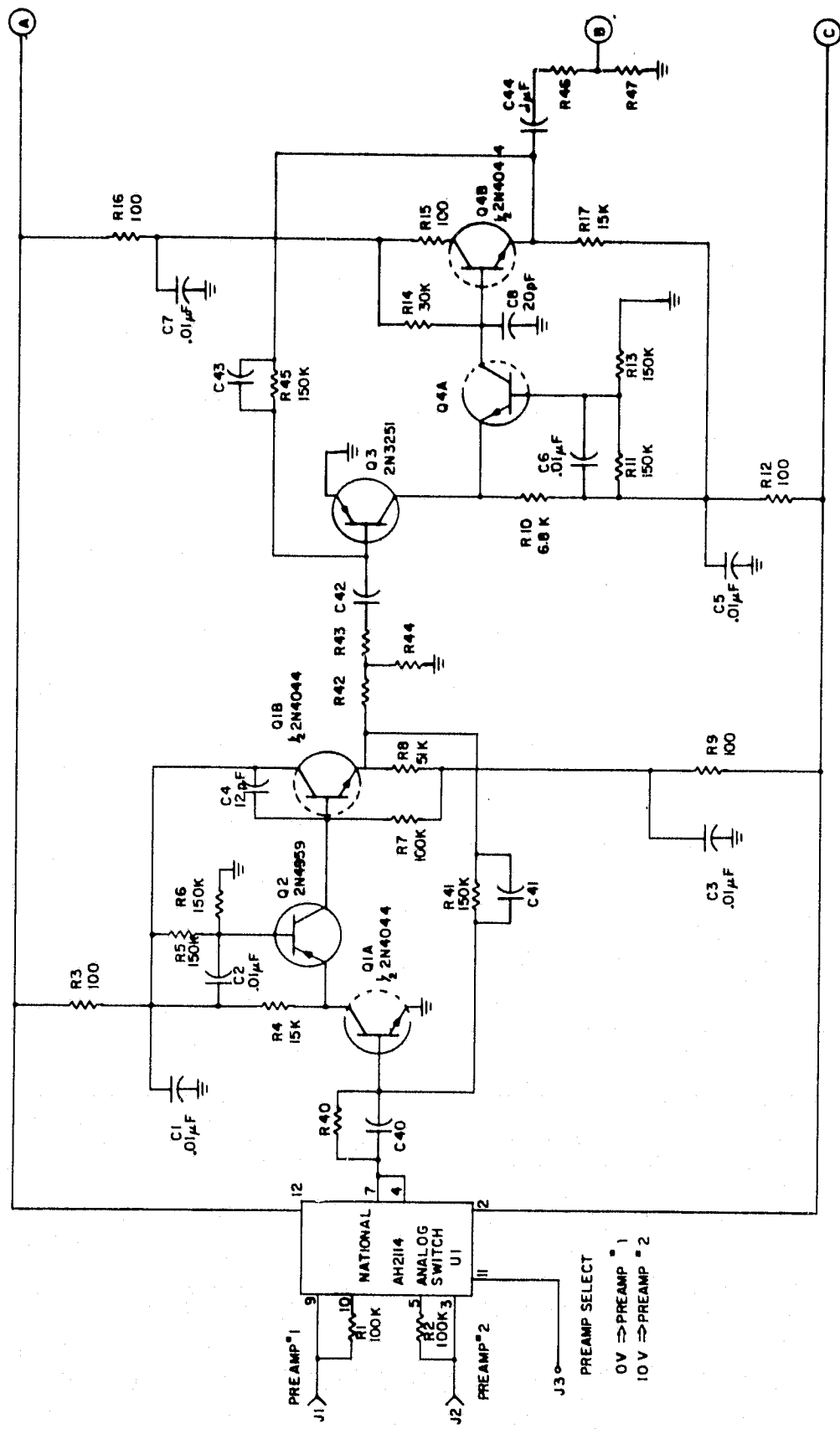
Figure 5.14   Schematic of shaping filter and analog switch.
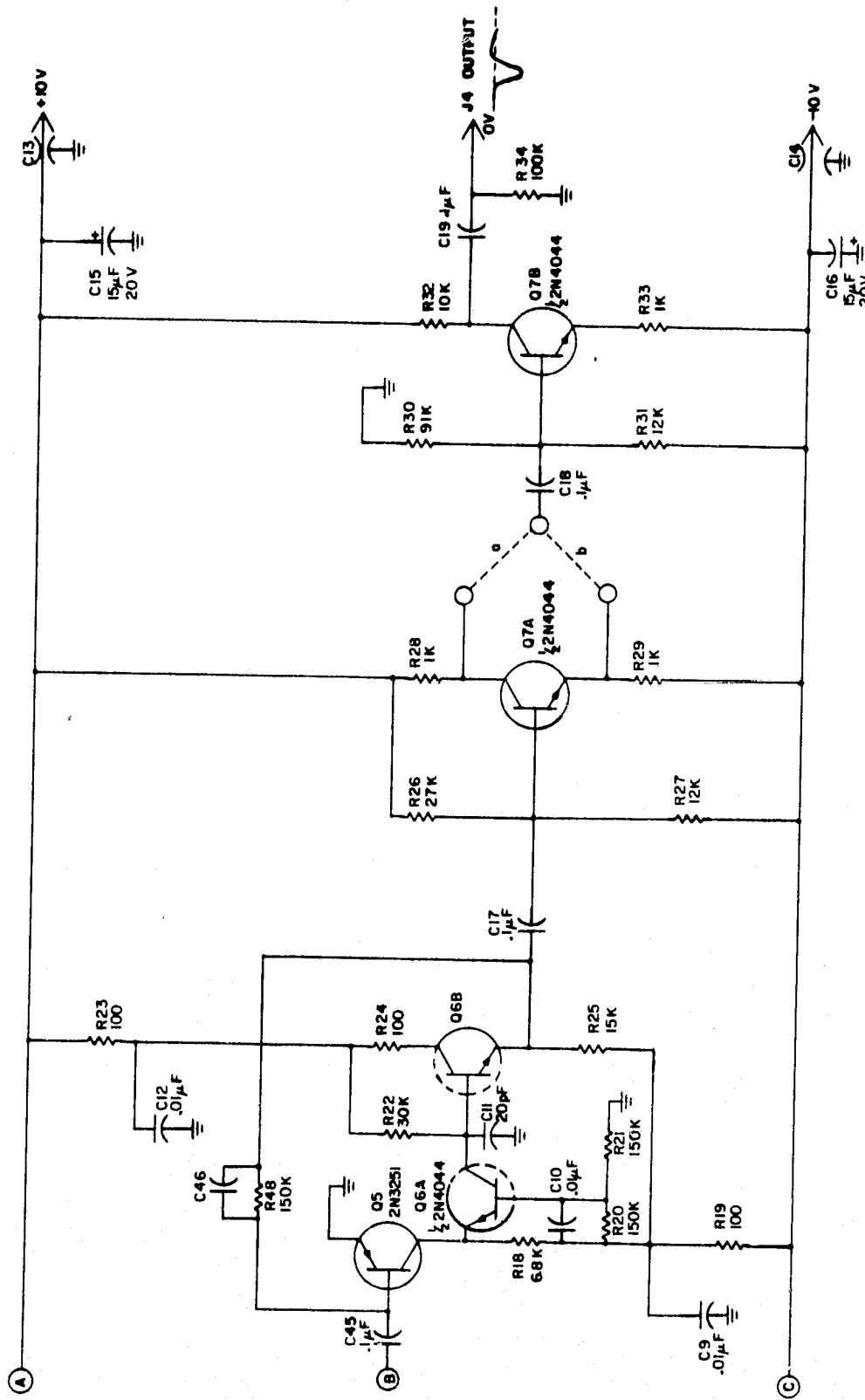
Figure 5.14 cont. Schematic of shaping filter. The polarity of the output pulse is adjusted by choosing either connection a or b on the output of transistor Q7A.
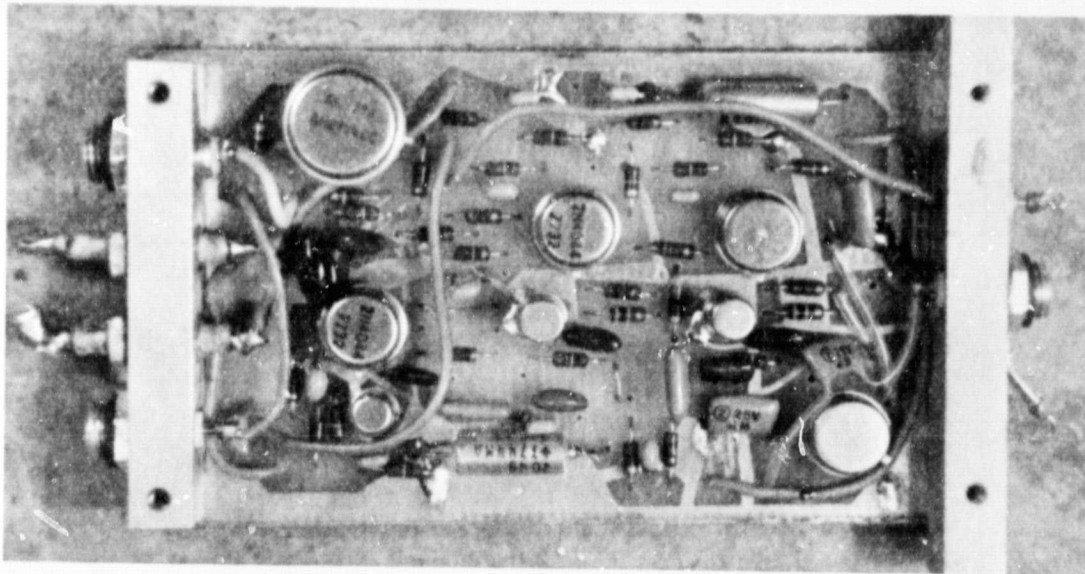
(a)
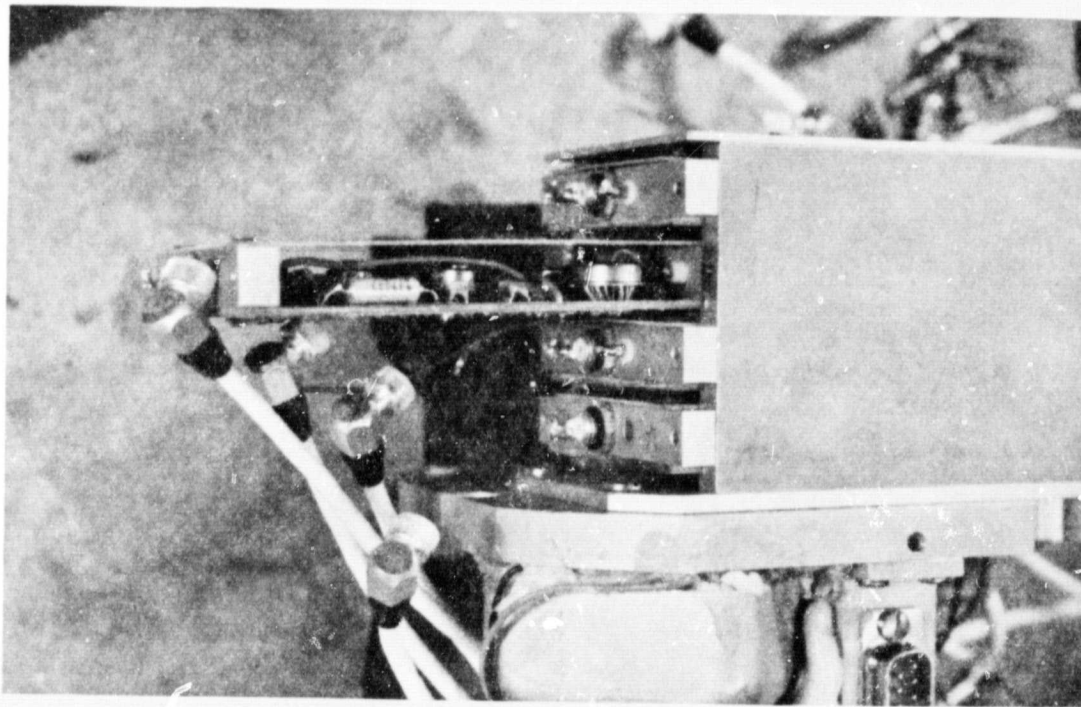
(b)

Figure 5.15   (a) The JASPIC shaping amplifier.
                (b) Packaging of the shaping amplifiers.

Table 5.6

Component values for selected components. Selected according
to desired time constant and required gain.

CONFIGURATION	COMPONENT	TIME CONSTANT		
		.5 µs	1 µs	2 µs
$(CR) \cdot (RC)^3$	C_{40}	100 pF	200 pF	390 pF
	R_{40}	5.1 M	2.4 M	1.3 M
	C_{41}	3.0 pF	6.0 pF	13 pF
	R_{42}	gain adjustment typical values		5.1k
	R_{43}			0
	R_{44}			∞
	C_{42}	.1 µF	.1 µF	.1 µF
	C_{43}	3.0 pF	6.0 pF	13 pF
	R_{46}	gain adjustment typical values:		100k → 50k
	R_{47}			1k
	C_{46}	3.0 pF	6.0 pF	13 pF
$(CR)^2 \cdot (RC)^3$	C_{40}	100 pF	200 pF	390 pF
	R_{40}	5.1 M	2.4 M	1.3 M
	C_{41}	3.0 pF	6.0 pF	13 pF
	R_{42}	gain adjustment typical values:		5.1k
	R_{43}			0
	R_{44}	The attenuator must present 5.1k between the two terminals		∞
	C_{42}	100 pF	200 pF	390 pF
	C_{43}	3.0 pF	6.0 pF	13 pF
	R_{46}	gain adjustment typical values:		100k → 50k
	R_{47}			1k
	C_{46}	3.0 pF	6.0 pF	13 pF

block is similar to the model of the preamplifier, the main difference being a current input rather than a voltage input.

Resistor R_{39} from the preamp (Figure 5.3) is actually part of the R_{39}, R_{40}, C_{40} combination; it is included in the preamplifier in order to provide some short-circuit protection. The first CR corner is determined by $C_{40}R_{39}$. In addition, $R_{40}C_{40}$ provides zero cancellation for the zero introduced by R_f $(R_fC_f = R_{40}C_{40})$.

The RC terms are provided by $R_{41}C_{41}$, $R_{45}C_{53}$ and $R_{48}C_{46}$. The resistor combinations $R_{42}/R_{43}/R_{44}$ and R_{46}/R_{47} are included to set the amplifier gain. The first attenuator $R_{42}/R_{43}/R_{44}$ is used as the R for the second $C_{42}R$ if a bipolar pulse is desired. If attenuation is inserted at this point and bipolar pulse shaping is desired, the combination must present an impedance of 5.1 kΩ.

The **last** gain block is identical with the second gain block. Because of the high ac gain an attenuator is required at the input. Since R_{46} and R_{47} form a simple voltage divider and are not used in determining a desired pole or zero, it is more convenient to adjust the overall gain of the shaper at this point, rather than using $R_{42}/R_{43}/R_{44}$.

The capacitors in the feedback loops of the gain blocks introduce a phase shift at the operating frequencies. Capacitors C_4, C_8 and C_{11} are included to offset this phase shift.

The gain block operates with a common emitter input stage operating as a current input. The common emitter amplifier is followed by a common base amplifier; this stage provides the voltage gain of the gain block. The two together form a cascode amplifier. This is followed by an emitter follower, to provide a low output impedance.

The final gain block is followed by a unity gain amplifier, Q_{7a}. This amplifier provides inverting and non-inverting outputs. The polarity of the output pulse is jumper selected at this point. The output transistor, Q_{7b}, provides a voltage gain of 10. The last gain block was unable to provide the required voltage swing. The output impedance of the pulse shaper is undesirably high, the output stage was limited in size and power requirements and the configuration shown represents the best compromise available in the given time frame. The high output impedance of the shaper does not affect the operation of the unit when connected to the EPS pulse-height analyzer; but it does present problems when some low impedance test equipment or long

connecting cables are required.

Power into the shaper is filtered by feedthrough capacitors and the high gain stages are all de-coupled from the power supply (e.g., C_3 and R_9).

An output of -11 V peak for 130 keV energetic electrons incident on the detector with a $(CR) \cdot (RC)^3$, $\tau = 1$ μs filter characteristic was required. The gain resistors listed in Table 5.6 reflect this requirement.

It was noted earlier that the input impedance of the shaping circuit is much less than the resistance R_{39} (5.1 kΩ) at the output of the charge preamplifier. Looking at the shaping circuit (Figure 5.13) we find that R_{39} (the output resistor of the preamplifier) is connected in series with C_{40} and then to the base of Q_1 of the shaping circuit. The time constant $R_{39}C_{40}$ is chosen to be the τ. The operating frequency is considered to be $1/\tau$ (1 MHz throughout this circuit description); so at the frequency of operation the series pair $R_{39}C_{40}$ is primarily resistive. It is assumed here that the current feedback on Q_1 of the shaper reduces the input impedance of that transistor so that R_L for the preamplifier is the impedance of R_{39}, 5.1 kΩ.

6. TESTING AND CALIBRATION OF THE ENERGETIC PARTICLE SPECTROMETER

The testing and calibration are divided into three phases: 1) bench tests of the system components; 2) main calibration at NASA/GSFC; and 3) pre-flight calibration at the launch site. During the first phase the system components (i.e., detectors, linear electronics, and non-linear electronics) are tested individually. The tests performed on a given stage can be designed to provide more information about that stage than could be obtained if only the input and output relationships of the entire instrument were to be measured. Both individual components and the entire system are considered during the main calibration. The final (pre-flight) calibration is performed shortly before launch and only considers the system input/output relationships.

6.1 *Bench Tests of the System Components*

6.1.1 *The detectors*. Energetic particle spectrometers have been used on several previous flights, although these instruments have provided limited information when compared to the EPS experiments flown for JASPIC. Because of this experience several aspects of the detector and collimator have already been discussed in *Voss and Smith* [1974] including the effects of the collimator on the angular response of the detectors.

The other property of interest is the response of the detectors to particles of known energies. The primary factor here is the effect of the dead zone. A detailed discussion of the dead zone (based largely on empirical data) was presented in Section 3.4.1. The results of the theoretical calculations were compared with some experimental measurements. If the particles used in the measurements are treated as unknowns, proper identification is possible, although there is a greater deviation from the theoretical calculations than expected. To investigate this deviation, some additional experimental measurements have been made during the main calibration and the result compared with the theoretical calculations.

6.1.2 *The linear electronics*. The charge preamplifiers and the shaping amplifiers are mounted on a payload deck and are tested together. The two units are packaged in separate boxes in order to allow the preamplifiers to be mounted as close as possible to the detector, thus reducing the excess capacitance caused by long cables between the detector and the preamplifier. Separating the units also allows switching of detectors at a point where the performance of the system is not affected. In considering the response of

of the system to an energetic particle, only the output of the shaping
amplifier is measured.

Tests for amplifier gain, noise performance, and amplifier linearity
can be performed without specialized test equipment. The setup for bench
tests is shown in Figure 6.1. Here the signal is monitored at the output
of the shaping amplifier, providing maximum resolution.

A detector is connected to the preamplifier and a radioactive source is
used to provide a pulse height (voltage level) corresponding to a known
input energy. The detector is disconnected in order to reduce the capacitance
across the preamplifier input, thereby improving the resolution of the system.
Then the Ortec test generator is connected and the attenuators (including the
normalization control) are adjusted so that the test generator scale is
calibrated in terms of energy. For example, if an Am^{241} radioactive source
is used, the energy level of interest is 60 keV; the dial of the test genera-
tor is set to 60 and output level is adjusted with the attenuators until the
shaper output pulse is the same height when using the generator as with the
radioactive source.

Measurements of the output level are taken for various input levels.
These measurements indicate the gain of the amplifiers (in V/keV) and the
linearity of the amplifiers. After the gain of the system has been determined,
the noise performance is checked. The rms noise level at the output is
measured with various amounts of shunt input capacitance. The amplifier
produces a certain amount of noise without any shunt capacitance. As
additional shunt capacitance is added, the noise level increases linearly
(capacitance in addition to the stray shunt capacitance).

The results of this test for three different combinations of preamplifiers
and shapers are shown in Figure 6.2. The noise is indicated in terms of E_{fwhm}
(see Section 4.3.1). This figure of merit is calculated using

$$N = 2.66 \ v_n/K \tag{6.1}$$

where N is the full width at half maximum given in terms of keV, the rms
noise voltage (as read on an averaging meter) is represented by v_n, in mV,
and the gain of the system in V/MeV is represented by K. The factor 2.66 is
the factor 2.36 from the definition of FWHM (equation 4.5) multiplied by
1.11, which changes the reading obtained from the averaging voltmeter into
an rms value. Figure 6.2 is particularly useful in that it provides a
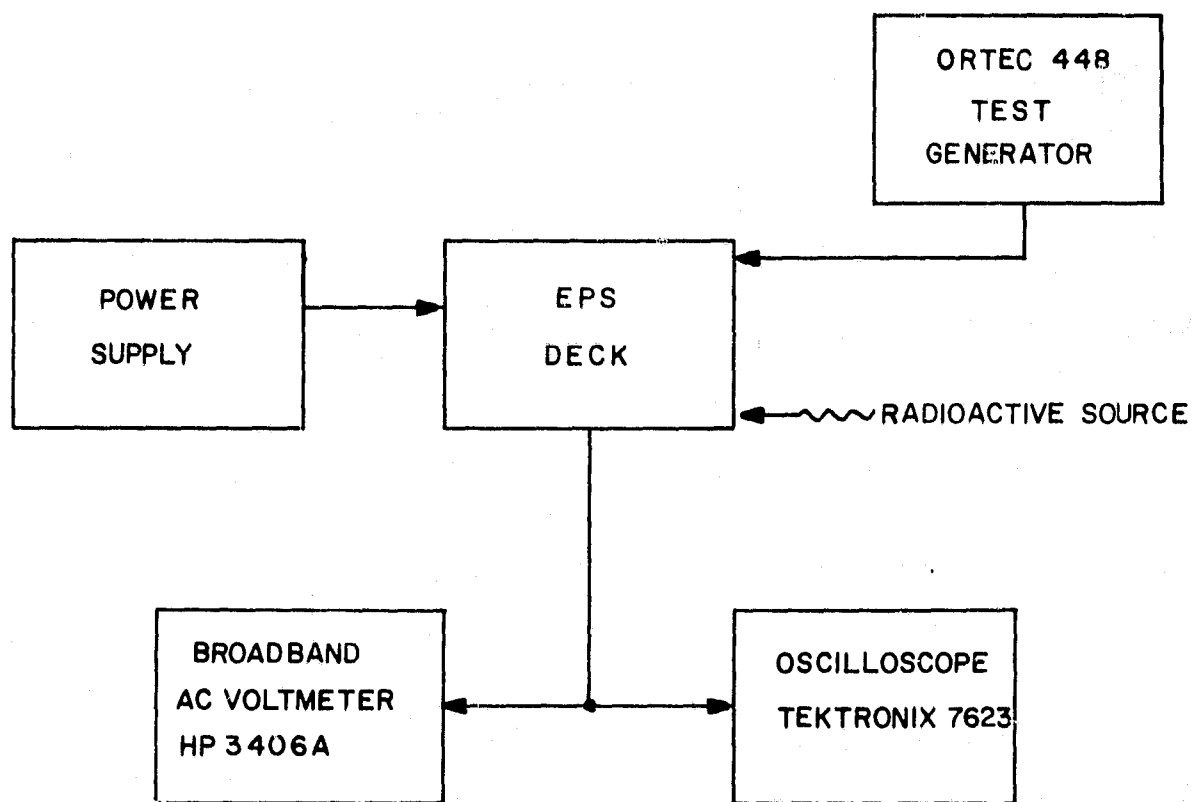
Figure 6.1 Test setup for bench measurements.
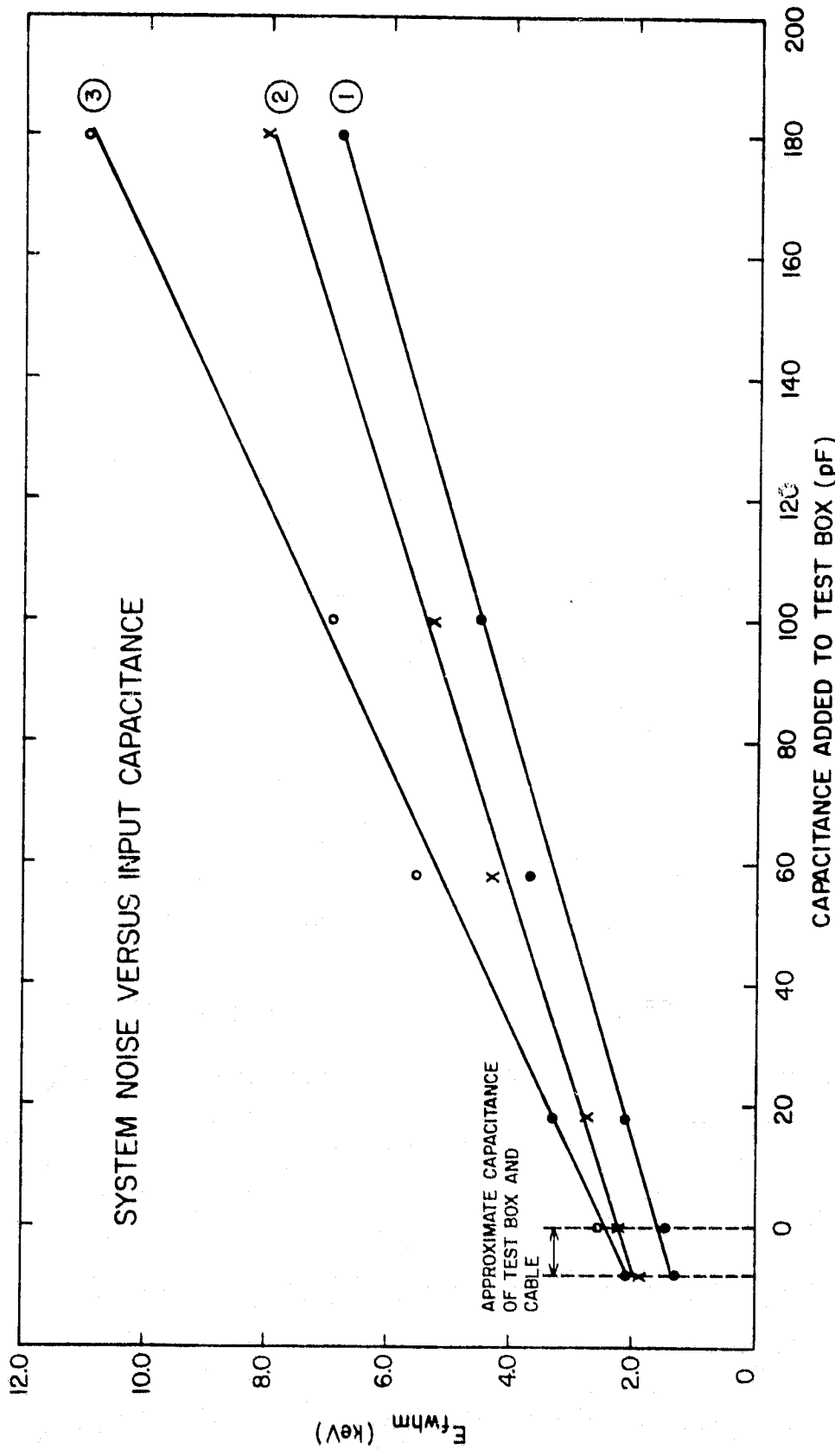
Figure 6.2 Results of tests on three preamplifiers. Curve 1 represents an SFB 8558 input transistor. Curves 2 and 3 are from preamplifiers with 2N6451 input transistors. $\tau = 2\mu s$ in all cases.

standard of comparison for future preamplifiers. If the noise performance of other amplifiers is much higher than those shown here, there is probably a defective component in the circuit. If the noise performance is much better for amplifiers of the same design, a measurement error should be suspected.

The data given in Figure 6.2 illustrate the effect of two different types of input transistor. The SFB 8558 is a special part obtained from Texas Instruments; the characteristics are similar to those of the 2N6451. The SFB 8558 results in improved noise performance, but it is more expensive and more difficult to obtain than is the 2N6451.

The curves also indicate the improvements in noise performance that can be obtained by selecting the highest performance parts from a given batch. The two 2N6451 FET's have comparable noise performance when no shunt capacitance is present, but the device used in preamp #5 (curve 3) is much more sensitive to shunt capacitance than either of the devices in preamps #0 and #4 (curves 1 and 2). When a detector is connected, the capacitance it presents will produce an increase in noise just as the capacitors used in the test box did.

6.1.3 *The non-linear electronics*. The microprocessor system is completely digital and does not require calibration. The rocket-borne pulse-height analyzer, however includes the peak detectors and the analog-to-digital converter; these must be calibrated.

PHA parameters of interest are the linearity and accuracy of the system. To properly calibrate this portion of the system the test pulse must have the same shape as the actual pulse encountered during flight. This is obtained by using a charge preamplifier/shaping amplifier combination with an Ortec test generator. These tests can be performed on the bench. The PHA tests are coupled with the results of the tests on the linear electronics in order to obtain a pre-calibration curve relating the output of the analog-to-digital converter to the input energy level.

6.2 *Main Calibration at NASA/GSFC*

After the bench tests are complete the EPS experiment is ready for the main calibration. At this point, the gain of the amplifiers has been adjusted and the input transistors selected. The detectors, preamplifiers and shapers are numbered and treated as systems. The main calibration is performed at NASA/Goddard Space Flight Center in Maryland. The test setup is shown in

Figure 6.3. The EPS experiment is placed in a vacuum chamber and tested
using energetic particles. Since we are primarily interested in the
linearity of the system electronics and the non-linearity of the dead zone
losses, a 256-channel pulse-height analyzer is used to monitor the output
signal instead of the 16-channel pulse-height analyzer used on the rocket.
The improved resolution allows more accurate calibration of the linear
system. The Ortec test generator and the radioactive source are included
for the tests indicated previously.

The high impedance output of the shaper presented some interface
problems. The pulse-height analyzer has a low impedance input and cannot be
connected directly to the EPS. An oscilloscope with a vertical channel
output was used to monitor the EPS signal and to drive the high resolution
pulse-height analyzer.

Long cable runs between the shaping amplifiers and the loading caused
by the two peak-detecting circuits (in the counting electronics and the
rocket-borne PHA) loaded down the output amplifier of the shaper, slightly
decreasing the gain of the system (by a factor of 10 or 20 percent). For
this reason the main calibration does not provide voltage levels
corresponding to energy levels; this information will be obtained later during
the pre-flight calibration. The main calibration provides a comparison
between the various channels and shows the effects of different particles on
the various detectors.

The pulse-height analyzer produces what can be considered a relative
probability distribution. Typical outputs are shown in Figures 6.4 to 6.9.
Points along the horizontal axis represent the various channels of the PHA
and correspond to narrow energy bands. The vertical axis represents the
number of counts obtained for a given channel (energy band); those counts
correspond to the values of the relative probability distribution function of
the signal (modeling the signal as a random process). The randomness is
due to the noise inherent in the system.

The relative probability distribution function indicates the likelihood
of a particle of a certain energy, in this case the energy level corresponding
to the center of a peak, being measured as a slightly different energy. If
enough samples are taken to provide good statistics, then the ratio of the
particle energy being measured at that given energy level, instead of being
measured at the actual energy level. In terms of the figure of merit being
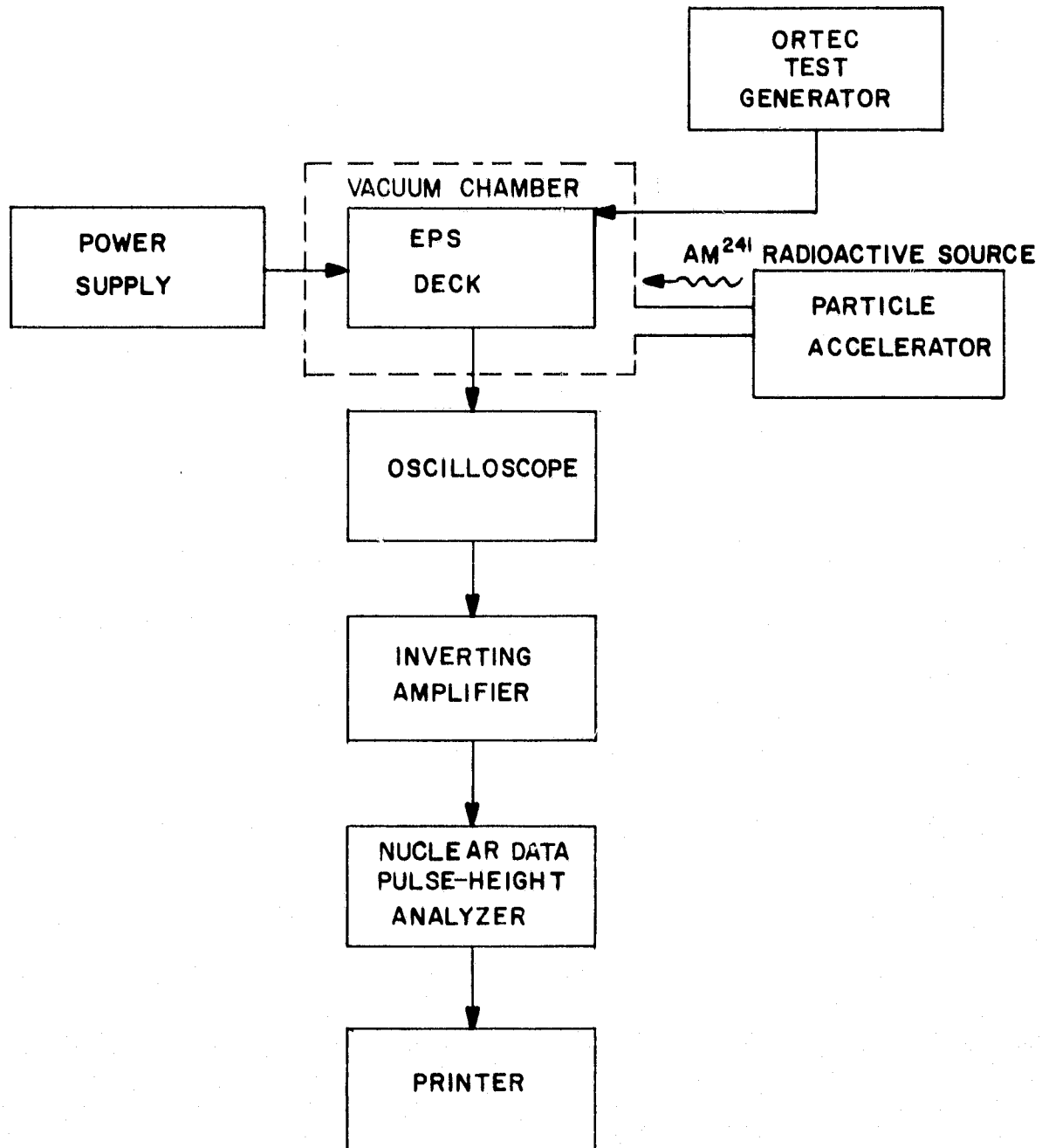
Figure 6.3   Test setup for EPS precalibration
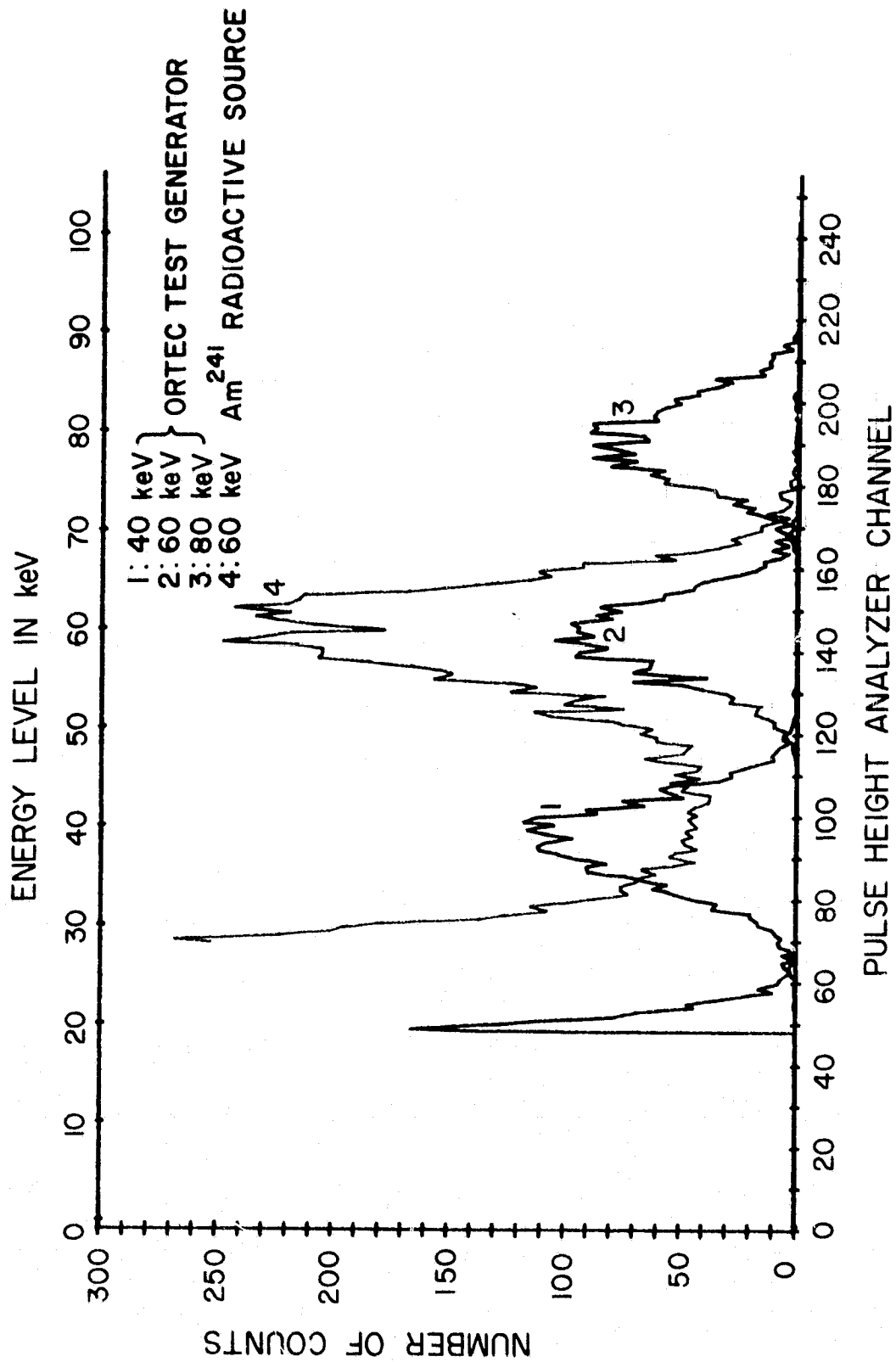
Figure 6.4 EPS intercalibration data for rocket 14.542 detector 1 up (40 μg cm^{-2} Au).
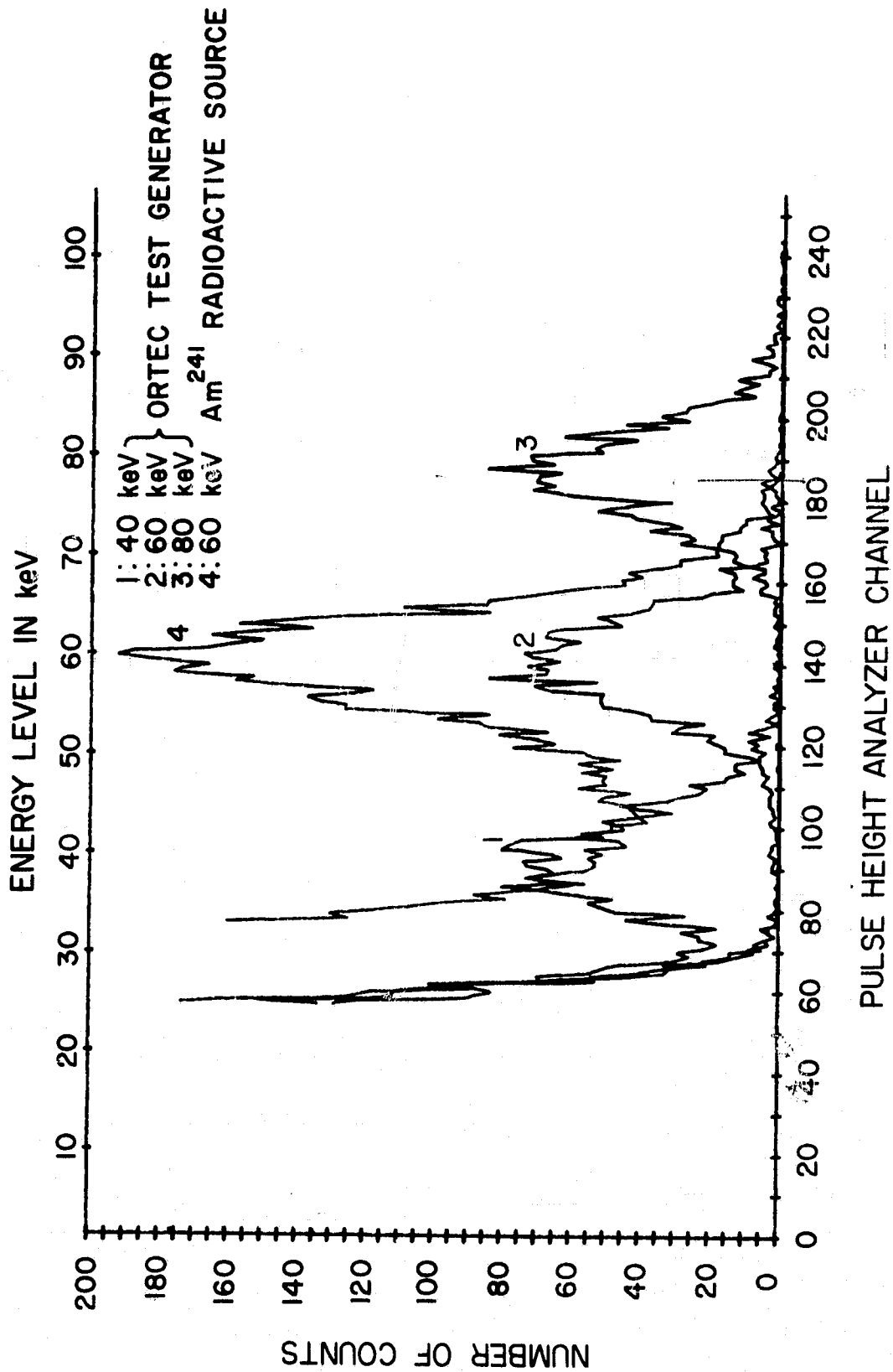
Figure 6.5 EPS intercalibration data for rocket 14542 detector
1 down (40 μg cm^{-2} Au).
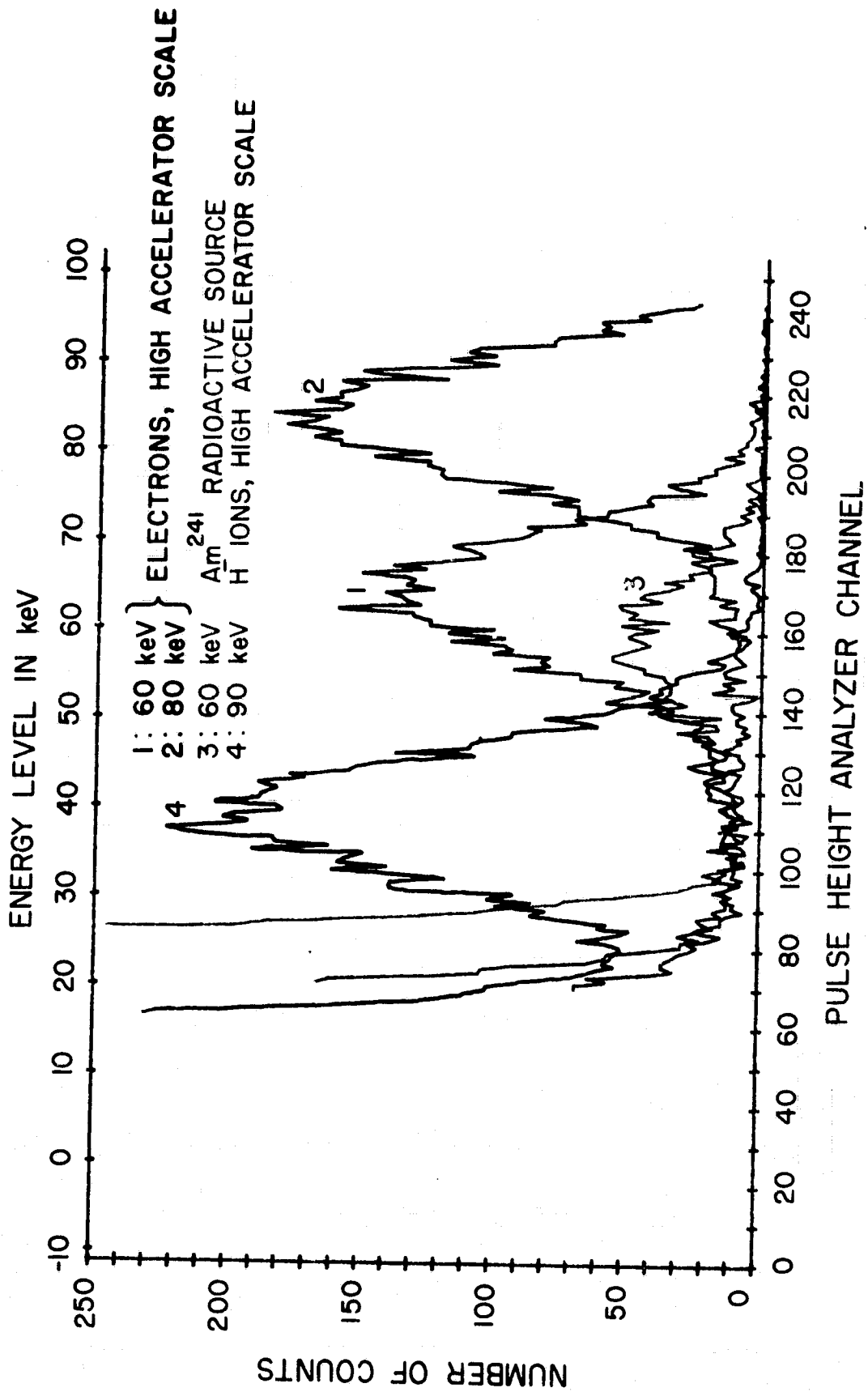
Figure 6.6 EPS intercalibration data for rocket 14.542 detector 2 up (100 μg cm⁻² Al).
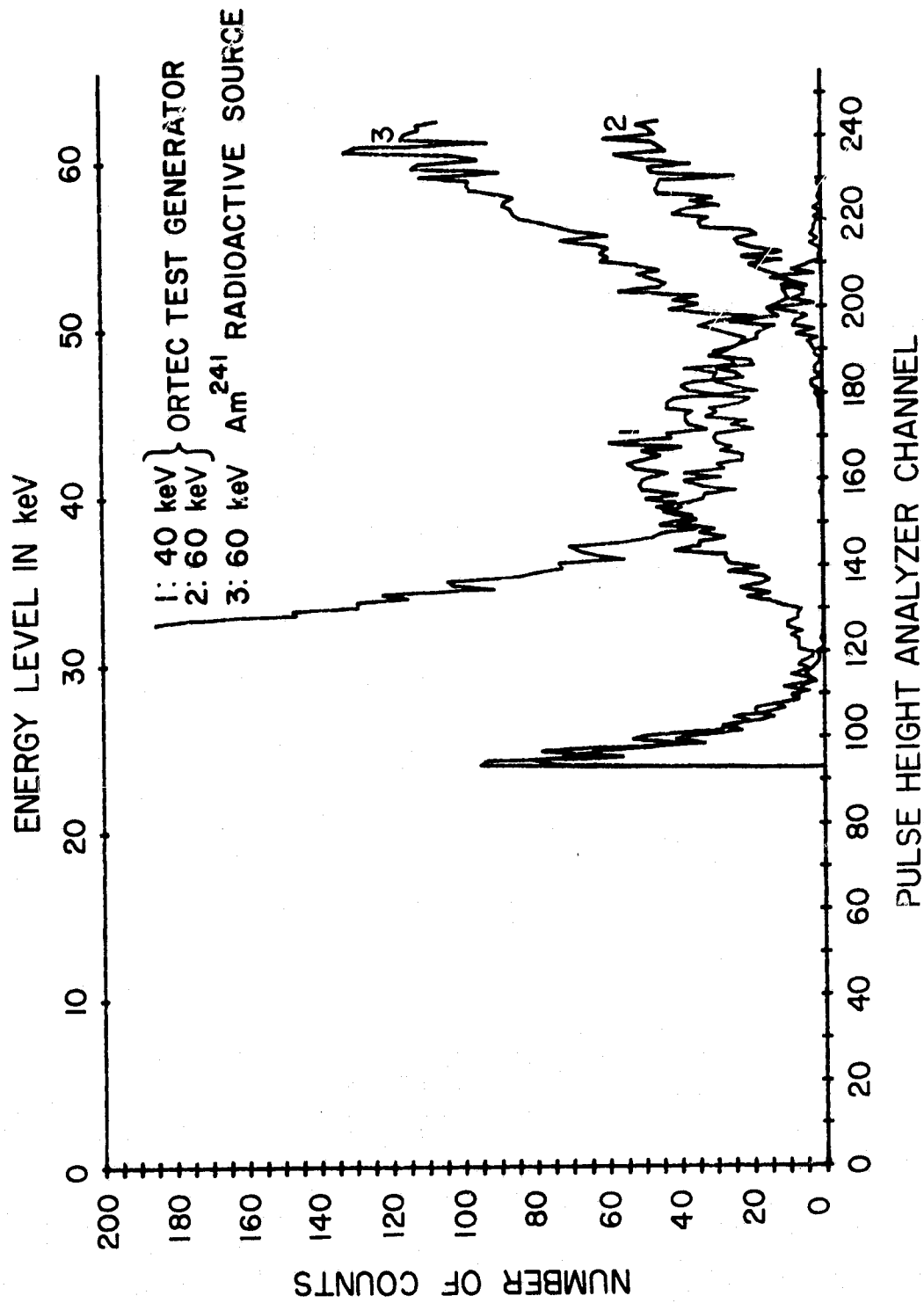
Figure 6.7 EPS intercalibration data for rocket 14.542 detector 3 up (40 μg cm^{-2} Al).
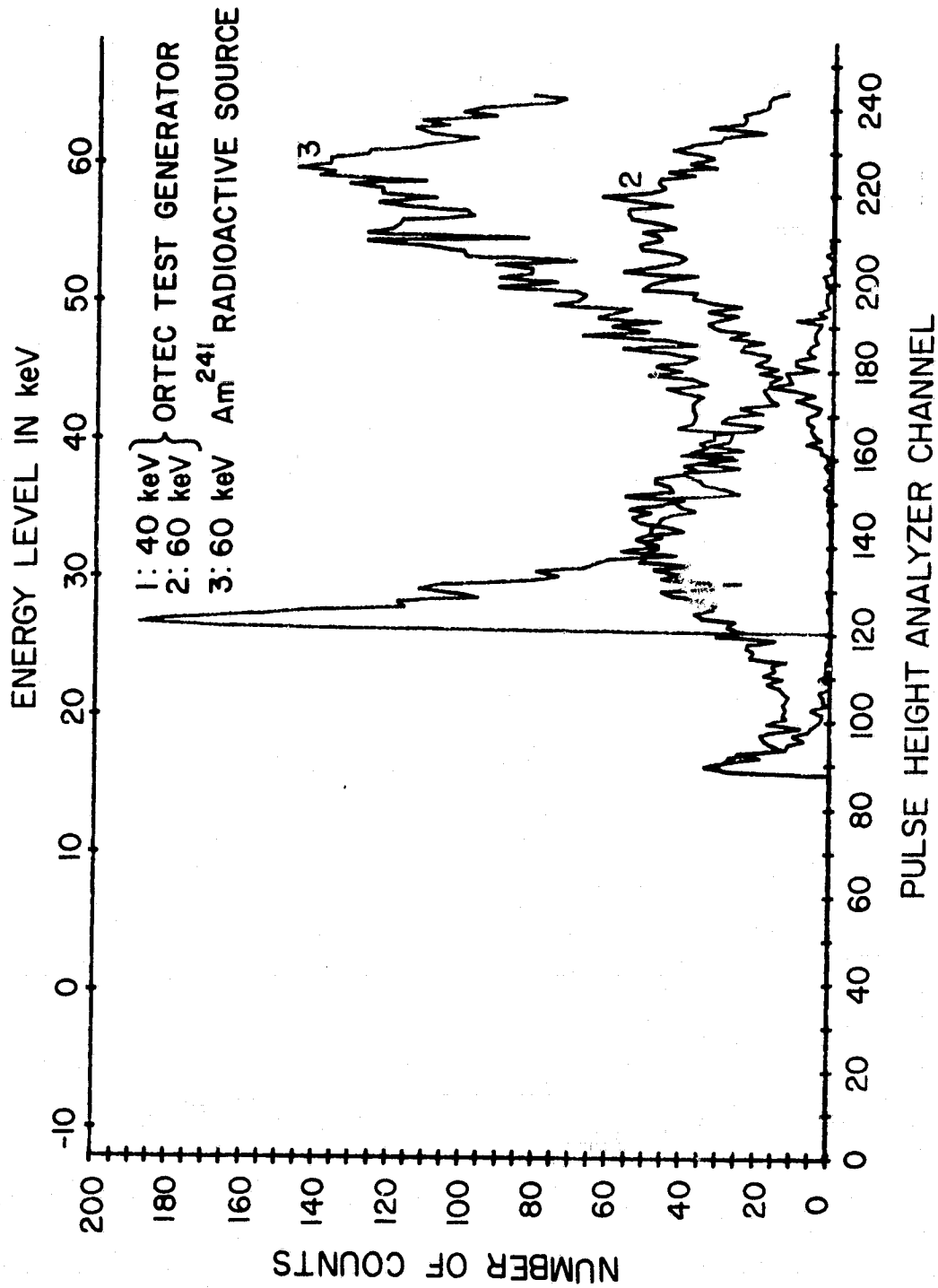
Figure 6.8 EPS intercalibration data for rocket 14.542 detector 3 down (40 µg cm^{-2} Al).
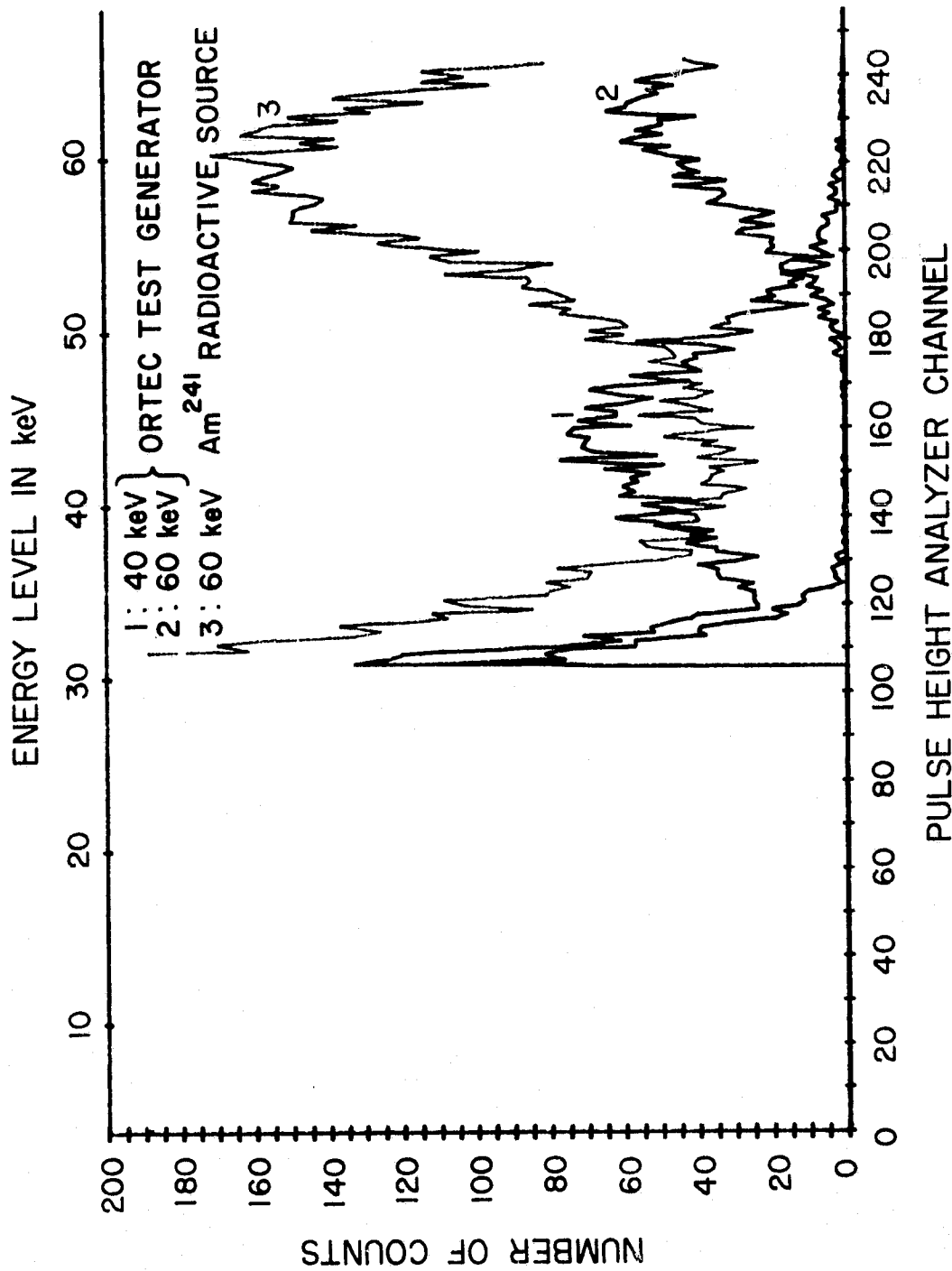
Figure 6.9   EPS intercalibration data for rocket 14.542 detector
4   (40 μg cm^{-2} Al).

used to describe this system the FWHM can be directly obtained from the plot by finding the number of channels between the two points on the curve with count rates half that measured at the peak. Consider the Am^{241} peak of Figure 6.5. The peak count rate is 193 counts for channel 142 (E = 60 keV). Half of this count rate is 97; this corresponds to channel 126 (E = 54 keV). and channel 153 (E = 64 keV). So $E_{fwhm} \approx 10$ keV for this channel. A change in the gain of the system will not affect E_{fwhm}; however, a change in the temperature of the detector, or the level of contamination, will have an effect.

When working with the data obtained during the main calibration, it is often useful to plot several different curves on the same set of axes. This allows one to see the effects of the dead zone on different types of particles, and to check the linearity of the system. A listing of the computer program written to plot these data are given in Appendix I, along with a short description of the program.

The plots in Figures 6.4 through 6.9 are included to provide intercalibration data for the six EPS's on Nike Apache 14.542, to model typical plots, and to demonstrate the difference in response of the different detectors to the various types of particles. (Chapter 3 contains some additional plots of response to energetic particles.) The scale at the top of each plot is the energy scale for that particular detector. This is obtained by centering the 60 keV point at the peak resulting from the Am^{241} radioactive source. The Ortec test generator provides pulses that are approximately 20 keV apart; the distance between these peaks is used to determine the number of channels per keV for a given detector. The normalization of the Ortec generator is not exact; this implies that the energy read off the Ortec scale should be multiplied by a constant factor in order to obtain the correct equivalent energy.

An iterative process is used to obtain a better approximation to the energy of the Ortec generator. The following quantities are defined:

α   is the scale factor for the Ortec generator: multiplying the energy on the Ortec dial by α produces the correct equivalent energy;

ΔE is the number of PHA channels per keV;

Ch_0 is the channel number of the peak produced by the Ortec generator at the setting E_0;

Ch_{ref} is the channel number of the peak produced by the
radioactive source corresponding to the energy E_{ref}
α' and $\Delta E'$ are the approximations to the values of α and ΔE,
defined above.

The procedure is as follows:

1) Obtain Ch_0, E_0, Ch_{ref}, E_{ref}, and $\Delta E'$ from plot (two Ortec
peaks are used to obtain $\Delta E'$). Assume $\alpha' = 1$. Set
$\Delta E'_{original} = \Delta E'$.

2) Calculate new $\Delta E' = \alpha' \Delta E_{original}$.

3) Calculate new α'

$$\alpha' = \frac{(Ch_0 - Ch_{ref})}{\Delta E'} + E_{ref}/E_0$$

4) Check difference between $\Delta E'$ obtained on this iteration and
$\Delta E'$ obtained on last iteration. If the four most significant
digits agree stop; if not, go to 1.

The channel numbers corresponding to the peaks of the various plots
along with α' and $\Delta E'$ are collected in Table 6.1. Because of variations in
the attenuation of the test input (due to component tolarances) α' can be
different for each detector system. Intercalibration for detector 2 up
used accelerator measurements, so $\alpha = 1.00$.

The energies listed for the various peaks at the top of each plot are
approximate. The actual energies are listed in Table 6.2; the discrepancies
are due to the Ortec calibration factor discussed above, and due to errors
in the calibration of the particle accelerator (Section 3.4.2).

6.3 *Pre-Flight Calibration at the Launch Site*

Before launch the detectors are checked with a radioactive source. The
output of the system is recorded on the telemetry tape for later reference.
This provides information regarding any changes in gain or noise performance
due to changes in temperature or to contamination of the detectors. These
final checks, coupled with the detailed analysis of linearity and PHA response
allow accurate calibration.

Figure 6.10 contains four sections of the pre-flight calibration chart
record. The horizontal axis is the energy level (bin numbers), and the
vertical axis is the number of counts. By adding the number of counts in a
given bin from several different measurement periods it is possible to get
good statistics.

Table 6.1

Values used for determining energy
scales on intercalibration plots.

Detector	Location of Energy Peaks (channel #'s)				α'	$\Delta E'$ (ch/keV)
	Am^{241} 60 keV	40 keV	60 keV	80 keV		
1 up	145	95	144	191	.993	2.38
1 down	142	92	141	188	1.00	2.42
2 up	160	-	electrons (high scale) 170 · · · · · · · 215		-	2.25
3 up	234	164	240	-	1.03	3.90
3 down	227	145	213	-	.926	3.15
4	221	157	232	-	1.05	3.93

Table 6.2

Actual energies used during intercalibration

Detector	40 keV Ortec (keV)	60 keV Ortec (keV)	80 keV Ortec (keV)	60 keV Electrons (keV)	80 keV Electrons (keV)	90 keV H⁻ (keV)
1 up	39.7	59.5	79.4	-	-	-
1 down	40	60	80	-	-	-
2 up	-	-	-	64.4	84.4	94.4
3 up	41.2	61.8	-	-	-	-
3 down	37.0	55.5	-	-	-	-
4	42.0	63.0	-	-	-	-
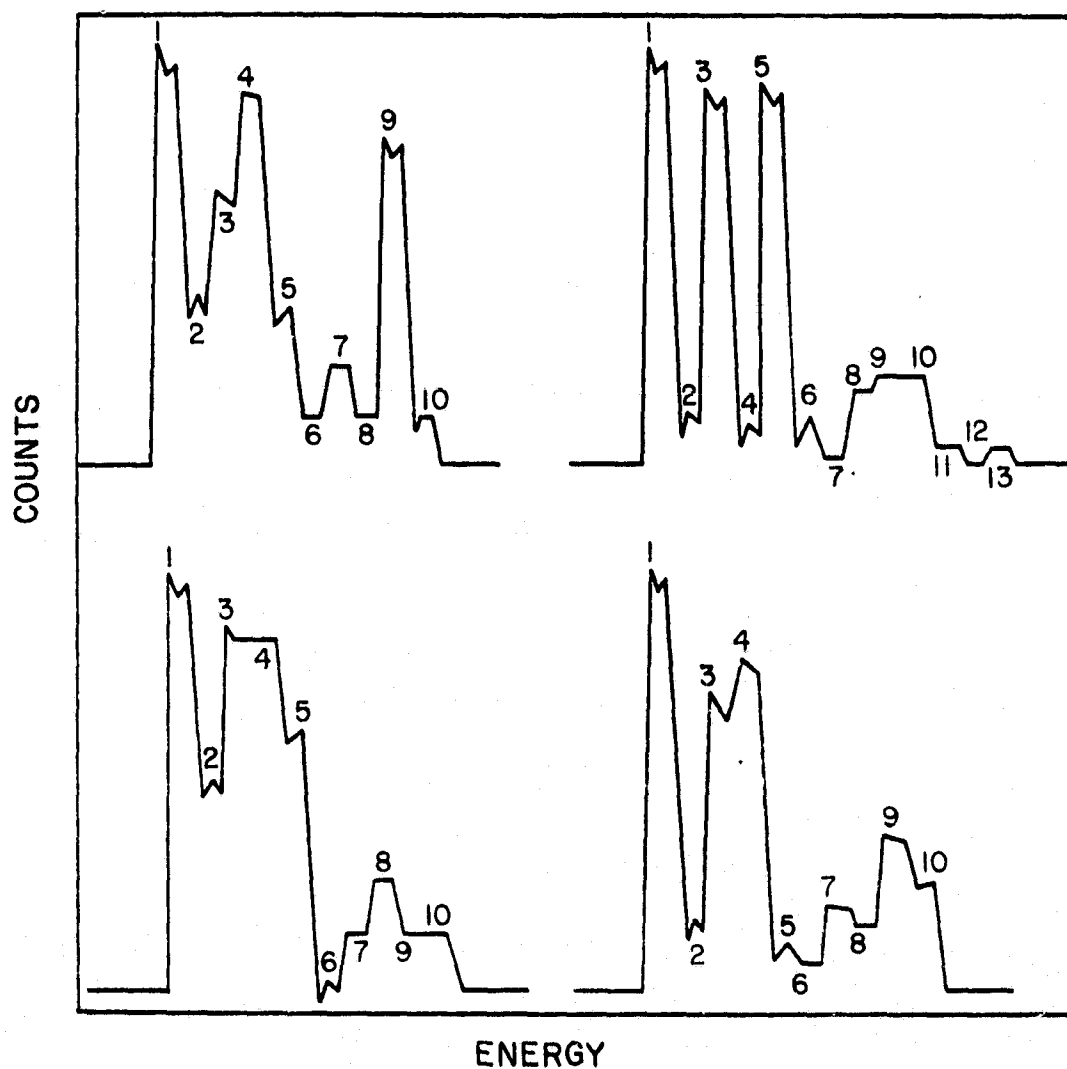
Figure 6.10 Portions of the chart record for the pre-flight
calibration of a detector using a 60 keV Am^{24}
radioactive source. The numbers identify energy
bins.

The chart record also provides the sample-and-hold output from the multiplexer; calibration can also be performed at this point. The analog output provides good resolution. The linearity of the A/D-D/A system of the microprocessor allows calibration of the energy bins with the information obtained from the sample-and-hold.

7. FLIGHT DATA

7.1 *Introduction*

This section will discuss some of the results obtained from Nike Apache 14.542 during the JASPIC program. The significance of the results, as they demonstrate the capabilities of the instrument, will be noted.

This is preliminary data. Exact energy levels for the various bins of the microprocessor and for the thresholds of the counting electronics will be determined later. Only relative energy levels are, at present, available; particle identification and spectrum profiles can, however, be determined. The pre-flight identification and spectrum profiles are obtained.

The launch occurred at 0530 UT (0030 EST) on September 27, 1978. The global weighted average of magnetic activity index, Kp, was 5+ for the three-hour period including the launch and 6- for the preceding three-hour period. Conditions at the time of launch allowed coordinated satellite and ground-based measurements.

7.2 *Count-Rate Versus Altitude*

Data taken by the microprocessor is sorted according to energy level, altitude, and rocket azimuth. If one is interested in the general trend of count rate (i.e., particle flux) with altitude, the counting electronics from the old system provides this information directly. Unlike the microprocessor, the counting electronics simply indicate the number of particles with energies greater than a certain threshold.

The thresholds of the counting electronics in Nike Apache 14.542 were set as follows: EPS 1: 2.70 V; EPS 2: 2.70 V; EPS 3: 2.63 V; EPS 4-1: 1.90 V; EPS 4-2: 2.70 V; and EPS 4-3: 4.7 V. Recall that the counting electronics for channel number 4 used three thresholds, as compared to one threshold for the other channels (see Section 2.6).

Figure 7.1 shows the count-rate profiles of the three energy levels for detector 4. This plot indicates a decreasing particle flux as energy increases. Figure 7.2 shows count-rate profiles for all of the detectors (EPS 4-2 is plotted for channel 4). The voltage thresholds are the same for all of these plots, but because of differences in amplifier gains the energies corresponding to the thresholds are slightly different. The low count rates obtained from EPS 3 down (mounted at 135° relative to the rocket spin axis) indicate that little backscattering of particles occurs. Much of the structure seen in the plot is due to the precessional motion of the
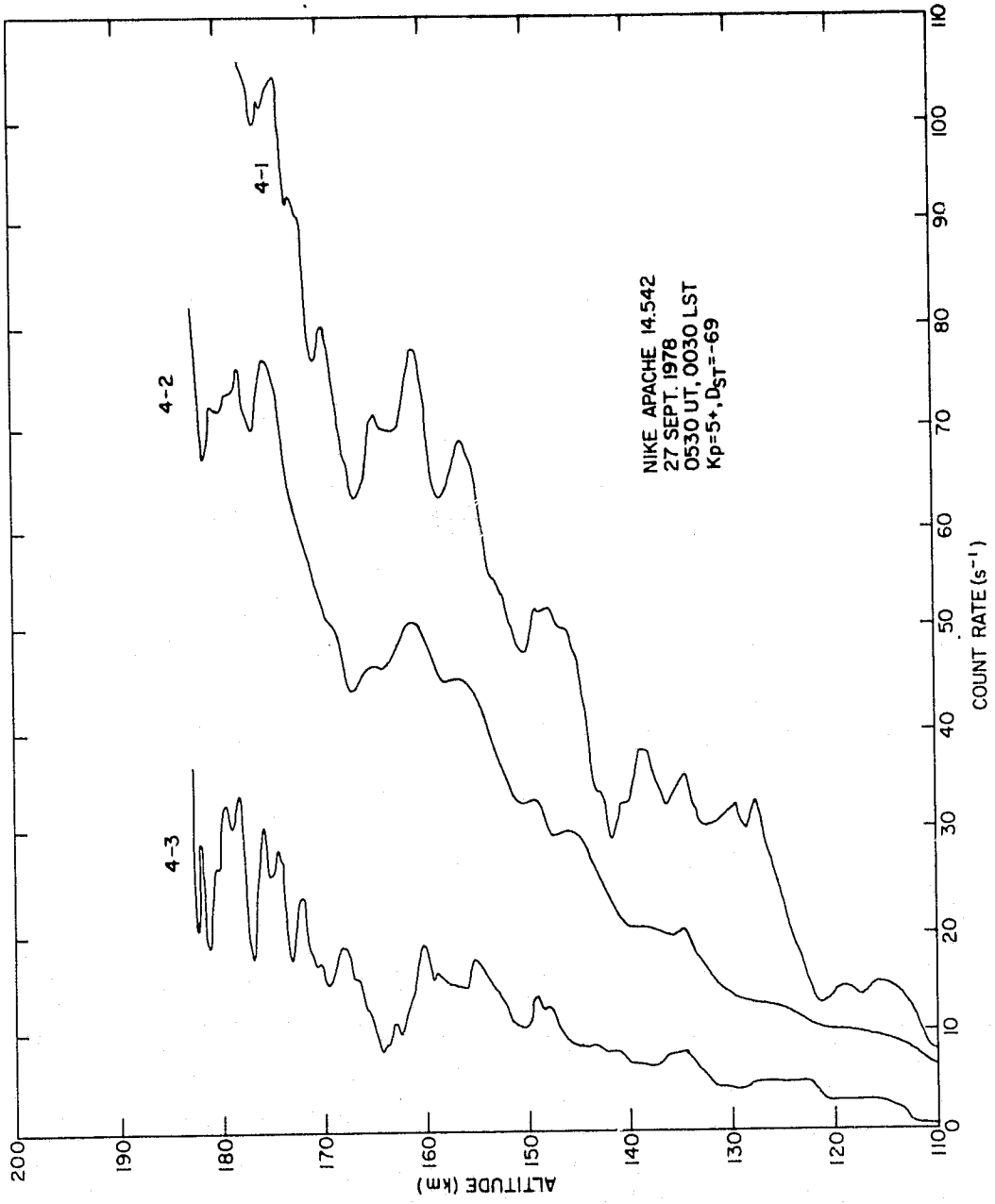
Figure 7.1 Count-rate profiles from three energy channels of detector EPS 4 on Nike Apache 14.542.
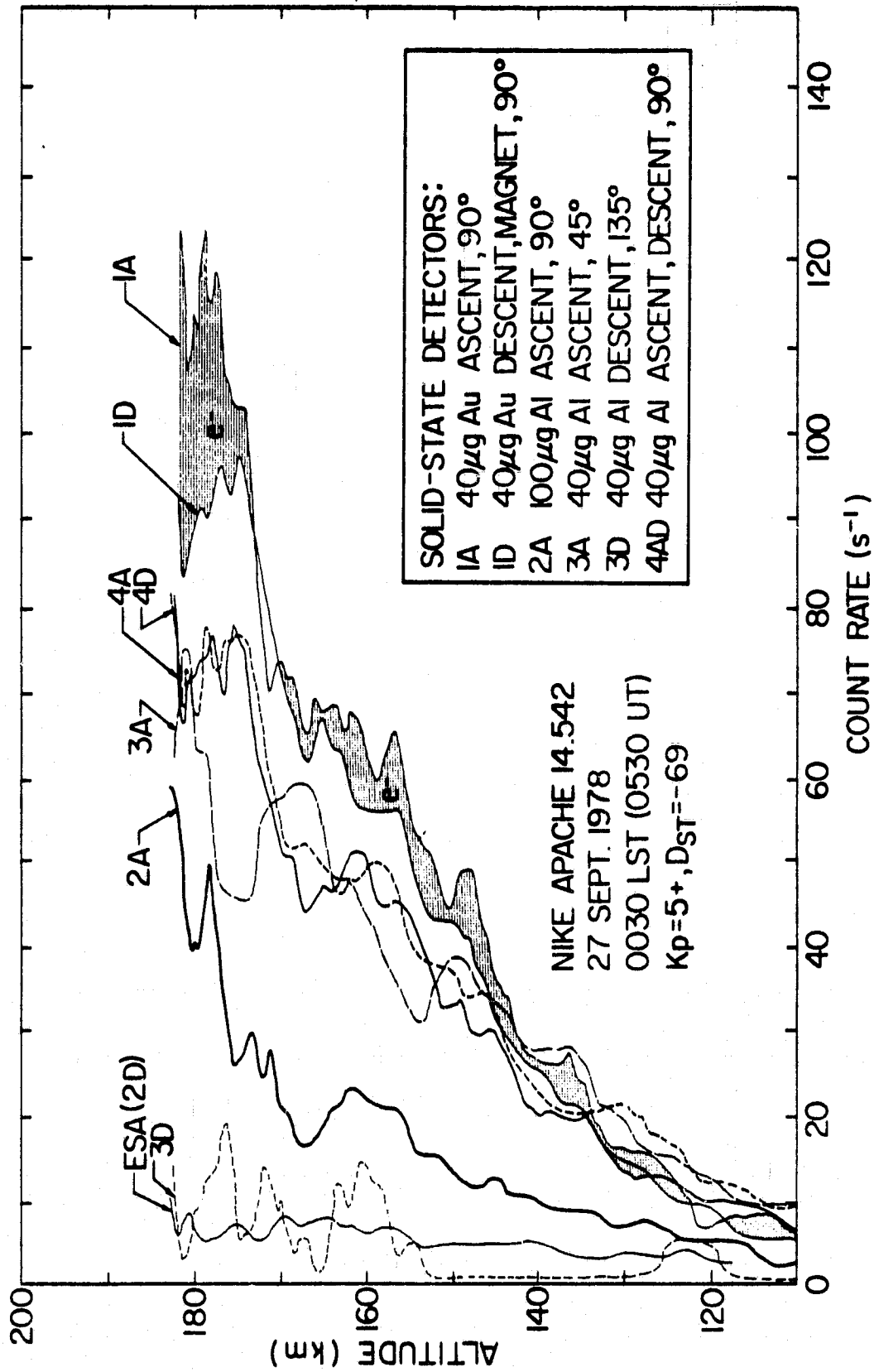
Figure 7.2 Count-rate profiles for six of the solid-state detectors on Nike Apache 14.542.

rocket which changes the look angle of the detector. The shaded area of the plot indicates the difference in count rate between two 40 μg cm^{-2} Au detectors, one with and one without a broom magnet (which prevent electrons from being detected). The results here indicate that the majority of the energetic particles are not electrons.

The more detailed energy spectrums and pitch-angle information obtained from the microprocessor is considered in the following sections.

7.3 *Pitch-Angle Distribution*

The microprocessor keeps track of the number of counts obtained at a given rocket azimuth; this is illustrated in Figure 7.3. In this plot all of the counts measured in energy bins 5 through 15 (1 through 4 are not included as that noise would influence the measurement) are shown as a function of rocket azimuth. The rocket azimuth is plotted according to bin numbers. This scale is linear so that each bin is a 24° increment from 0 to 360°. This plot contains data from two rocket revolutions in order to obtain better statistics. When this information is subsequently coupled with the direction of the rocket spin axis, accurate particle pitch angles can be determined.

The phase shift between detector 3 UP and detectors 1 up and 4 up is expected because of the location of the detectors in the rocket. Figure 7.4 identifies the positions of the various detectors; it can be seen that detector 3 up is mounted with its axis at 45° from the rocket spin axis.

7.4 *Energy Spectra and Particle Identification*

A plot of energy spectra is presented in Figure 7.5. In this plot the counts in each azimuth bin have been accumulated for two revolutions of the rocket. The energy scale is linear with an energy range of each bin of roughly 60/9 keV. Thus, bin 1 is the energy range 0 to 6.7 keV; this provides a relative energy scale.

Computer programs have been written by Frank Braswell to produce plots similar to those shown in Figures 7.3 and 7.5 by taking measurements over any given number of revolutions, including any given number of energy bins or azimuth sectors, at any time during the launch. Final results obtained from this analysis including particle identification, will be presented in a later publication.
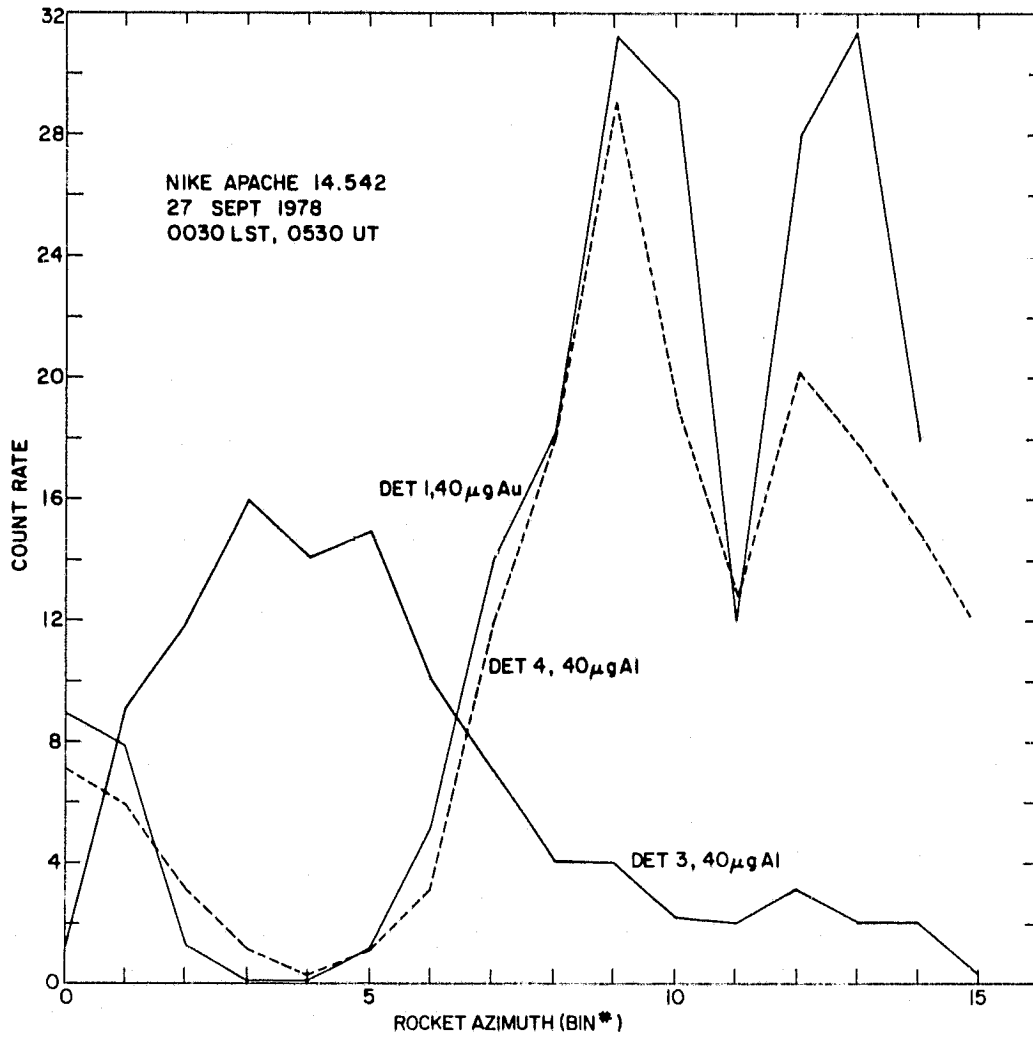
Figure 7.3   Azimuthal distribution of count rate from three of the solid-state spectrometers on Nike Apache 14.542.

2 UP
100 µg
cm^{-2} Al
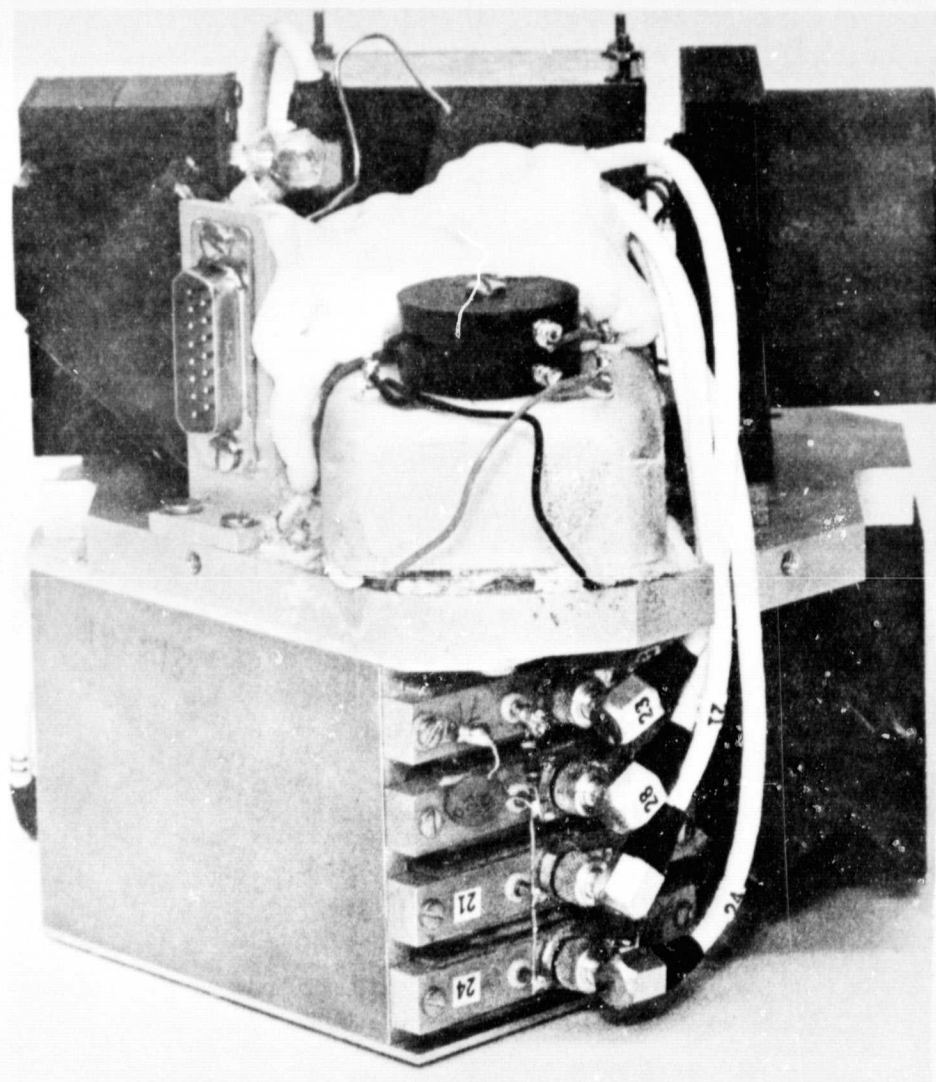
1 DOWN
(with
magnet)
40 µg
cm^{-2} Au

3 DOWN
40 µg
cm^{-2} Au
(40 µg
cm^{-2} Al)

4 UP/DOWN
40 µg
cm^{-2} Al

3 UP
40 µg
cm^{-2} Au
(40 µg
cm^{-2} Al)

1 UP
40 µg
cm^{-2} Au

Figure 7.4   Location of the detectors on the EPS deck of
Nike Apache 14.543 (parentheses indicate 14.542
when differences occur).
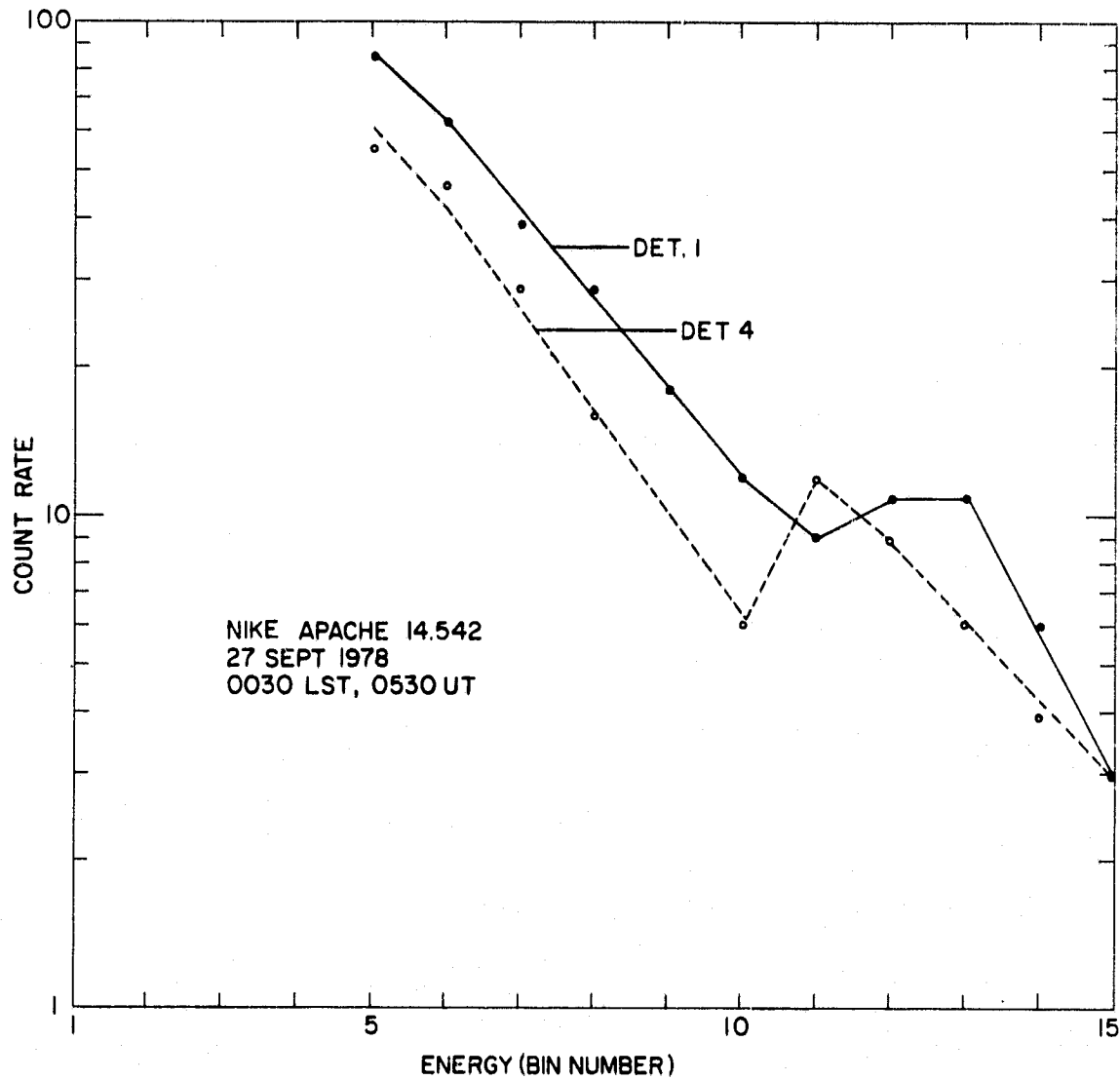
Figure 7.5 Energy spectra for two detectors on Nike Apache 14.542.
            The energy scale is linear with bin #9 corresponding to
            60 keV electrons.

8. CONCLUSIONS AND RECOMMENDATIONS FOR FUTURE WORK

8.1 *Conclusions*

This report has discussed the general requirements of an energy
spectrometer and, in detail, the theoretical and practical considerations
relating to the design of the linear electronics (low-noise charge
preamplifier and shaping amplifier). The performance of the unit has been
measured and reported. The preliminary results from Nike Apache 14.542 have
been presented.

8.2 *Recommendations for Future Work*

8.2.1 *The preamplifier.* The electrical performance of the present
preamplifier is acceptable. If the unit was repackaged, a slight decrease
in size could be realized. Any design change must minimize the possibility
of ground loops, yet provide very good shielding.

If the preamplifier circuit is redesigned, the paralleling of input
FET's should be considered. This results in a decreased slope for the noise
outputs versus input capacitance function. This has been investigated by
Smith et al. [1966] and the results of paralleled FET's at room temperature
and at 140°K are shown in Figure 8.1. Their preamplifier circuit is shown
in Figure 8.2. When n FET's are combined in parallel $g_{m_{eff}} = ng_m$ and
$C_{gs_{eff}} = nC_{gs}$. When low values of shunt capacitance are used, the nC_{gs}
factor results in a higher level of noise than would be obtained with a single
FET; however, when the shunt capacitance becomes large, the increased g_m
reduces the noise when compared with a single FET.

It was shown in Section 5.2.2 that the loop gain of the preamplifier
could become marginal ($T \approx 5$) if an input FET was chosen with a high value
of y_{ob5}. This occurs even though the open loop gain is quite high, because
of the large attenuation of the feedback signal. If the stage driven by
Q_2 (see Figure 5.3) had a high input impedance, Q_1 would act as an
appreciable voltage gain at the first stage. The frequency response of the
configuration must be investigated in order to determine if it is practical.
Because of the very short rise time of the input pulse, it is desirable to
have a charge preamplifier with a wide bandwidth. In the present configuration
the low impedance presented by the common base stage, Q_3, reduces the Miller
capacitance seen at the input of Q_1.

A single supply voltage should also be considered if the preamplifier is
redesigned.
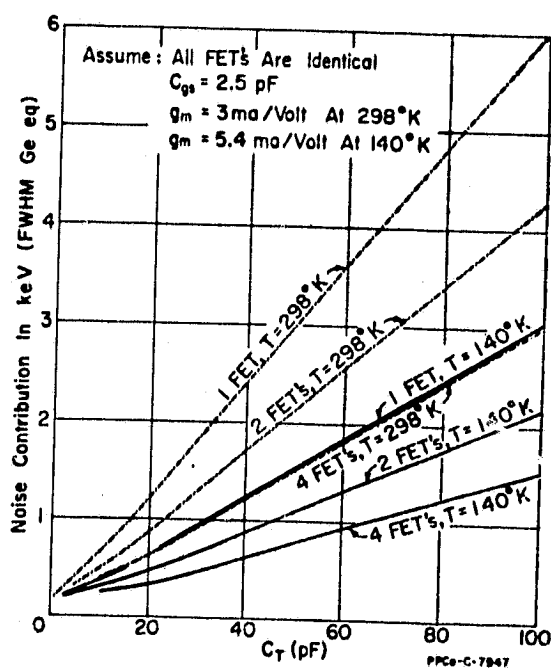
Figure 8.1 Theoretical amplifier noise vs C_{Total} for 1, 2, and 4 paralleled field-effect-transistors at T = 298°K and 140°K with τ_o = 1.6 μsec and single RC integrating and differentiating time constants [*Smith and Cline*, 1966].
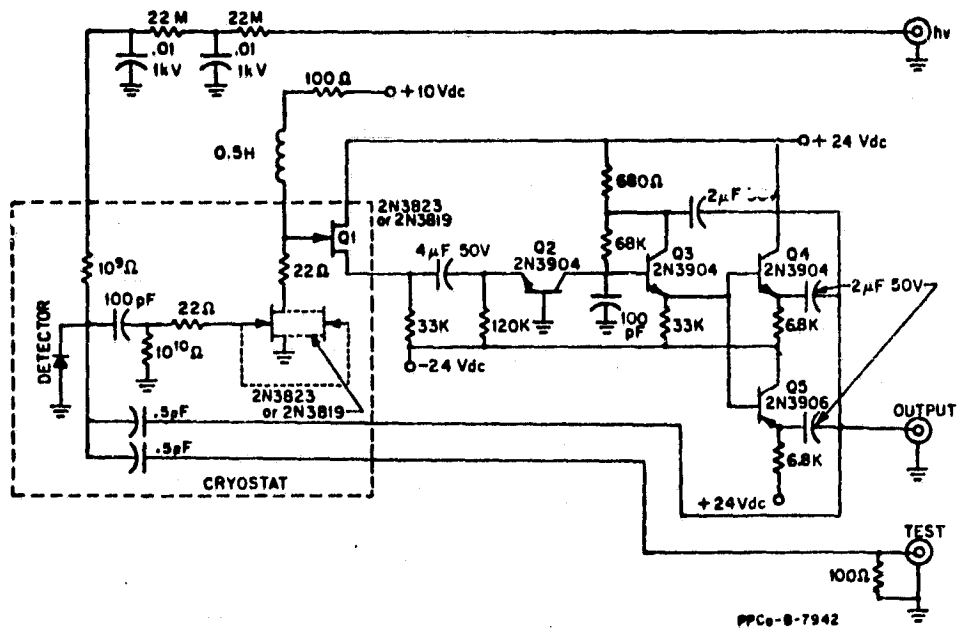
Figure 8.2   Schematic diagram of preamplifier using parallel
             input FETs [*Smith and Cline*, 1966].

8.2.2 *The shaping circuit.* The present shaping amplifier is large and uses some parts that are difficult to obtain. It should be possible to redesign the shaper using integrated operational amplifiers (op amps) and readily available components.

A fourth stage of low-pass filtering could be added to improve noise performance. The signal amplitude at intermediate points must be considered in any redesign. The frequency response of the devices should be high enough to insure proper operation of the filters; this may be difficult for the first stage. The shaping amplifier requirements were discussed in detail in Chapter 5. These requirements can be used as guidelines for a new design.

The output amplifier should be modified to provide a low output impeda impedance; this will simplify testing and insure proper operation in case changes are made to the following stages.

The analog switch functions well. Unless a smaller unit can be found, there is little reason to change design.

8.2.3 *General comments.* The present design represents what is felt to be the best approach for rocket-borne applications. If size and performance characteristics change in the future, a more elaborate design may be appropriate. Some things to consider would be:

a) A circuit that will discharge the feedback capacitor in the charge preamplifier after a certain amount of charge has been stored. This would replace R_f and eliminate the unwanted zero and the constant exponential decay of signal pulses.

b) A circuit that would monitor the time between pulses and indicate when pile-up has occurred.

c) The use of delay lines in the shaping filter. This would require an investigation to determine the practicality of using delay lines. If it is possible, the realizable optimal filter can be more closely approximated.

At the present time the above suggestions seem suitable for laboratory instruments, but not for rocket-borne applications.

The data obtained during pre-calibration for the JASPIC payloads was only available in printed form. This required entering 13,000 numbers by hand in order to plot the data in a usable form. The PHA data obtained from the pre-calibration should be written to digital cassette (in a format that can be used at the University of Illinois) or written to paper tape.

REFERENCES

Bertolaccini, M., C. Bussolati, and E. Gatti [1966], On the problem of optimum signal-to-noise ratio in amplitude measurements, *Nuclear Instruments and Methods, 41,* 173.

Bertolaccini, M., C. Bussolati, S. Cova, I. DeLotto, and E. Gatti [1969], Optimization of signal-to-noise ratio in the presence of noise and pileup fluctuations, Semiconductor Nuclear-Particle Detectors and Circuits, U.S. National Academy of Sciences, *Nuclear Science Series Report No. 44,* 523.

Bertolini, G. and A. Coche [1968], *Semiconductor Detectors,* New York: John Wiley and Sons.

Buck, T. M. [1961], Surface effects on silicon particle detectors, semiconductor nuclear particle detectors, *NASA-NRC-PUB. 876,* 111-120.

Carroll, J. E. [1974], *Physical Models for Semiconductor Devices,* Edward Arnold Publ. Co.

Davis, L. L., L. G. Smith, and H. D. Voss [1979], A rocket-borne data manipulation experiment using a microprocessor, *Aeron. Rep. No. 84,* Aeron. Lab., Dep. Elec. Eng., Univ. Ill., Urbana.

Deme, S. [1971], *Semiconductor Detectors for Nuclear Radiation Measurement,* New York: John Wiley and Sons.

Goulding, F. S. [1972], Pulse-shaping in low-noise nuclear amplifiers: a physical approach to noise analysis, *Nuclear Instruments and Methods, 100,* 493-504.

Herbst, L. J. (ed.) [1970], *Electronics for Nuclear Particle Analysis,* Oxford University Press, London.

Hunter, L. P. [1962], *Handbook of Semiconductor Electronics,* New York: McGraw-Hill.

Leung, W., L. G. Smith, and H. D. Voss [1979], A rocket-borne pulse-height analyzer for energetic particle measurements, *Aeron. Rep. No. 83,* Aeron. Lab., Dep. Elec. Eng., Univ. Ill., Urbana.

Milnes, A. G., and D. L. Feucht [1972], *Heterojunctions and Metal-Semiconductor Junctions,* New York: Academic Press.

Motchenbacher, C. D. and F. C. Fitchen [1973], *Low-Noise Electronic Design,* New York: John Wiley and Sons.

Nicholson, P. W. [1974], *Nuclear Electronics,* London: John Wiley and Sons.

Northcliffe, L. C. and R. F. Schilling [1970], Range and stopping-power tables from heavy ions, *Nuclear Data, A7, 233-463.*

O'Kelley, G. D. [1962], *Detection and Measurement of Nuclear Radiation,* Subcommittee on Radio-Chemistry, National Academy of Sciences, National Research Council.

Papoulis, A. [1965], *Probability, Random Variables, and Stochastic Processes,* New York: McGraw-Hill.

Pozzi, M. A., L. G. Smith, and H. D. Voss [1979], A rocket-borne electrostatic analyzer for measurement of energetic particle flux, *Aeron. Rep. No. 82,* Aeron. Lab., Dep. Elec. Eng., Univ. Ill., Urbana.

Smith, K. F. and J. E. Cline [1966], A low-noise charge-sensitive preamplifier for semiconductor detectors using paralleled field-effect transistors, *IEEE Trans. Nuc. Sci., NS-13.*

Sternheimer, R. M. [1959], Range-energy relations for protons in Be, C, Al, Cu, Pb, and Air, *Phys. Rev., 115,* 137-142.

Taub, H. and D. Schilling [1971], *Principles of Communication Systems,* New York: McGraw-Hill.

Voss, H. D. and L. G. Smith [1974], Design and calibration of a rocket-borne electron spectrometer for investigation of particle ionization in the nighttime and midlatitude E region, *Aeron. Rep. No. 62,* Aeron. Lab., Dep. Elec. Eng., Univ. Ill., Urbana.

Voss, H. D. and L. G. Smith [1977], Energetic particles and ionization in the nighttime middle and low latitude ionosphere, *Aeron. Rep. No. 78,* Aeron. Lab., Dep. Elec. Eng., Univ. Ill., Urbana.

Williamson, C. and J. P. Boujot [1962], Range and rate of energy loss of charged particles of energy 0.5 to 150 meV, *Commissariat à l'Energie Atomique-2189.*

APPENDIX I

Energetic Particle Spectrometer Calibration Data Manipulation Program

This program was written to be used on a Hewlett-Packard 9830A calculator with the HP 9866A printer, the 9862A plotter, and the matrix algebra ROM. Data obtained during calibration can be entered via the program and stored on tape. Once stored the data can be printed, plotted or edited. The program provides several options:

(1) Graph Parameters: the parameters used to plot the graph scales can be modified depending upon the desired plot.

(2) Printer Prompts: for the inexperienced user instructions and special messages are printed on the printer along with the short messages given on the display. Once one becomes familiar with the program the printer prompts can be disabled. The default is to provide printer plots.

(3) Multiple Local Files: the user has the option of working with one or five local data files. A local data file refers to the data stored in the calculator; this is the data that can be printed, plotted, etc. By using multiple local files the user does not have to read from tape as often as when a single local file is used, particularly when superimposing plots, the default is one local file.

(4) Curve Smoothing: the curve smoothing option is not included in this version of the program.

The plotting of graph scales and lables, graph legend, and the actual plot of a local file are separated into separate options in order to allow super-imposed graphs. The "plot energy scale" option produces a horizontal scale at the top of the graph in terms of keV. The user must supply the reference energy, the reference energy PHA channel number, and the number of PHA channels per 10 keV. These parameters can be obtained from a calibrated source and a test generator.

In addition to allowing the reading and writing of data on tapes, the program will format the tapes so that they can be used with this program. It is possible to print the data tape data record headers. If multiple files are in use this option also allows the printing of the headers of the local

data files. If an error occurs it is possible to resume program execution at the "choose an option" point by typing CONT120 and pressing the EXECUTE key.

A suggested format for headers is given after the program listing.

```
10 DIM AI[256],TI[256,5]
11 MAT A=ZER
12 X1=0
13 X2=255
14 Y1=0
15 Y2=400
16 O1=O2=O3=0
17 F1=1
18 MAT T=ZER
20 REM X1=XMIN,X2=XMAX,Y1=YMIN,Y2=YMAX
21 REM T1=X TICK INTERVAL, V1=X VALUE INTERVAL
22 REM T2=Y TICK INTERVAL, V2=V VALUE INTERVAL
23 REM O1=OPTION 1 FLAG: 0=ALL PRINTER PROMPTS, 1=NONE
24 REM O2=MULTIPLE LOCAL FILE FLAG: 1=AVAILABLE, 0=NOT AVAIL.
25 REM O3=CURVE SMOOTHING FLAG: 1=SMOOTH, 0=NORMAL
26 REM F1=LOCAL FILE IN USE: 1=DEFAULT, 1-5 USER ADDRESSABLE
27 REM THIS PROGRAM MAKES USE OF THE MATRIX OPERATIONS ROM AND THE PLOTTER
28 REM CONTROL ROM.
29 REM MATRIX A IS FOR SCRATCH OPERATIONS, MATRIX T CONTAINS LOCAL FILES
47 WRITE (15,48)
48 FORMAT /,/,"ENERGETIC PARTICLE SPECTROMETER CALIBRATION"
49 PRINT "DATA MANIPULATION PROGRAM"
50 IF O1=1 THEN 120
51 PRINT
52 PRINT "SELECT OPTION:"
53 PRINT " "
55 PRINT " 1) PLOT LOCAL FILE"
60 PRINT " 2) PLOT GRAPH SCALES/LABELS"
65 PRINT " 3) PLOT GRAPH LEGEND"
70 PRINT " 4) PLOT ENERGY SCALE"
75 PRINT " 5) CHANGE DEFAULT PARAMETERS"
80 PRINT " 6) PRINT LOCAL FILE "
85 PRINT " 7) ENTER/EDIT LOCAL FILE"
90 PRINT " 8) READ TAPE DATA RECORD INTO LOCAL FILE"
95 PRINT " 9) PRINT TAPE DATA RECORD HEADERS"
100 PRINT "10) WRITE LOCAL FILE ONTO TAPE DATA RECORD"
105 PRINT "11) FORMAT/ERASE DATA TAPE"
110 PRINT " "
120 DISP "CHOSE THE DESIRED OPTION";
130 INPUT I
140 GOTO I OF 2000,1000,1200,3100,2300,800,500,400,4000,700,5000
150 DISP "TYPE CHOICE 1 THROUGH 11";
160 GOTO 130
170 REM*****************************************************************
400 DISP "READ RECORD FROM TAPE"
410 WAIT 2000
420 DISP "WHAT TAPE RECORD NUMBER";
430 INPUT I
431 IF I<0 THEN 471
432 IF O2=0 THEN 439
433 GOSUB 9200
439 LOAD  DATA I,A
440 GOSUB 9000
450 DISP "ROCKET:"T[254,F1]"DETECTOR:"T[255,F1]*1000+T[256,F1]
460 WAIT 4000
461 GOTO 120
471 DISP "INVALID RECORD #="I
472 WAIT 2000
473 GOTO 420
480 REM*****************************************************************
500 DISP "ENTER/EDIT DATA FROM KEYBOARD"
501 WAIT 1000
502 IF O2=0 THEN 511
503 GOSUB 9200
511 IF O1=1 THEN 517
512 PRINT "EDIT DATA FROM KEYBOARD, SELECT OPTION:"
513 PRINT "1. EDIT DATA        ROCKET:";F[254,F1]
514 PRINT "2. EDIT HEADER      DETECTOR:";F[255,F1]*1000+F[256,F1]
515 PRINT "3. ZERO DATA FILE"
```

```
516 PRINT " "
517 DISP "EDIT: 1=DATA 2=HEADER 3= 0 FILE";
518 INPUT I
519 GOTO I OF 555,660,680
520 DISP "INVALID CHOICE:"I
521 WAIT 1000
522 GOTO 517
555 DISP "FIRST ELEMENT TO ENTER";
560 INPUT B
561 IF B<1 THEN 651
562 IF B>253 THEN 651
570 DISP "LAST ELEMENT TO ENTER,0=SINGLE";
580 INPUT E
581 IF E<B AND E#0 THEN 654
582 IF E>253 THEN 654
590 IF E#0 THEN 610
600 E=B
610 FOR I=B TO E
620 DISP "ELEMENT:"I"OLD:"T[I,F1]"NEW:";
630 INPUT T[I,F1]
640 NEXT I
650 GOTO 50
651 DISP "INVALID ELEMENT NUMBER="B
652 WAIT 2000
653 GOTO 555
654 DISP "INVALID ELEMENT NUMBER="E
655 WAIT 2000
656 GOTO 570
659 REM**************************
660 DISP "OLD ROCKET #:"T[254,F1]"NEW #:";
661 INPUT T[254,F1]
662 DISP "OLD DETECTOR#:"T[255,F1]*1000+T[256,F1]"NEW #:";
663 INPUT I
664 T[255,F1]=INT(I/1000)
665 T[256,F1]=I-T[255,F1]*1000
666 GOTO 50
669 REM**************************
680 GOSUB 9100
681 GOTO 50
685 REM*****************************************************************************
700 DISP "WRITE DATA TO TAPE RECORD"
710 WAIT 2000
720 DISP "TAPE RECORD TO WRITE TO";
721 INPUT I
722 IF I<0 THEN 751
725 IF O2=0 THEN 727
726 GOSUB 9200
727 GOSUB 9300
735 DISP "ROCKET:"A[254]"DETECTOR:"A[255]*1000+A[256]
736 WAIT 2000
740 STORE  DATA I,A
750 GOTO 120
751 DISP "INVALID RECORD NUMBER="I
752 WAIT 2000
753 GOTO 720
790 REM*****************************************************************************
800 DISP "PRINT DATA IN LOCAL FILE"
810 WAIT 1000
811 IF O2=0 THEN 820
812 GOSUB 9200
820 WRITE (15,830)T[254,F1],T[255,F1]*1000+T[256,F1]
830 FORMAT /,/,"ROCKET:",F6.0,5X,"DETECTOR:",F7.0,/
840 FOR I=1 TO 51
850 B=I+51
860 C=B+51
870 D=C+51
880 E=D+51
890 WRITE (15,900)I,T[I,F1],B,T[B,F1],C,T[C,F1],D,T[D,F1],E,T[E,F1]
900 FORMAT F3.0,F6.0,F9.0,F6.0,F9.0,F6.0,F9.0,F6.0,F9.0,F6.0
```

```
910 NEXT I
920 WRITE (15,930)
930 FORMAT /,/,/
935 GOTO 50
940 REM*****************************<*******************************
1000 DISP "SCALE/LABEL WITH VALUES"
1005 WAIT 2000
1006 GOSUB 9400
1010 SCALE X1-0.1*(X2-X1),X2+0.1*(X2-X1),Y1-0.1*(Y2-Y1),Y2+0.2*(Y2-Y1)
1020 XAXIS Y1,T1,X1,X2
1030 YAXIS X1,T2,Y1,Y2
1035 LABEL (*,1.2,1.7,0,8/10)
1040 FOR Y=Y1 TO Y2 STEP V2
1050 PLOT X1,Y,1
1060 CPLOT -6,-0.3
1070 LABEL (1080)Y
1080 FORMAT F4.0
1090 NEXT Y
1092 PLOT X1-(X2-X1)*0.1,Y1+(Y2-Y1)*0.3,1
1093 LABEL (*,1.4,1.7,PI/2,8/10)"NUMBER OF COUNTS"
1100 LABEL (*,1.2,1.7,+PI/2,8/10)
1110 FOR X=X1 TO X2 STEP V1
1120 PLOT X,Y1,1
1130 CPLOT -6,-0.3
1140 LABEL (1150)X
1150 FORMAT F4.0
1160 NEXT X
1161 PLOT X1+(X2-X1)*0.3,Y1-(Y2-Y1)*0.1,1
1163 LABEL (*,1.4,1.7,0,8/10)"PULSE HEIGHT ANALYZER CHANNEL"
1170 GOTO 120
1180 REM****************************<*******************************
1200 DISP "PLOT GRAPH LEGEND"
1210 WAIT 2000
1220 DISP "WHICH LINE NUMBER,1-5";
1230 INPUT I
1240 IF I<1 OR I>5 THEN 1220
1250 PLOT X1,Y2+0.2*(Y2-Y1),1
1260 LABEL (*,1.4,1.7,0,8/10)
1270 CPLOT 0,-I
1280 DISP "TO EXIT LEGEND MODE PRESS STOP"
1290 WAIT 1000
1300 LETTER
1310 GOTO 120
1998 REM**********************************************************
1999 REM PLOTTING ROUTINE
2000 IF 2=0 THEN 2005
2001 GOSUB 9200
2005 DISP "PLOT ROCKET:"T[254,F1]"DET:"T[255,F1]*1000+T[256,F1]
2010 WAIT 2000
2020 PEN
2030 PLOT 1,T[X1+(X1=0),F1],-2
2040 FOR X=X1+(X1=0) TO X2-(X2 >= 244)*(X2-244)
2050 PLOT X,T[X,F1]
2060 NEXT X
2070 PEN
2080 GOTO 120
2090 REM****************************#*****************************
2300 DISP "CHANGE PARAMETERS"
2305 WAIT 2000
2310 IF O1=1 THEN 2370
2320 PRINT "SELECT OPTION:"
2330 PRINT "1: GRAPH PARAMETERS"
2335 PRINT "2: PRINT PROMPT MESSAGES (ON/OFF)"
2340 PRINT "3: MULTIPLE FILE OPTION (ON/OFF)"
2355 PRINT "4: CURVE SMOOTHING"
2360 PRINT " "
2370 DISP "1:G PAR 2: PROMPT 3:MULT F 4:SM";
2380 INPUT I
2390 GOTO I OF 2500,2850,2900
```

```
2400 DISP "INVALID SELECTION!"I
2410 WAIT 2000
2420 GOTO 2370
2499 REM************************
2500 DISP "CHANGE PLOTTING PARAMETERS"
2510 WAIT 2000
2520 DISP "OLD XMIN="X1"NEW=";
2530 INPUT I
2540 IF (I<0) OR (I>250) THEN 2690
2550 X1=I
2560 DISP "OLD XMAX="X2"NEW=";
2570 INPUT I
2580 IF (I<X1+50) OR (I>255) THEN 2710
2590 X2=I
2600 DISP "OLD YMIN="Y1"NEW=";
2610 INPUT I
2620 IF (I<0) OR (I>800) THEN 2730
2630 Y1=I
2640 DISP "OLD YMAX="Y2"NEW=";
2650 INPUT I
2660 IF (I<Y1+200) OR (I>1200) THEN 2750
2670 Y2=I
2680 GOTO 50
2690 GOSUB 2800
2700 GOTO 2520
2710 GOSUB 2800
2720 GOTO 2560
2740 GOTO 2600
2750 GOSUB 2800
2760 GOTO 2640
2800 DISP "INVALID PARAMETER:"I
2810 WAIT 2000
2820 RETURN
2830 REM************************
2850 DISP "PRINT PROMPTS,0=YES,1=NO";
2855 INPUT I
2860 IF I<0 OR I>1 THEN 2850
2865 O1=I
2870 GOTO 50
2900 DISP "MULTIPLE FILES, 0=NO, 1=YES";
2910 INPUT I
2920 IF I<0 OR I>1 THEN 2900
2930 O2=I
2940 GOTO 50
2999 REM************************
3000 DISP "CURVE SMOOTHING! 0=NO, 1=YES";
3005 WAIT 2000
3010 INPUT I
3020 IF I<0 OR I>1 THEN 3000
3030 O3=I
3041 DISP "SMOOTHING NOT AVAILABLE"
3042 WAIT 1000
3050 GOTO 50
3099 REM***********************************************************************
3100 DISP "PLOT ENERGY SCALE"
3110 WAIT 2000
3120 DISP "REFERENCE ENERGY,IN KEV";
3130 INPUT E1
3140 IF E1<10 OR E1>300 THEN 3120
3150 DISP "REFERENCE CHANNEL #";
3160 INPUT C1
3170 IF C1<1 OR C1>253 THEN 3150
3180 DISP "# CHANNELS PER 10 KEV";
3190 INPUT C2
3200 IF C2<5 OR C2>100 THEN 3180
3210 REM FIND FIRST ENERGY NUMBER TO PLOT
3220 FOR N=-10 TO 30
3230 IF C1-N*C2 <= X1 THEN 3260
3240 NEXT N
```

```
3250 N=1/0
3260 N=-(N-1)
3270 REM PLOT AXIS THEN TICKS AND LABEL FOR EVERY 10 KEV
3280 PLOT X1,Y2,1
3290 PLOT X2,Y2,+2
3300 PEN
3310 LABEL (*,1.2,1.7,PI/2,8/10)
3320 FOR X=C1+N*C2 TO X2 STEP C2
3325 PLOT X,Y2,1
3330 CPLOT -0.3,-0.3
3340 LABEL (3350)E1+N*10
3350 FORMAT "-",F4.0
3360 N=N+1
3370 NEXT X
3380 REM LABEL AXIS
3390 PLOT X1+(X2-X1)*0.15,Y2,1
3400 LABEL (*,1.2,1.7,0,8/10)
3410 CPLOT 0,3
3420 LABEL (*)"ENERGY LEVEL IN KEV"
3430 GOTO 120
3599 REM*******************************************************************
3600 REM PRINT LOCAL FILE HEADERS
3610 WRITE (15,3620)
3620 FORMAT /,/,"LOCAL FILE HEADERS:",/
3630 FOR I=1 TO 5
3640 WRITE (15,3650)I,T[254,I],T[255,I]*1000+T[256,I]
3650 FORMAT "FILE:",F5.0,8X,"ROCKET:",F7.0,8X,"DETECTOR:",F7.0
3660 NEXT I
3670 WRITE (15,3680)
3680 FORMAT /,/,/
3690 GOTO 50
3999 REM*******************************************************************
4000 DISP "PRINT TAPE LISTING"
4005 WAIT 2000
4006 IF O2#1 THEN 4010
4007 DISP "1=LOCAL FILE HEADERS,0=TAPE";
4008 INPUT I
4009 IF I=1 THEN 3600
4010 DISP "BEGIN WITH RECORD NUMBER";
4020 INPUT B
4030 IF B<0 THEN 4200
4040 DISP "END WITH RECORD NUMBER";
4050 INPUT E
4070 IF E<B THEN 4230
4080 WRITE (15,4090)
4090 FORMAT /,/,/,"DATA TAPE RECORD HEADERS",/
4100 REWIND
4110 FOR I=B TO E
4120 LOAD DATA I,A
4130 WRITE (15,4140)I,A[254],A[255]*1000+A[256]
4140 FORMAT "RECORD:",F5.0,8X,"ROCKET:",F7.0,8X,"DETECTOR:",F7.0
4150 NEXT I
4160 WRITE (15,4170)
4170 FORMAT /,/,/
4180 REWIND
4190 GOTO 50
4200 DISP "INVALID RECORD NUMBER:"B
4210 WAIT 2000
4220 GOTO 4010
4230 DISP "INVALID RECORD NUMBER:"E
4240 WAIT 2000
4250 GOTO 4040
4260 REM*******************************************************************
5000 DISP "FORMAT AND ERASE DATA TAPE"
5010 WAIT 2000
5011 IF O1=1 THEN 5020
5012 PRINT "USE THIS OPTION TO FORMAT NEW TAPES FOR STORING DATA"
5013 PRINT "OR TO EXTEND OLD DATA TAPES.  THIS OPTION WILL"
5014 PRINT "ERASE DATA CURRENTLY ON THE TAPE, ON AND AFTER"
```

```
5015 PRINT "THE FIRST RECORD YOU FORMAT."
5016 PRINT " "
5020 DISP "BEGIN FORMAT/ERASE WITH RECORD"!
5030 INPUT B
5040 IF B<0 THEN 5200
5050 DISP "END FORMAT/ERASE WITH RECORD"!
5060 INPUT E
5070 IF E<B THEN 5230
5080 DISP "REC."B"TO"E"TO BE ERASED"
5090 WAIT 4000
5100 DISP "ENTER 1 TO ERASE/FORMAT RECORDS";
5110 INPUT I
5120 IF I#1 THEN 50
5130 FIND B
5140 MARK (E-B+1),260
5150 MAT A=ZER
5160 FOR I=B TO E
5170 STORE  DATA I,A
5180 NEXT I
5190 GOTO 50
5200 DISP "INVALID RECORD NUMBER:"B
5210 WAIT 2000
5220 GOTO 5020
5230 DISP "INVALID RECORD NUMBER:"E
5240 GOTO 5050
8999 REM************************************************************
9000 REM TRANSFER FROM A TO T(X,I)
9010 FOR Z=1 TO 256
9020 T[Z,F1]=A[Z]
9030 NEXT Z
9040 RETURN
9099 REM************************************************************
9100 REM ZERO ARRAY T(X,F1)
9110 FOR Z=1 TO 256
9120 T[Z,F1]=0
9130 NEXT Z
9140 RETURN
9150 REM************************************************************
9200 DISP "WHICH LOCAL FILE";
9210 INPUT J
9220 IF J >= 1 AND J <= 5 THEN 9255
9230 DISP "INVALID FILE NUMBER"!J
9240 WAIT 2000
9250 GOTO 9200
9255 F1=J
9260 RETURN
9270 REM************************************************************
9300 REM TRANSFER FROM T(X,F1) TO A
9310 FOR Z=1 TO 256
9320 A[Z]=T[Z,F1]
9330 NEXT Z
9340 RETURN
9350 REM************************************************************
9400 REM CALCULATE SCALES AND TICK INTERVALS
9405 T1=10
9406 V1=20
9410 GOTO INT((X2-X1)/55)+1 OF 9420,9440,9440,9460,9460
9420 T1=T1-4
9430 V1=V1-5
9440 T1=T1-10
9450 V1=V1-5
9460 T2=50
9470 V2=100
9480 GOTO INT((Y2-Y1)/205)+1 OF 9490,9510,9510,9530,9530,9530
9490 T2=T2-5
9500 V2=V2-30
9510 T2=T2-40
9520 V2=V2-50
9530 RETURN
9540 REM************************************************************
```

INFORMATION ON DATA MANIPULATION PROGRAM

EACH DATA RECORD CONTAINS THE DATA OBTAIND FROM PULSE
HEIGHT ANALYZER OF A BEAM OF ENERGETIC PARTICLES.
THE PULSE HEIGHT ANALYZER HAS 256 CHANNELS NUMBERED 0
THROUGH 255.   THE DATA MANIPULATION PROGRAM STORES THE VALUES OBTAINED
FOR CHANNELS 1 THROUGH 253.   ALSO STORED WITH THE CALIBRATION DATA
IS A RECORD HEADER CONSISTING OF THE ROCKET PAYLOAD NUMBER, STORED
AS AN INTEGER (E.G. 14542) AND A SIX DIGIT DETECTOR NUMBER.   THE
FIRST DIGIT OF THE DETECTOR NUMBER CORRESPONDS TO THE CHANNEL NUMBER
OF THE DETECTOR (E:G. FOR 14.542 THERE WERE 4 CHANNELS, 1 THROUGH
4).   THE SECOND DIGIT INDICATES WHETHER THE DETECTOR IS USED ON THE
UP LEG OR THE DOWN LEG OF ROCKET.   FOR EXAMPLE, ON 14.542 THE NUMBERS
WOULD BE 11X, 12X, 21X, 31X, 32X, AND 40X= 1UP, 1DOWN, 2UP, 2UP,
3 DOWN, AND 4 UP AND DOWN.   THE CODE IS:

          0 DETECTOR USED ON THE UP AND DOWN LEG
          1 DETECTOR USED ON THE UP LEG
          2 DETECTOR USED ON THE DOWN LEG

THE THIRD DIGIT INDICATES THE PARTICLE TYPE:
          0 RADIOACTIVE SOURCE
          1 ELECTRONS
          2 PROTONS (HIGH SCALE)
          3 PROTONS (LOW SCALE)
          4 TEST GENERATOR
          5 OXYGEN

THE FINAL THREE DIGITS INDICATE THE PARTICLE ENERGY IN KEV.   FOR
EXAMPLE: 120060= DETECTOR 1 DOWN, RADIOACTIVE SOURCE, 60KEV; WHICH
IMPLIES A CO57 SOURCE.   THIS METHOD OF RECORD IDENTIFICATION CAN
BE ADAPTED TO A GIVEN COLLECTION OF DATA RECORDS.

APPENDIX II

General Plotting Program with Tape Facilities

This program was written to be used on a Hewlett-Packard 9830A calculator with the HP 9866A printer, the 9862A plotter, and the matrix algebra ROM. The program will plot up to 200 pairs of points (X and Y coordinates) in the order that the points are stored (the points are connected). The primary use of this program is to plot data that is obtained from hand calculations or from another computer program; if a functional representation of the data is available the plotting routine supplied by Hewlett-Packard should be used.

When formatting a tape for storing data the records must be at least 800 words long. A record of what data is on a data tape should be kept by the user by using the TLIST command; data headers are not used for this program.

```
10 PRINT "THIS PROGRAM IS INTENDED TO PLOT A GRAPH"
20 PRINT "GIVEN A SET OF DATA POINTS IN AN X,Y FORMAT"
30 PRINT "THE USER ENTERS THE NUMBER OF PAIRS OF POINTS,"
40 PRINT "200 MAX, IN ASSENDING ORDER OF X, NOT"
50 PRINT "NECESSARLY EVENLY SPACED.  ALSO REQUIRED ARE"
60 PRINT "THE BOUNDS OF THE X AND Y AXIS."
70 PRINT " "
80 PRINT " "
90 DIM X[200],Y[200]
91 MAT X=ZER[200]
92 MAT Y=X
93 N=200
94 GOTO 300
100 DISP "NUMBER OF POINTS TO BE PLOTTED";
110 INPUT N
120 GOTO 390
140 PRINT "ENTER POINTS IN ACCENDING ORDER OF X IN"
150 PRINT "PAIRS X,Y."
155 PRINT
160 DISP "POINT 1";
170 INPUT X[1],Y[1]
180 FOR I=2 TO N
190 DISP "POINT ";I;
200 INPUT X[I],Y[I]
210 IF X[I] >= X[I-1] THEN 230
220 PRINT "POINT ";I;" IS LESS THAN PREVIOUS POINT, EDIT LATER"
230 REM
240 NEXT I
250 REM
300 PRINT
310 PRINT "SELECT OPTION:"
320 PRINT "1) EDIT DATA"
330 PRINT "2) PRINT DATA"
340 PRINT "3) PLOT DATA"
350 PRINT "4) PLOT AXIS"
360 PRINT "5) DRAW LEGEND"
370 PRINT "6) SET X,Y BOUNDS"
380 PRINT "7) ENTER NEW DATA"
381 PRINT "8) SET N"
382 PRINT "9) READ DATA FROM TAPE"
383 PRINT "10) WRITE DATA TO TAPE"
385 PRINT
390 DISP "TYPE CHOICE, 1-10";
400 INPUT I
410 GOTO I OF 500,700,900,1100,1300,1600,140,100,2100,2300,390
420 GOTO 390
500 REM
510 REM  EDIT DATA
520 DISP "WHICH POINT? (0 TO EXIT)";
530 INPUT I
540 IF I=0 THEN 390
550 IF I<1 OR I>N THEN 590
560 DISP "X=";X[I];" Y=";Y[I];"NEW";
570 INPUT X[I],Y[I]
580 GOTO 520
590 DISP "RANGE ERROR"
600 WAIT 2000
610 GOTO 520
700 REM
710 REM PRINT DATA
711 PRINT
712 PRINT
720 PRINT "POINT","X","Y"
730 PRINT
740 FOR I=1 TO N
750 PRINT I,X[I],Y[I]
760 NEXT I
```

```
770 PRINT
780 PRINT
790 DISP "IF DESIRED, TEAR OFF PAPER"
800 WAIT 4000
810 GOTO 300
900 REM
910 REM PLOT DATA
920 PEN
921 I=1
930 PLOT X[I],Y[I],-2
940 FOR I=2 TO N
950 PLOT X[I],Y[I]
960 NEXT I
965 PEN
970 GOTO 390
1100 REM
1110 REM PLOT AXIS
1120 SCALE X1-0.2*(X2-X1),X2+0.1*(X2-X1),Y1-0.2*(Y2-Y1),Y2+0.2*(Y2-Y1)
1130 XAXIS Y1,T1,X1,X2
1140 YAXIS X1,T2,Y1,Y2
1150 LABEL (*,1.2,1.7,0,8/10)
1160 FOR Y=Y1 TO Y2 STEP V2
1170 PLOT X1,Y,1
1180 CPLOT -6,-0.3
1190 LABEL (*)Y
1200 REM FORMAT F6.0
1210 NEXT Y
1215 LABEL (*,1.2,1.7,PI/2,8/10)
1220 FOR X=X1 TO X2 STEP V1
1230 PLOT X,Y1,1
1240 CPLOT -6,-0.3
1250 LABEL (*)X
1260 REM FORMAT F6.0
1270 NEXT X
1275 PEN
1280 GOTO 390
1300 REM
1310 REM PLOT GRAPH LEGEND
1320 PEN
1330 PLOT X1,Y2+0.2*(Y2-Y1),1
1340 LABEL (*,1.4,1.7,0,8/10)
1350 DISP "ROTATE 90 DEG? (1=YES,0=NO)";
1360 INPUT I
1370 IF I#1 THEN 1400
1380 LABEL (*,1.4,1.7,PI/2,8/10)
1390 PLOT X1,Y1-0.2*(Y2-Y1),1
1400 CPLOT 0,-1
1410 DISP "TO EXIT PRESS STOP";
1420 LETTER
1425 PEN
1430 GOTO 390
1600 REM
1610 REM BOUNDS FOR GRAPH
1620 DISP "INPUT XMIN,XMAX";
1630 INPUT X1,X2
1640 DISP "INPUT: YMIN,YMAX";
1650 INPUT Y1,Y2
1660 DISP "INPUT TICK INTERVAL: X,Y";
1670 INPUT T1,T2
1680 DISP "INPUT LABEL INTERVAL: X,Y";
1690 INPUT V1,V2
1700 GOTO 390
1950 DISP "WHICH TAPE RECORD";
1960 INPUT J1
1970 IF J1<0 OR J1>100 THEN 1950
1980 RETURN
2000 DISP "X OR Y? (X=0,Y=1)";
```

```
2010 INPUT J2
2020 IF J2<0 OR J2>1 THEN 2000
2030 RETURN
2100 DISP "READ DATA FROM TAPE"
2110 WAIT 2000
2120 GOSUB 2000
2130 GOSUB 1950
2140 IF J2=1 THEN 2170
2150 LOAD  DATA J1,X
2160 GOTO 2180
2170 LOAD  DATA J1,Y
2180 GOTO 390
2300 DISP "WRITE DATA TO TAPE"
2310 WAIT 2000
2320 GOSUB 2000
2330 GOSUB 1950
2340 IF J2=1 THEN 2370
2350 STORE  DATA J1,X
2360 GOTO 2380
2370 STORE  DATA J1,Y
2380 GOTO 390
```